Solving the core-cusp problem of cold dark matter halos and the origin of their observational universalities

Go OGIYA

February 2014

Solving the core-cusp problem of cold dark matter halos and the origin of their observational universalities

Go OGIYA
Doctoral Program in Physics

Submitted to the Graduate School of
Pure and Applied Sciences
in Partial Fulfillment of the Requirements
for the Degree of Doctor of Philosophy in
Physics

at the
University of Tsukuba

Graduate School of Pure and Applied Sciences

Solving the core-cusp problem of cold dark matter halos and the origin of their observational universalities

（ コールドダークマターハローのコア–カスプ問題の解決とその観測的経験則の起源）

Go OGIYA

Doctoral Program in	Physics
Student ID	201130065
Doctor of Philosophy in	Physics
Advised by	Masao Mori

Abstract

The present standard paradigm for the structure formation in the universe is called the cold dark matter (CDM) model. It is widely accepted since the predictions are excellently match to the observational results on large scales. However, on scales smaller than about 1Mpc, some serious discrepancies between CDM predictions and observations have been discussed for two decades and are so called the small scale crises. According to the CDM cosmology, small and less–massive systems gravitationally collapse and form early. Larger and more massive systems are formed through mergers among smaller ones. Therefore, it is important to study the properties of dark matter (DM) halos surrounding small galaxies to understand the formation processes of galaxies and DM halos.

The main research target of this thesis is one of the small scale crises, the core–cusp problem. It is well known as a mismatch of the central density distribution between simulated halos and observations. Recent observations of nearby dwarf galaxies and low surface brightness galaxies have revealed that the density profile of the DM halo is almost constant at the center of such galaxies (e.g., Moore 1994; Burkert 1995; de Blok et al. 2001; Swaters et al. 2003; Gentile et al. 2004; Spekkens et al. 2005). In contrast, cosmological N-body simulations based on collisionless CDM have always predicted a steep power–law mass-density distribution at the center of CDM halos (e.g., Navarro et al. 1997; Fukushige & Makino 1997; Moore et al. 1998). This discrepancy is the core–cusp problem of the CDM scenario. I study the dynamical response of DM halos to change in gravitational potential induced by stellar feedback by using numerical simulations and constructing an analytical model. In the process, I also find an interesting relation between the scenario of the cusp–to–core transformation and the observational laws.

In this Ph.D thesis, I present the results of some works conducted by myself and my collaborators.

The Connection between the Cusp–to–Core Transformation and Observational Universalities of Dark Matter Halos

Observations have revealed interesting universal properties of DM halos especially around low-mass galaxies. Strigari et al. (2008) showed that DM halos have common enclosed masses within 300pc (Strigari relation). Kormendy & Freeman (2004) reported DM halos having almost identical central surface densities (the $\mu_{0\mathrm{D}}$ relation). In addition, there exists a core–cusp problem, a discrepancy of the central density distribution between simulated halos and observations. We investigate whether a scenario where cuspy halos

transform into cores by some dynamical processes can also explain their universal structural properties. It is shown that a cusp–to–core transformation model naturally reproduces the μ_{0D} relation and that Strigari relation follows from the μ_{0D} relation for dwarf galaxies. For both, large galaxies and very small galaxies we predict that both relations cannot be fulfilled simultaneously. We also show that the central densities of cored dark halos provide valuable information about their formation redshifts.

A Tree–SPH Code Developed for GPU Clusters

DM halos are categolized into collisionless self–gravitational systems in which the gravity of the whole system is more important than encounters of nearby matter. To follow the dynamical evolution of such systems, N–body simulation utilizing the tree algorithm (Barnes & Hut 1986) is a suitable numerical method. N–body simulations with a large number of particles must be performed to remove the effects of artificial two–body relaxation and to achieve a sufficiently high resolution that ensures the softening length is much smaller than the resolution limit of the observations of the density profiles of DM halos. To perform such large scale simulations within a reasonable time, we accelerate a tree–code using garaphics processing units (GPUs). The implementation tailored to behaviors of GPU cores, bundling the routes of particles in a tree structure, dramatically accelerates computing gravity. We parallelize the code with the Message Passing Interface (MPI) and finally achieve the performance to compute gravity among 10^9 particles within about 18 seconds per time. Applying similar methods, the smoothed particle hydrodynamics (SPH) scheme (Lucy 1977; Gingold & Monaghan 1977; Saitoh & Makino 2013) is accelerated on the GPU cluster.

Dynamical Effects of Gas Mass–Loss on Dark Matter Halos

We perform N-body simulations to study the nonlinear response of CDM halos to the variance of the gravitational potential induced by gas removal from galaxy centers. We focus on the timescale of the gas ejection, which is strongly correlated with stellar activities, and demonstrate that it is one of the key factors in determining the dynamical response of CDM halos. The results of simulations show that the power–law index of the mass–density profile of the DM halo correlated with the timescale of the mass loss, and it is flatter when the mass loss occurs over a short time than when it occurs over a long time. However, it is still larger than typical observational values; in other words, the central cusp remains for any mass loss model in the simulations. Moreover, for the slow mass-loss case, the final density profile of the DM halo recovers the universal density profiles predicted by the CDM cosmology. Therefore, mass loss driven by stellar feedback may not be an effective mechanism to flatten the central cusp.

Dynamical Effects of Gas Oscillation on Dark Matter Halos

In this chapter, we investigate the dynamical response of DM halos to recurrent starbursts in forming less–massive galaxies to solve the core–cusp problem. The gas heated by supernova feedbacks after a starburst expands, and the star formation then terminates. This expanding gas loses energy by radiative cooling, and then falls back toward the galactic center. Subsequently, the starburst is enhanced again. This cycle of expansion and contraction of the interstellar gas leads to a repetitive change in the gravitational potential of the gas. The resonance between DM particles and the density wave excited by the oscillating potential plays a key role in understanding the physical mechanism of the cusp–to–core transformation of DM halos. DM halos effectively gain kinetic energy from the baryon potential through the energy transfer driven by the resonance between the particles and density waves. We determine that the critical condition for the cusp–to–core transformation is such that the oscillation period of the gas potential is approximately the same as the local dynamical time of DM halos. We present the resultant core radius of a DM halo after

the cusp–to–core transformation induced by the resonance, by using the conventional mass–density profile predicted by the CDM models. Moreover, we verify the analytical model by using numerical simulations, and the results validate the resonance model.

Contents

Part I

Mass–Density Profile and Structural Properties of Dark Matter Halos

Chapter 1 Introduction

1.1 Dark Matter

Thanks to huge effort made by astrophysists and astronomers, our understanding of the structure formation in the universe has been dramatically improved. Recent observations of the Cosmic Microwave Background (CMB) radiation, the Wilkinson Microwave Anisotropy Probe (*WMAP*) satellite (Spergel et al. 2007; Komatsu et al. 2009, 2011), have determined the composition of the universe accurately. According to their results, about 22.5 % of the total energy density is accounted by an invisible and unidentified matter, so called "dark matter (DM)". Baryonic matter (atoms) and dark energy (unidentified) account about 4.5 % and 73 %, respectively. This means that about 84 % of matter exists as DM. In addition, DM is assumed as a kind of matter which interacts only gravitationally (therefore it is invisible) and is dissipationless. Because of these features, DM is the main source of the gravitational potential which drives the dynamical evolution and formation of the structures in the universe (galaxies, clusters of galaxies and so on).

The existence of DM was firstly pointed out by Zwicky (1933). Using the virial theorem, he estimated the dynamical mass of the Coma cluster. He proposed DM as a invisible mass to explain the larger velocity dispersion than that of expected from the luminosity. But his idea seemed to be flabbergasting and was not recognized by researchers of the time. Decades later, some studies (e.g., Rubin & Ford 1970; Rubin et al. 1980) measured rotation velocity profiles of spiral galaxies. They found that rotation velocities of galaxies do not decrease at the outskirts in spite of absenses of luminosity (visible mass). They also found the rotation velocities of galaxies become almost constant values at the outskirts, so called the flat rotation curve. Faber & Jackson (1976) extended this feature to elliptical galaxies. Because of these observational facts, the picture in which visible galaxies are embedded in invisible halos of DM (hearafter, DM halo or dark halo) has been standard.

The observations of CMB also revealed the condition of the initial density fluctuation in the universe. The amount of the density fluctuations is order of 10^{-5} at redshift, $z \approx 1000$. Starting from the initial small fluctuations, matters have been attracted gravitationally and have formed bounded systems. In this process, DM plays crucial roles. DM contracts earlier than dissipational baryonic matter due to the dissipationless feature, and helps the contraction of baryon. Considering the model of the universe without DM, observed galaxies have not been constructed even now (Silk 1968). After losing internal energy by radiative cooling, baryon begins to contract and to form stars with help from potential of DM (Rees & Ostriker 1977). Therefore, stars and galaxies have been formed in the potential well of DM halos.

The present standard paradigm for the structure formation in the universe is called the cold dark matter (CDM) cosmology (e.g., White & Rees 1978), where "cold" means the rest mass of a DM particle is much greater than its kinetic energy. This model is widly accepted, since its predictions, for example, the power spectrum of density fluctuations (e.g., Tegmark et al. 2004), the distribution of galaxies judged by the two–point correration function (e.g., Eisenstein et al. 2005), and the spectrum of temperature fluctuations of the CMB (e.g., Hinshaw et al. 2007) excellently match observations. Because gravity is believed to be the most important force to determine the dynamical evolution of systems on large scales, collisonless N–body simulations starting from initial conditions which follow observational results have fulfilled key roles to obtain quantitative predictions (e.g., Navarro et al. 1995, 1996b, 1997; Fukushige & Makino 1997; Moore et al. 1998, 1999b; Jing & Suto 2000; Klypin et al. 2001; Fukushige et al. 2004; Navarro et al. 2004; Diemand

et al. 2004; Reed et al. 2005; Ishiyama et al. 2008; Stadel et al. 2009; Ishiyama et al. 2009; Navarro et al. 2010; Klypin et al. 2011; Ishiyama et al. 2013).

1.2 The Core–Cusp Problem

The CDM cosmology also predicts that smaller and less–massive systems gravitationally collapse and form earlier. Larger and more massive systems have formed through mergers among smaller ones. Generally, small galaxies (e.g., dwarf galaxies) are believed to have less–massive DM halos. Therefore, it is important to study the properties of DM halos surrounding dwarf galaxies to understand the physical processes of formation of galaxies and DM halos. Studying such small systems is also important to constrain the properties of DM particles, because they are dynamically dominated by DM (e.g., Mateo 1998). Although the CDM cosmology has gotten successful on large scales ($\gtrsim$1Mpc), some serious discrepancies between CDM predictions and observations are being discussed on smaller scales ($\lesssim$1Mpc). One of them is the core–cusp problem, that is the mismatch of the observationally inferred central density structures of DM halos when compared with theoretical predictions.

Cosmological N–body simulations based on the CDM cosmology claim divergent density distributions, called cusps, in the centers of DM halos (e.g., Navarro et al. 1996b, 1997; Fukushige & Makino 1997; Moore et al. 1998, 1999b; Ishiyama et al. 2013). The Navarro–Frenk–White (NFW) profile (Navarro et al. 1997) well fits the density structures of simulated CDM halos,

$$\rho(r) = \frac{\rho_{\rm s} r_{\rm s}^3}{r(r+r_{\rm s})^2}, \tag{1.1}$$

where r is the distance from the center and $\rho_{\rm s}$ and $r_{\rm s}$ are the scale density and scale length of the halo, respectively. On the other hand, DM halos of observed galaxies, especially for low–mass galaxies, indicate constant density profiles, called cores or at least shallower cusps, in contrast to the steep cusps, predicted by cosmological simulations (e.g., Moore 1994; Burkert 1995; Salucci & Burkert 2000; de Blok et al. 2001b,a; Swaters et al. 2003; Weldrake et al. 2003; Gentile et al. 2004; Spekkens et al. 2005; Kuzio de Naray et al. 2006, 2008; Oh et al. 2008; van Eymeren et al. 2009; Oh et al. 2011). The Burkert profile (Burkert 1995) reproduces well the density structures of DM halos obtained from observation data (see also Salucci & Burkert 2000),

$$\rho(r) = \frac{\rho_0 r_0^3}{(r+r_0)(r^2+r_0^2)}, \tag{1.2}$$

where ρ_0 and r_0 are mean the central density and the core radius of the halo, respectively.

If DM particles are only interacting gravitationally, flattening out a central DM cusp would require changes in the gravitational potential. Several mechanisms have been proposed and indeed succeed to reduce the central density. One of them is change in the gravitational potential caused by stellar feedback redistributing gas or generating galactic winds (e.g., Navarro et al. 1996a; Read & Gilmore 2005; Mashchenko et al. 2006, 2008; Pontzen & Governato 2012; Teyssier et al. 2013). Another example is the heating by dynamical friction of massive clumps (e.g., El-Zant et al. 2001; Tonini et al. 2006; Goerdt et al. 2010; Cole et al. 2011; Inoue & Saitoh 2011).

1.3 The Observational Universalities of Dark Matter Halos

In connection with this problem, some studies reported observational universalities of DM halos. Strigari et al. (2008) found there exists a common mass scale among DM halos of nearby dwarf galaxies. According to their analysis that is based on Jeans equation for spherical systems, the enclosed DM mass within 300pc from the halo centers, $M(<300\text{pc})$, is $\sim 10^7 M_\odot$ (hereafter, Strigari relation). Motivated by these

observations, Walker et al. (2009) argued that all dwarfs are embedded in the same universal DM halo. Hayashi & Chiba (2012) evaluated $M(< 300\mathrm{pc})$ using non–spherical Jeans analysis. Independent of Strigari relation, Kormendy & Freeman (2004) revealed the quantity, $\mu_{0\mathrm{D}} \equiv \rho_0 r_0$, which corresponds to the central surface density of DM halos for cored profiles, does not depend on blue magnitude of galaxies (hereafter, the $\mu_{0\mathrm{D}}$ relation). Donato et al. (2009) confirmed this result for a larger sample, including nearby dwarf and spiral galaxies. The finding of Kormendy & Freeman (2004) is also consistent with the observed correlations of core parameters $\rho_0 \propto r_0^{-1}$ when fitting the observations by Burkert halos as affirmed by Salucci et al. (2012). They also obtained $\mu_{0\mathrm{D}} \sim 140 M_\odot \mathrm{pc}^{-2}$.

1.4 This Thesis

In this thesis, I firstly argue the relation between a scenario of the cusp–to–core transformation and the observational laws of DM halos, and find that the scenario naturally reproduces the observational laws. This means that it is possible to explain observations of structural properties of DM halos simultaneously in the CDM framework. This is an important result since we can regard it as a support of the standard paradigm, the CDM cosmology. The argument also provide us valuable information about the formation redshifts of DM halos.

Numerical simulation is a powerful tool in astrophysics. Especially, N–body simulations are widely used to study the dynamics of self–gravitational systems including DM halos. In simulations, a large number of particles must be employed to avoid artificial two–body relaxation and to achieve a sufficiently high resolution, but a large amount of calculation is needed. In order to carry out simulations in a reasonable comutation time, we develop a tree code (Barnes & Hut 1986) optimized for Graphic Processing Unit (GPU) clusters. GPUs attract lots of attention as a powerful computing accelerator, and the GPU acceleration is a big research area of high performance computing. Our tree code achieves a performance which enables us to compute gravity among a billion particles within 18 seconds per time. I also extend the code to the Smoothed Particle Hydrodynamics (SPH) method which is a well known Lagrangian scheme to simulate dynamics of fluid numerically (e.g., Monaghan 1992, 2005; Rosswog 2009; Springel 2010; Price 2012; Saitoh & Makino 2013, and references therein).

Using numerical simulations, I study the dynamical response of DM halos to change in gravitational potential driven by supernova feedback which expected to be closely related with the star formation activities in galaxies. Supernova feedback expells gas from the galactic center. This phenomenon makes the gravitational potential around the center of the DM halos shallower, and impacts the mass distribution of DM halos dynamically.

The core–cusp problem is often discussed for low–mass galaxies, such as dwarf galaxies and low–surface–brightness galaxies. Low–mass galaxies are more sensitive to stellar feedback, as compared to giant ones, because of their shallow gravitational potential well. The hydrodynamical response of galaxies to stellar activity depends on various factors such as their mass, morphology, and star formation history (e.g., Dekel & Silk 1986; Yoshii & Arimoto 1987; Mori et al. 1997, 1999, 2002; Mac Low & Ferrara 1999; Silich & Tenorio-Tagle 2001; Bland-Hawthorn et al. 2011). Observations of nearby dwarf galaxies have revealed that such galaxies have particular properties (e.g., Mateo 1998; Tolstoy et al. 2009; McQuinn et al. 2010a,b; Weisz et al. 2011). Therefore, supernova feedback is expected to give various dynamical effects on the mass distribution of DM halos and I test following two models. To remove the effects of artificial two–body

relaxation which causes cusp flattening even though no potential change exists, sufficient number of particles is employed in the simulations.

The first model corresponds to the case in which gas has been blown out from the galaxies as galactic winds. I perform collisionless N–body simulations that focus on the dependence of the dynamical response of DM halos on the timescale of gravitational potential change. Simulation results show that the timescale of mass–loss is one of the important factors in determining the dynamical response of DM halos. We obtain the the surprising result: the gas mass–loss is not an effective mechanism to the cusp.

Recent hydrodynamic simulations clearly demonstrate the existence of the phenomena called galactic fountains (e.g., Stinson et al. 2007). When the energy of gas gained from supernova feedback is insufficient to escape from the galactic potential, the heated gas expands temporarily, and the star formation is then terminated. The expanding gas loses thermal energy by radiative cooling, and then falls back toward the galactic center. After that, the star formation is re–enhanced and subsequently ignites a starburst. This repetitive gas motion leads to a recurring potential change. The second model is based on these phenomena.

In order to understand the fundamental physical mechanism to determine the dynamical response of DM halos to a recurring change in gravitational potential, we construct a simple analytical model. According to our model, the resonance between DM particles and density waves induced by the oscillating gravitational potential plays crucial role to flatten the central cusp. Applying this model, we can predict the resultant core scale created through the resonance. Then, we examine our analytical model using collisionless N–body simulations and find its validity. Furthermore, I perform N–body + SPH simulations to study if the resonance mechanism works in the more realistic cases.

Chapter 2 The Connection between the Cusp–to–Core Transformation and Observational Universalities of DM Halos

2.1 Motivation

The structural universalities of DM halos have been reported by recent observations with high qualities and spatial resolutions. Strigari et al. (2008) revealed the common mass scale of DM halos surrounding nearby dwarf galaxies. They analysed the velocity dispersion profiles of stars by solving Jeans equation, and estimated the mass structures of dark halos. According to their results, sample halos contain about $10^7 M_\odot$ within 300 pc from the centers (Strigari relation). Independent of this study, Kormendy & Freeman (2004) found DM halos have the identical central column density. This result has been affirmed by some studies (e.g., Donato et al. 2009; Salucci et al. 2012).

These properties of DM halos should be closely related with their mass–density structures. A serious descrepancy about the mass–density structure of DM halo, the core–cusp problem would be solved if the central cusp is flattened out. We study if the scenario of the cusp–to–core transformation explains the origin of the structural universalities. If so, this would be a strong confirmation of the CDM cosmology on the small scales.

2.2 Concentration Parameter

The concentration parameter of an NFW halo, c, is defined by $c \equiv r_{200}/r_{\rm s}$, where r_{200} is the radius inside of which the mean density of the DM halo is 200 times of the critical density of the universe and which is called the virial radius. This is related to the virial mass, M_{200}, by

$$M_{200} \equiv \frac{4\pi}{3} 200 \rho_{\rm crit} (1+z)^3 r_{200}^3, \tag{2.1}$$

where $\rho_{\rm crit}$ and z are the critical density of the universe and redshift, respectively. If we know the dependence of c on M_{200} and z, we can determine the parameters of the NFW halo, $\rho_{\rm s}$ and $r_{\rm s}$, for given M_{200} and z. Such dependence, $c(M_{200}, z)$, has been investigated by using cosmological N–body studies (e.g., Bullock et al. 2001; Macciò et al. 2008), most of which concluded that c decreases monotonically with increasing M_{200} and decreasing z. This is a result of the fact that c reflects the cosmic density at the formation (collapse) epoch of DM halos. In the standard CDM cosmology, the cosmic density decreases with time, and present massive objects are believed to have collapsed later than smaller ones.

Recently, Prada et al. (2012, hearafter P12) determined $c(M_{200}, z)$. According to their results, c is described by a nearly universal U–shaped function of M_{200}, and the dependence on z is more complex than proposed by Bullock et al. (2001). Ludlow et al. (2012) pointed out halos around the minimum of the U–shaped function are not relaxed dynamically and are in the early period of merger events. The analysis of P12 and Ludlow et al. (2012) was restricted to $M_{200} > 10^{11} M_\odot$. In order to determine $c(M_{200}, z)$ on less

massive scales, we analysed the data of the cosmological simulation, *Cosmogrid*, performed by Ishiyama et al. (2013, hearafter I13). Though the covered volume is smaller than that of the Millenium simulations (Springel et al. 2005; Boylan-Kolchin et al. 2009), the Bolshoi (Klypin et al. 2011) and the MultiDark simulations (P12), the mass resolution is about 1000 times better (particle mass $\sim 10^5 M_\odot$). Therefore we could analyse c of DM halos down to $M \sim 10^8 M_\odot$ which is comparable to the virial mass of dSphs.

Along the lines of P12, we computed c of each halo from the velocity ratio $V_{\rm max}/V_{200}$. $V_{\rm max}$ and V_{200} are the maximum circular velocity and the circular velocity at r_{200}, respectively. Fig. 2.1 shows the concentration parameter of DM halos as a function of M_{200}. The fitting formula given by P12 perfectly predicts the result of our simulation at the redshift $z = 3$, and reasonably matches that of the redshift $z = 5.4$. The small offset seen in the lower panel arise from the difference of the adopted cosmological parameters, especially σ_8. A similar level of offset is observed at $z = 10.8$ (not shown). However, this is within a small error range and gives negligible effects on the following analysis.

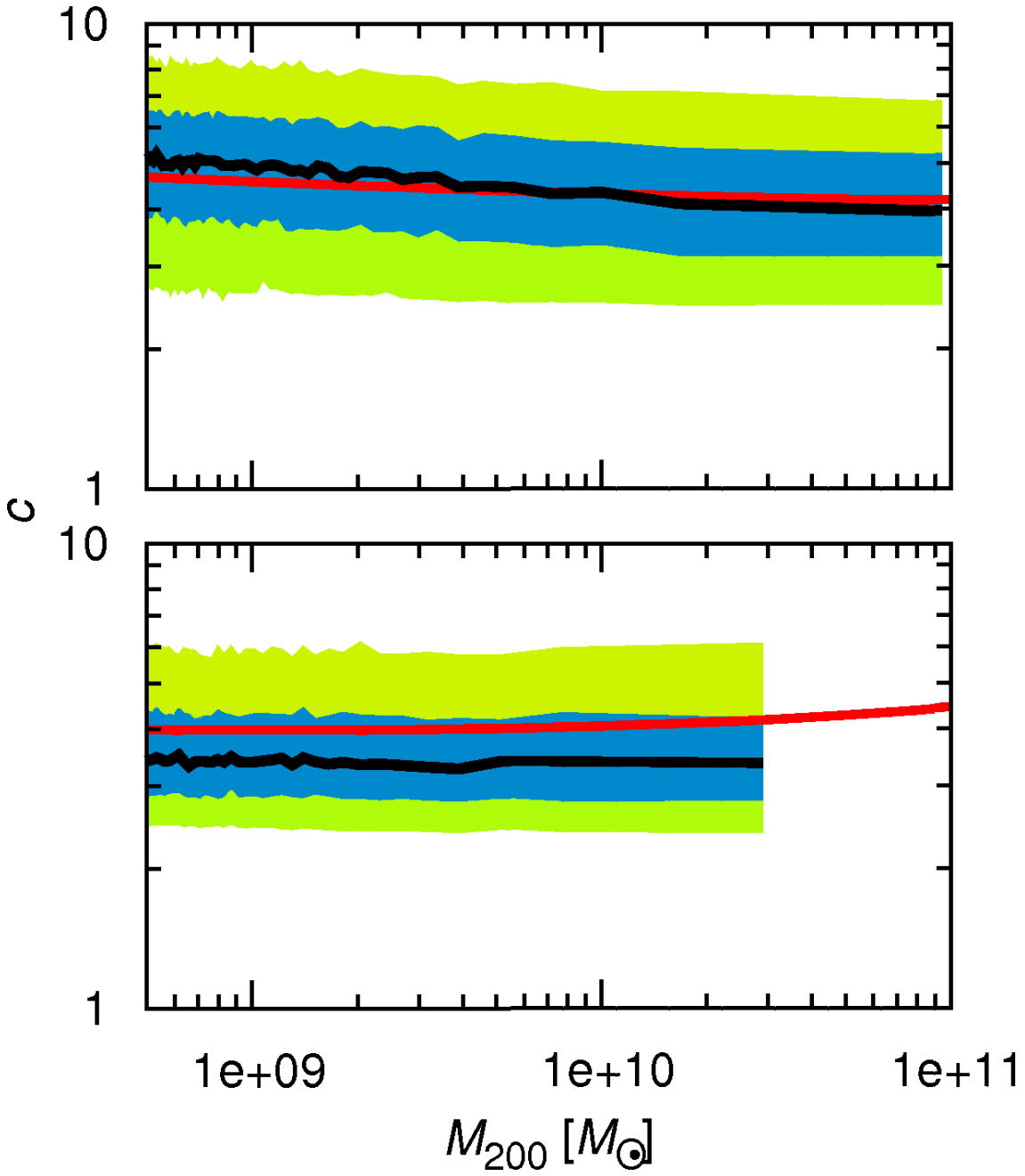

Fig. 2.1: The concentration parameter, c, of DM halos as a function of the virial mass, M_{200}. Red and black lines indicate the fitting formula $c(M_{200}, z)$ proposed by Prada et al. (2012) and the median of our result, respectively. Blue and green areas cover halos distributed within the offsets of 25th and 45th percentiles from the median. Upper and lower panels correspond the results for $z = 3.0$ and $z = 5.4$, respectively.

2.3 The Origin of the μ_{0D} Relation

Using the fitting formula $c(M, z)$, we study the connection between the cusp–to–core transformation and the μ_{0D} relation and estimate some characteristic properties of DM halos. The procedures and assumptions of the analysis are as follows:

(1) Halo formation: We assume that DM halos form following an NFW profile with the $c(M_{200}, z)$ of P12 for given M_{200} and z.

(2) Cusp–to–Core transformation: We then assume that NFW halos are transformed into Burkert halos by the dynamical process quoted in chapter 1.

We then determine the parameters of the Burkert profile into which a given dark halo distribution will transform. For that we impose two conditions. First, we require mass conservation, that is, M_{200} is conserved during the cusp–to–core transformation. Secondly, we assume that the density distribution is affected only in the inner regions while the outer density distribution is preserved. This is a reasonable assumption if this transition is a result of variations in the gravitational potential caused by baryons and stellar feedback. From Equations (1.1) and (1.2), this condition requires

$$\rho_{\rm s} r_{\rm s}^3 = \rho_0 r_0^3. \tag{2.2}$$

We show the results in Fig. 2.2 which plots r_0 vs. ρ_0. Though Spano et al. (2008) assumed an isothermal sphere to derive the core parameters, the difference between a Burkert profile and an isothermal sphere is small if the parameters (i.e., the central density and the core radius) are the same. Therefore we adopt the data from Spano et al. (2008) as parameters of the corresponding Burkert profile. The sample galaxies of Salucci et al. (2012, triangles) are nearby dSphs. The data from Donato et al. (2009, circles) and Spano et al. (2008, squares) covers more massive galaxies. In Fig. 2.2, the yellow and green regions indicate that the free-fall time is longer than the cooling time assuming the collisional equilibrium of the primordial composition of the gas with hydrogen molecules. Such a parameter range, the cooling is efficient so that these objects can cool and condense leading to the active star formation. Most of sample galaxies along the μ_{0D} relation lie in these regions. Therefore, we find that the scenario proposed in this study, the cusp–to–core transformation, naturally explains the μ_{0D} relation.

Figure 2.2 also shows that the central density, ρ_0, is nearly constant for each cusp–to–core transformation redshift, $z_{\rm t}$, at which the central cusp has been transformed into core. We assume that DM halos have survived until now without significant change of the virial mass. Assuming that central cusps have been flattened out into cores by mechanisms which involve star formation activities (e.g., Ogiya & Mori 2011, 2012), $z_{\rm t}$ corresponds to the formation epoch of DM halos and galaxies, approximately. As shown in Fig. 2.1, the dependence of c on M_{200} is weak, especially at high redshifts (see also Fig. 12 in P12). Using this and the definition of the virial mass, Equation (2.1), $r_{\rm s}^3 \propto M_{200}$ should be satisfied. We have defined the scale density, $\rho_{\rm s}$, by the mass profile of NFW profile,

$$\rho_{\rm s} = \frac{M_{200}}{4\pi r_{\rm s}^3 \left[\ln(1+c) - \frac{c}{1+c}\right]}, \tag{2.3}$$

and found $\rho_{\rm s}$ is almost independent of M_{200}. As one of the results of the anasysis, we know that the core radius of Burkert halos, r_0, is close to the scale length of corresponding NFW halos, $r_{\rm s}$. This means that $\rho_0 \approx \rho_{\rm s}$ since ρ_0 is determined by Equation (2.2). Combining everything, one can understand why the dependence of ρ_0 on r_0 is fairly weak. Fig. 2.2 allows us to estimate $z_{\rm t}$ from ρ_0. As expected, the higher

the core density, the higher the transformation redshift of the corresponding halo. Halos with small core radii and correspondingly high core densities have small virial masses while large cores reside in massive dark halos.

Burkert (1995) obtained the density profiles of several DM halos. His sample halos had core radii of $10^3\mathrm{pc} \lesssim r_0 \lesssim 10^4\mathrm{pc}$. Fig. 1 in Burkert (1995) showed their outer density structures correspond to CDM halos formed at $z = 0.6$. He also proposed a scaling relation between r_0 and ρ_0, and Salucci & Burkert (2000) confirmed this relation for a larger sample. Our results match this relation (blue box). Salvadori et al. (2008) constructed a semi–analytical model to fit the observed features of the Sculptor dSph and found its transformation redshift to be about 7. Our core property estimate for this formation redshift matches nicely the observational measurements (large triangle). They also derived the virial mass of the Sculptor dSph which is about $10^8 M_\odot$. Using the observationally inferred r_0 and transformation redshift, z_t, a halo virial mass of $M_{200} \sim 1.2 \times 10^8 M_\odot$ which is a perfect match to their result is derived.

As demonstrated in this section, the cusp–to–core transformation naturally generates the μ_{0D} relation in the context of the CDM cosmology. We also find that the cusp–to–core transformation redshift, z_t, is closely related to the central density of cored DM halos. Interestingly, the parameters of the Burkert profile (r_0 and ρ_0) are almost the same as the scaling parameters of corresponding NFW halos (r_s and ρ_s). Therefore we conclude that the observed universal correlation between the core parameters has been shaped by the physics of formation of these DM halos, in other words, the cores of dark halos retain a memory of their formation redshift. The $c(M_{200}, z)$ relation is essentially important for these results since it determines the parameters of NFW profile.

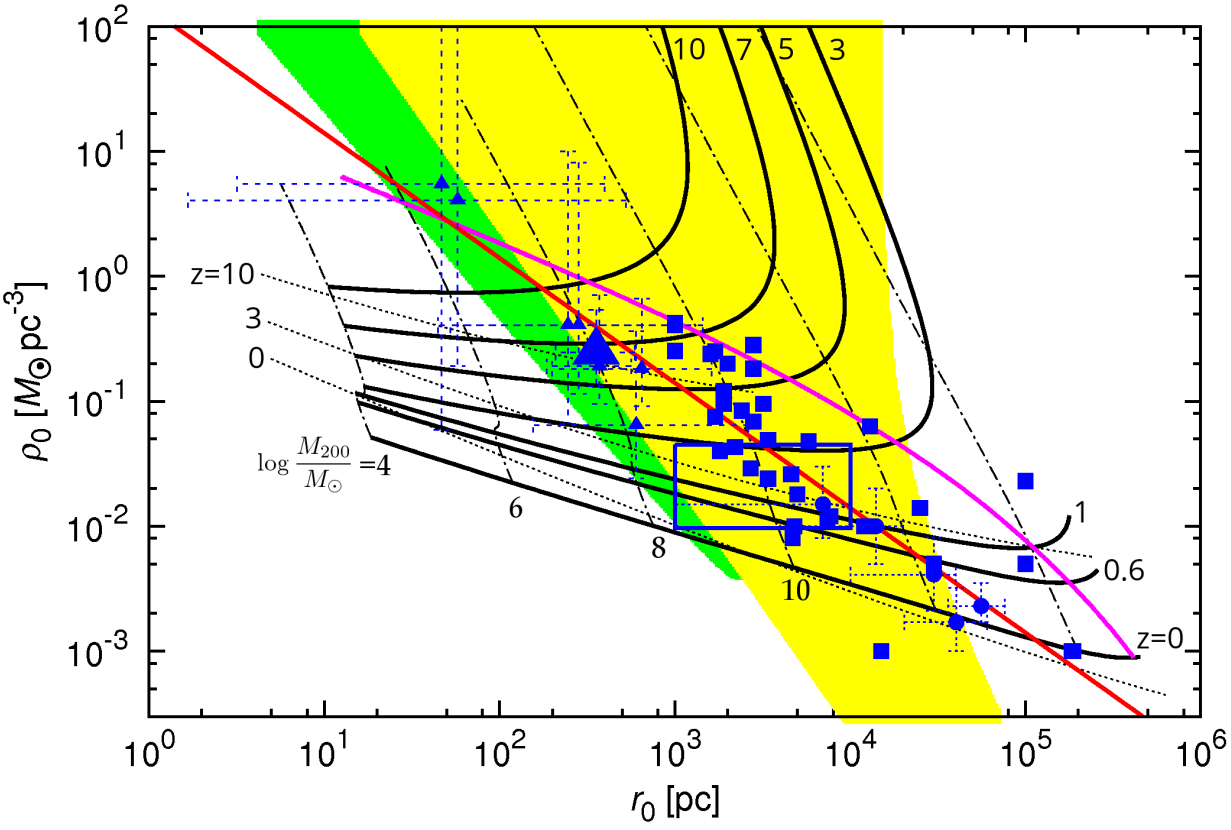

Fig. 2.2: Diagram of r_0 vs. ρ_0. Respective points show the parameters of Burkert profile, ρ_0 and r_0, obtained by observations. Triangles, squares and circles represent the data from Salucci et al. (2012), Spano et al. (2008) and Donato et al. (2009), respectively. Large triangle denotes the Sculptor dSph. Red line is the scaling relation between ρ_0 and r_0 proposed by Salucci et al. (2012). The place embraced by blue box corresponds to the results of Burkert (1995). Solid and dotted black lines show the results of our analysis applying the $c(M, z)$ proposed by Prada et al. (2012) and Macciò et al. (2008), respectively. Subscripts denote the corresponding transformation redshift, z_t. Black dot–dashed lines are the contour of halo mass. Magenta line corresponds to the density peaks, $\delta = \delta_c = 3\sigma(M, z)$, where $\delta_c = 1.69$ and $\sigma(M, z)$ are the critical density peak to collapse and the linear rms fluctuation of the density field for given mass and redshift, $\sigma(M, z)$, respectively. Applying the Press–Schechter theory (Press & Schechter 1974), most of halos satisfy $\delta < 3\sigma(M, z)$ (below magenta line), stochastically. The yellow and green regions indicate the parameter range satisfying the condition, $t_{\rm cool} \leq t_{\rm ff}$, where $t_{\rm cool}$ and $t_{\rm ff}$ are the cooling time and the free–fall time of the gas, respectively. Aassuming a total gas mass equal to $0.1\,M_{200}$, and a molecular abundance equal to 0.1% of the neutral hydrogen, we estimate the cooling time using the cooling function of primordial gas given by Sutherland & Dopita (1993, yellow) including H_2 cooling (temperature below $\sim 10^4$ K, green) given by Galli & Palla (1998).

2.4 Relation between Universalities

The above mentioned $M(< 300\mathrm{pc})$ universality has been reported for DM halos surround nearby dwarf galaxies. These galaxies are also included in the samples which were used to derive the $\mu_{0\mathrm{D}}$ relation. In this section, we show the consistency between both relationships among nearby dwarfs and the inconsistency for larger and smaller galaxies. We start by adopting a Burkert profile for the mass–density structures of DM halos. The mass enclosed within given radius, r, is then

$$M(r) = \pi\rho_0 r_0^3 \Bigg\{ -2\arctan\left(\frac{r}{r_0}\right) + 2\ln\left(1+\frac{r}{r_0}\right) + \ln\left[1+\left(\frac{r}{r_0}\right)^2\right] \Bigg\}. \tag{2.4}$$

(Mori & Burkert 2000). We use Eqs. (2.3) and (2.4) in the analysis of this section.

The upper panel of Fig. 2.3 shows the DM mass enclosed within 300pc, $M(< 300\mathrm{pc})$, as a function of the core radius, r_0. As shown in this panel, the DM halos of dSphs have $\sim 10^7 M_\odot$ within 300pc. This is consistent with Strigari relation (black line) for lower core radii. Independent of this study, Faerman et al. (2013) show Burkert profile naturally produces Strigari relation for nearby dwarf galaxies. However, halos of larger galaxies deviate from it. Our theoretical prediction, shown by the solid red line fits the data very well and indicates that Strigari relation is just a coincidence resulting from the fact that dwarf galaxies like close to the maximum of $M(< 300\mathrm{pc})$ versus r_0 correlation. As a result we would predict that halos that are smaller than those typically found around dSphs should have smaller values of $M(< 300\mathrm{pc})$ as predicted by Strigari relation. We also show $M(< 300\mathrm{pc})$ of NFW halos supposing $\rho_\mathrm{s} r_\mathrm{s} = 140 M_\odot \mathrm{pc}^{-2}$ (red dashed line). For this line, the horizontal axis corresponds to r_s. Comparing the solid and dashed red lines one can see it is difficult to distinguish between NFW halos and Burkert halos for dwarfs, but that measurements of core properties for more massive halos should allow to distinguish between the different halo profiles. The lower panel of Fig. 2.3 shows the central density of the Burkert profile, ρ_0, as a function of r_0. This panel clearly demonstrates the two relations are consistent with each other among dSphs, but inconsistent for larger galaxies with scale radii of order 10 kpc or larger.

The consistency between Strigari and the $\mu_{0\mathrm{D}}$ relation breaks down for larger halos surround massive galaxies, but these galaxies follow the $\mu_{0\mathrm{D}}$ relation very well. From that we conclude that Strigari relation is just an indirect evidence of the $\mu_{0\mathrm{D}}$ one for the case of dwarf galaxies, since the latter covers a broader range of halo masses and halo core radii. In addition, the NFW profile does not follow theses observations well, indicating that the cusp–to–core transformation is an important process for the evolution of the inner dark halo structure.

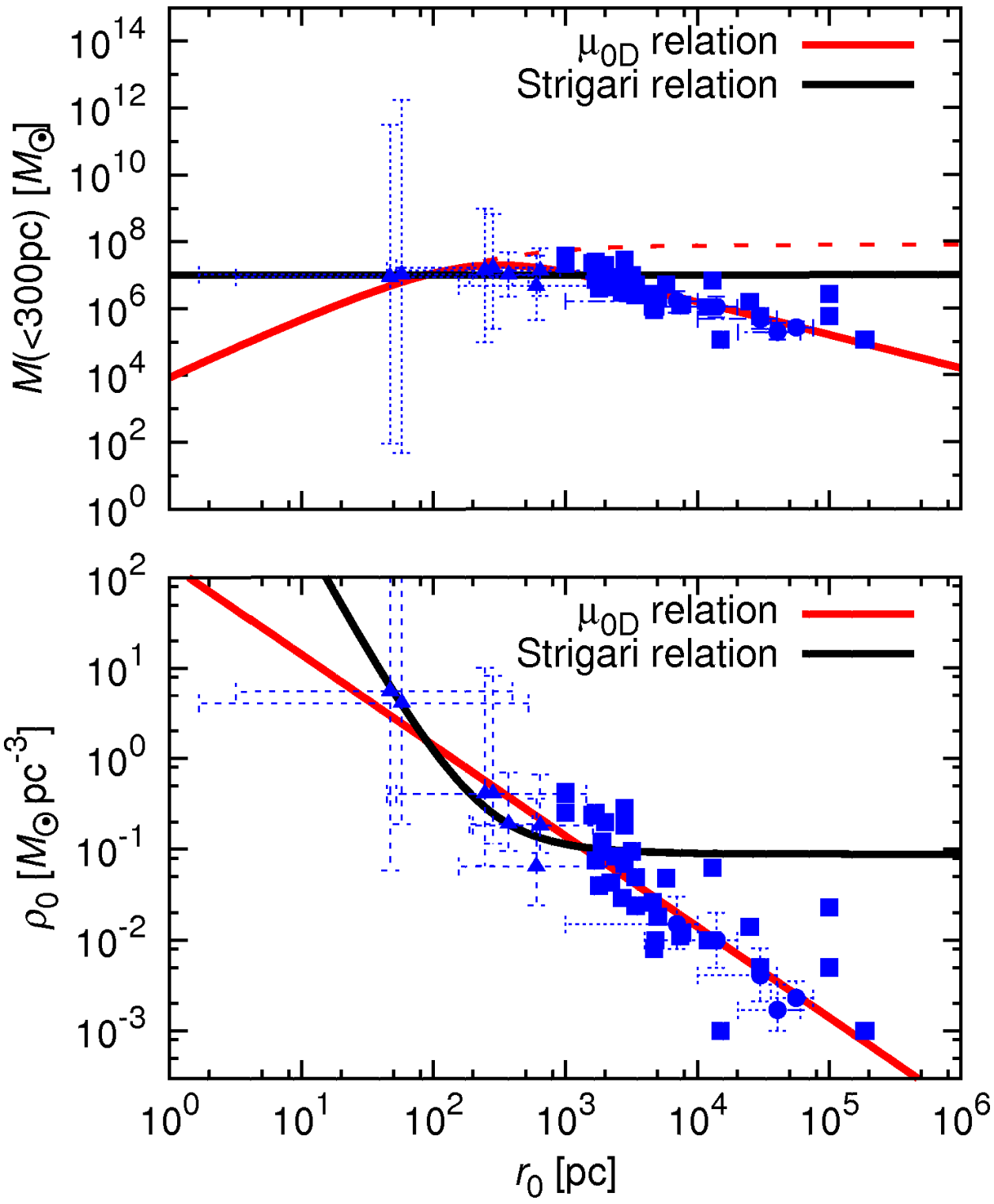

Fig. 2.3: (*Upper*) DM mass enclosed within 300pc, $M(<300\mathrm{pc})$, as a function of core radius, r_0. Symbols with error bars show the observations. The red, solid line depicts the $\mu_{0\mathrm{D}}$ relation. We show $M(<300\mathrm{pc})$ of NFW halos with the assumption of $\rho_s r_s = 140 M_\odot \mathrm{pc}^{-2}$ (red dashed). The black line shows Strigari relation. (*Lower*) The central density of Burkert profiles, ρ_0, is shown as a function of r_0. The black and red lines show Strigari and the $\mu_{0\mathrm{D}}$ relation, respectively. Each symbol represents same observed galaxy within Fig. 2.2.

2.5 Summary and Discussion

In this chapter, we have studied the relation between observational universalities of dark matter halos and the cusp–to–core transformation. We obtained three interesting results:

(1) We verified the dependence of the concentration parameter of NFW profiles, c, on virial mass of halo, M_{200}, and redshift, z, proposed by Prada et al. (2012) using the data of the cosmological simulation performed by Ishiyama et al. (2013). According to our analysis, the $c(M_{200}, z)$ proposed by Prada et al. (2012) is appropriate down to $M \sim 10^8 M_\odot$ which is the mass scale of dwarf galaxies.

(2) The cusp–to–core transformation shapes the $\mu_{0\mathrm{D}}$ relation naturally. The central density of the Burkert profile, ρ_0, is almost independent of M_{200}. We therefore can estimate the formation epoch of the respective halos from ρ_0. Our estimations are consistent with previous studies. The $\mu_{0\mathrm{D}}$ relation is a relict of the formation phase of DM halos and keeps a memory of their time of formation.

(3) We found that the $\mu_{0\mathrm{D}}$ and Strigari relations are consistent with each other among DM halos surrounding dSphs. However, this consistency breaks down for halos of more massive galaxies that have larger cores. The $\mu_{0\mathrm{D}}$ relation can be applied to a broader range of halo mass than Strigari relation. We conclude that Strigari relation is an indirect evidence of the $\mu_{0\mathrm{D}}$ relation.

The cusp–to–core transformation represents a viable model in order to explain the origin of these universalities. In our analyses, we assumed a transformation from NFW profiles to Burkert profiles. This assumption requires some mechanisms to flatten the cusps and to create the cores with sizes comparable to the scale lengths of the cuspy halo. This requirement might allow to distinguish between different models of core formation and might provide important constraints for them. It is not only the flattening of a cusp but also the formation of a reasonably sized core that these models have to generate.

An interesting question is whether the cusp–to–core transformation also solves the missing satellite (e.g., Moore et al. 1999a) problem. This might be difficult to achieve as obviously the cores are observed in dwarf galaxies that were not disrupted by internal processes or that became invisible because of quenching of star formation but that still experienced major changes in the gravitational potential leading to cores (see also Peñarrubia et al. 2012). In addition, it is also intersting about a weak dependence of a halo mass on the $\mu_{0\mathrm{D}}$ relation (Cardone & Tortora 2010; Boyarsky et al. 2010; Cardone & Del Popolo 2012).

It is noteworthy that the transformation redshifts of the Sextans and the Leo II dSphs, the leftmost points in Fig. 2.2, are beyond the redshift $z_\mathrm{t} = 10$. In such an early epoch, the gas is almost metal–free, and H_2 acts as a prime coolant (e.g., Galli & Palla 1998; Omukai & Nishi 1998; Bromm & Yoshida 2011, and references therein). Further studies about these galaxies may play a key role to unravel the formation of the first objects in the universe.

Part II

Numerical Simulation Code for GPU Clusters

Chapter 3 A Tree–SPH Code Developed for GPU Clusters

3.1 Introduction

Gravity is the most important physical process for the structure formation in the universe. N–body simulations are commonly used to investigate the formation and dynamical evolution of galaxies (e.g., Kazantzidis et al. 2006; Mori & Rich 2008; Ogiya & Mori 2011; Łokas et al. 2012; Ogiya & Mori 2012). In N–body simulations, systems are expressed by discretized N particles. We compute gravitational acceleration among particles and update their position and velocity iteratively. In most cases, it is impossible to let a particle correspond to a star because of huge amounts of computation and required memory. A particle is treated as an imaginary object with mass of (M/N), where M is the total mass of the system. In order to achieve high spatial resolution and to avoid the deterioration of the results caused by discretization, we have to employ particles as much as possible. On the other hand, the amount of computation increases with N.

The most straightforward and accurate algorithm to compute gravity among particles is the "direct" method. The computational cost is $\mathcal{O}(N^2)$, since we would have to compute gravitational acceleration between all pairs of particles. Therefore this algorithm is unfavorable to solve problems with large N. Hereafter, we call the particles for which the gravitational acceleration is computed the "i–particles" and call the particles that interact with i–particles the "j–particles". The equation of motion of the i–particle is represented by

$$\frac{d^2\mathbf{r}_\mathrm{i}}{dt^2} = -G\sum_{j\neq i}^{N}\frac{m_\mathrm{j}(\mathbf{r}_\mathrm{i}-\mathbf{r}_\mathrm{j})}{(|\mathbf{r}_\mathrm{i}-\mathbf{r}_\mathrm{j}|^2+\epsilon^2)^{3/2}}, \tag{3.1}$$

where $\mathbf{r}_\mathrm{i}$ and $\mathbf{r}_\mathrm{j}$ are the position vector of the i– and j–particles, respectively. G is the gravitational constant, and ϵ is called the softening parameter which prevents the numerical divergence. In N–body simulations of collisionless systems, ϵ is set to a positive constant and corresponds to the spatial resolution. It also have a role of smoothing the potential field which is important to represent collisionless systems by a finite number of particles. The tree method reduces the cost to $\mathcal{O}(N\log N)$ by treating a group of j–particles that are sufficiently far from the i–particle as a single heavy j–particle (Barnes & Hut 1986).

Graphics Processing Unit (GPU) attracts lots of attention as a powerful computing accelerator. Acceleration of the direct method has succeeded since the beginning of GPGPU (General-Purpose computation on GPU; e.g., Nyland et al. 2007; Elsen et al. 2007; Belleman et al. 2008; Miki et al. 2012, 2013). Recently, development environments, including CUDA (Compute Unified Device Architecture; NVIDIA 2011) which provided by NVIDIA and OpenCL (Open Computing Language; Khronos 2011) which formulated by Khronos Group, have been facilitated and more complicated algorithms have been accelerated (Hamada et al. 2009; Nakasato 2012; Yokota et al. 2011; Bédorf et al. 2012)

In this chapter, we improve the method to accelerate the tree algorithm on GPU proposed by Nakasato (2012). We parallelize the code with MPI (Message Passing Interface; MPI 2013) and measure the performance. The development environment adopted in this study is CUDA. We use GPUs made by NVIDIA, but our ideas are able to be applied to other environments.

The structure of this chapter is as follows. We describe the tree algorithm in §3.2. We provide overviews of CUDA and the method proposed by Nakasato (2012) in §3.3. In §3.4, we propose an improved method

to accelerate the tree algorithm on GPUs, and §3.5 shows the results of the performance measurements. In §3.6, we parallelize the code with MPI and show the performance. We describe the Smoothed Particle Hydrodynamics (SPH) and show the performance of our Tree–SPH code in §3.7. §3.8 provides the summary of this chapter.

3.2 Tree Method

The tree method consists of two parts, tree–construction and tree–traversal.

3.2.1 Tree Construction

In the first part, the tree–construction, we construct an oct–tree structure of particles. We split the cube containing all particles recursively into 8 (in 3D) smaller cubes (Figure 3.1), and we link all cubes to their daughter– and sister–cubes (Figure 3.2). Next– and More–pointers connect the sister– and daughter–cubes with the present cube. We continue the recursion until every cube contains less than or equal to $N_{\rm crit}$ particles. After the linking operation, we compute the mass and position of each cube. The mass of the cube is the sum of that of the contained particles, and its position is the center of mass of the contained particles.

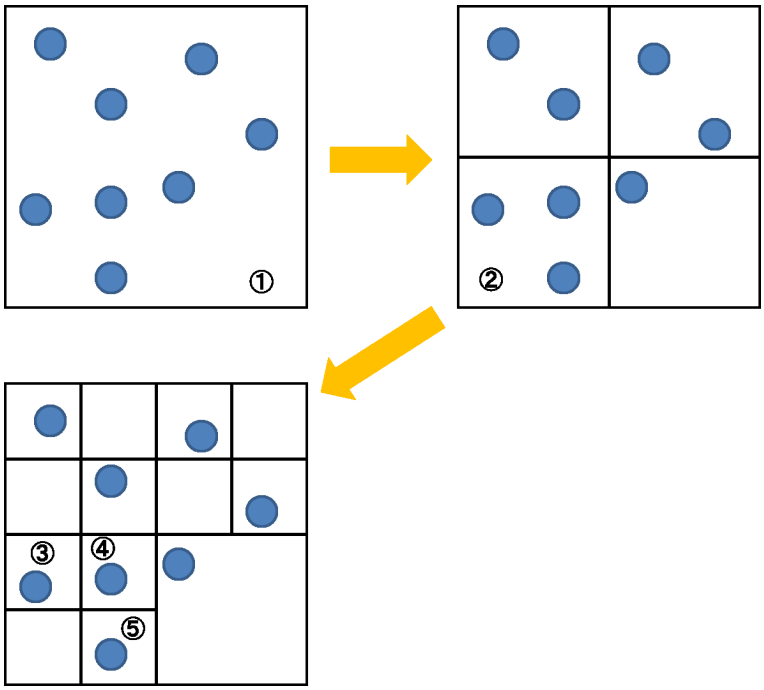

Fig. 3.1: Recursive splitting of cubes into 8 (in 3D) smaller cubes until all cubes contain less than $N_{\rm crit}$ particles (blue dots). In this schematic diagram, $N_{\rm crit}$ is 1. The particle ③ is a daughter of ② and ④ is a daughter of ③.

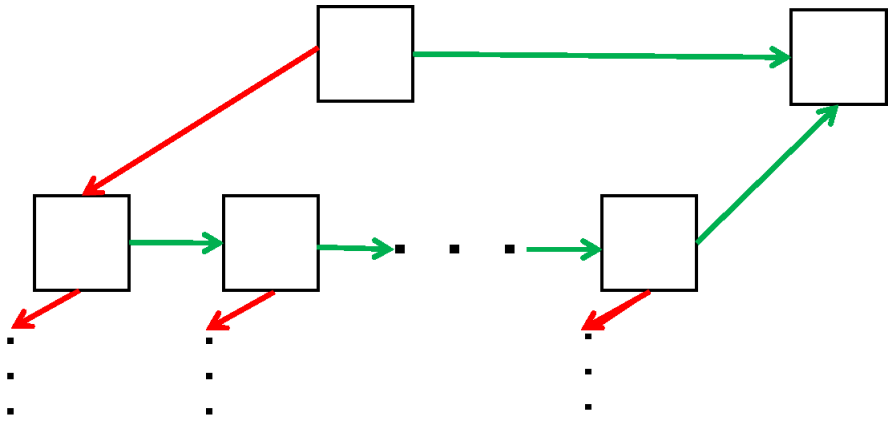

Fig. 3.2: Relation among cubes. Red and green lines represent pointers connected to daughter– and sister–cubes, respectively.

3.2.2 Tree Traversal

In the second part, the tree–traversal, we walk the tree constructed in the previous part for each i–particle. A cube is sufficiently far from an i–particle if its angular size is smaller than a critical size, θ. Here, we define a critical distance to judge cubes sufficiently far from the i–particle or not, $D_{\rm crit}$,

$$D_{\rm crit} \equiv l/\theta + s, \tag{3.2}$$

where l and s are the cube size and the distance from the geometric cube center to the center of mass in the cube, respectively. When we reach a cube for which

$$d \geq D_{\rm crit}, \tag{3.3}$$

we walk to a daughter–cube, where d denotes the distance from the i–particle to the cube. If we reach a cube for which

$$d < D_{\rm crit}, \tag{3.4}$$

we walk to a sister–cube (Figure 3.3). In the former case, j–particles contained in the cube are treated as a single heavy j–particle, reducing the cost of computation. The tree structure has about $\log N$ layers. Since we calculate gravitational force for N particles, the computation cost is $\mathcal{O}(N \log N)$. Since smaller θ leads to a larger amount of computation but provides a higher accuracy, since the fashion for gravity computing approaches that of the direct method. The tolerance paremeter, θ, is a constant number which satisfies $0 < \theta \leq 1$.

3.3 Overview of CUDA and Nakasato (2012)

In this section, we summarize CUDA and the method proposed by Nakasato (2012; hereafter N12). We argue for GPUs of compute capability 2.0 and CUDA version 4.0 (NVIDIA 2011).

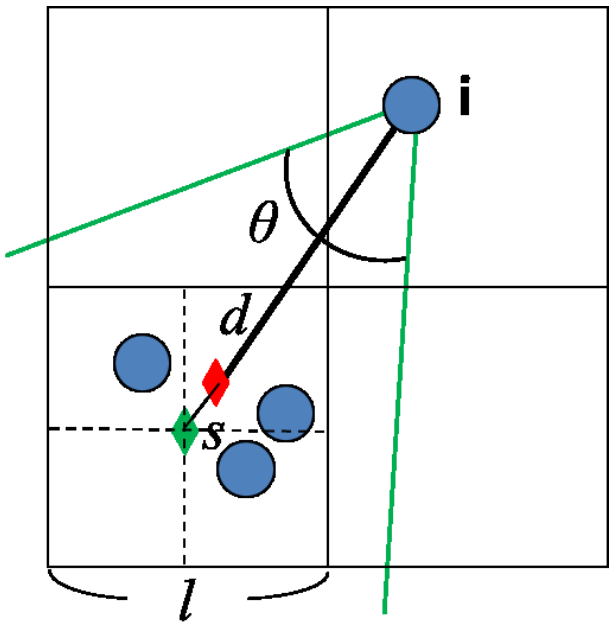

Fig. 3.3: Conceptual diagram of judgment with θ. Red and green points are the geometric cube center and the center of mass in the cube, respectively.

3.3.1 CUDA

CUDA is the development environment provided by NVIDIA. Bacause of a number of processors mounted on GPU cards, the theoretical peak performance of GPUs is much higher than that of high–end CPUs. In order to let processors work efficiently, we control them with imaginary units of processing, called "Thread", "Block", and "Grid". As shown in Figure 3.4, Block and Grid consist of Threads and Blocks, respectively. The numbers of Threads/Blocks per Block/Grid are controllable parameters. Actually, 32 CUDA cores are constituent of a streaming multiprocessor (SM). 16 SMs are mounted on an NVIDIA M2090 card and it has 512 CUDA cores in total.

Figure 3.5 shows a notable feature of GPUs, the hierarchical memory structure. The global memory has a large capacity (> GB) but the bandwidth is small compared with other memory areas. All CUDA cores can load/store data from/on the global memory. On the other hand, the capacity of registers which have a large bandwidths is small (a few hundreds bytes per core). Each CUDA core can access only assigned areas in the register. The bandwidth of the shared memory and level–1 (L1) cache is comparable to that of the register. They are assigned to the same memory area and can be accessed by CUDA cores which belong to the identical SM.

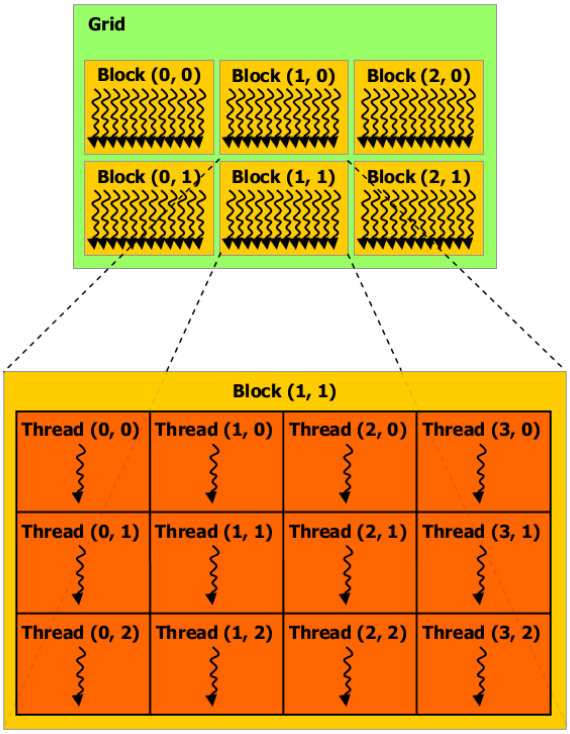

Fig. 3.4: Schematic diagram of imaginary units of processing. Quoted from NVIDIA CUDA C Programming Guide Version 4.0 NVIDIA (2011).

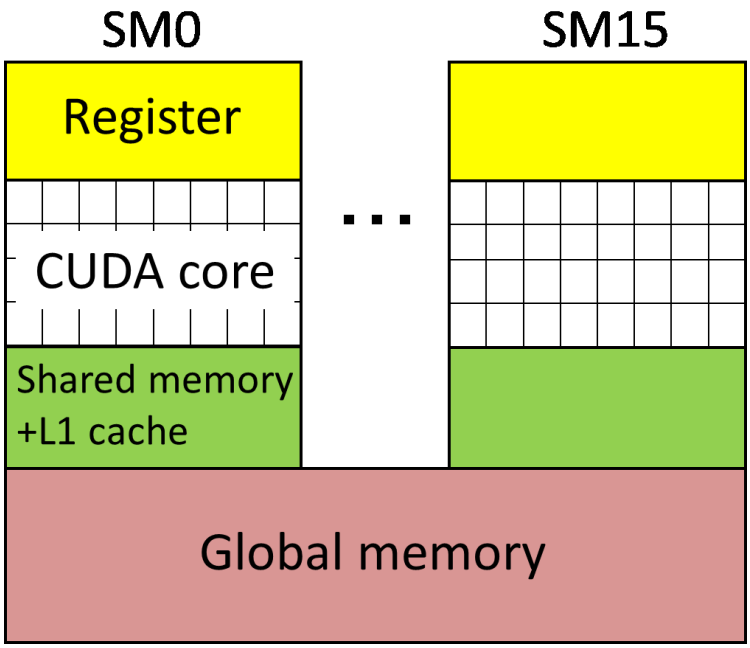

Fig. 3.5: Hierarchical memory structure of GPU (NVIDIA M2090).

3.3.2 Nakasato (2012)

In N12, CPU cores and GPU cards are designed to compute tree construction and to compute tree–traversal, respectively. The computation cost of the latter is much larger than that of the former. N12 proposed a method in which each Thread computes an i–particle through tree–traversal. In order to achieve a high performance, we have to reuse data on the shared memory/L1 cache. Because of the character of the tree method, utilizing the shared memory is not so easy. The bandwidth of the L1 cache is the same as that of the shared memory. Therefore, N12 made an effort to increase the frequency of L1 cache hit.

Geometrically neighbor particles are expected to have similar access patterns to the tree data. We assume that i–particles close in the memory space are assigned to the identical Blocks. Thus it is very important to collect geometrically neighbor particles close in the memory space, since CUDA cores are allowed to reuse the tree data copied on the L1 cache. N12 gave particles indices one–dimensionally by applying a kind of space–filling curve, "Morton curve" (Figure 3.6) and sorted them by obeying the indices in the memory space. N12 showed that this sorting of particle data made the computing speed of the tree–traversal on a GPU double. The tree construction part which computed by CPU cores was also accelerated because of the high cache hit rate.

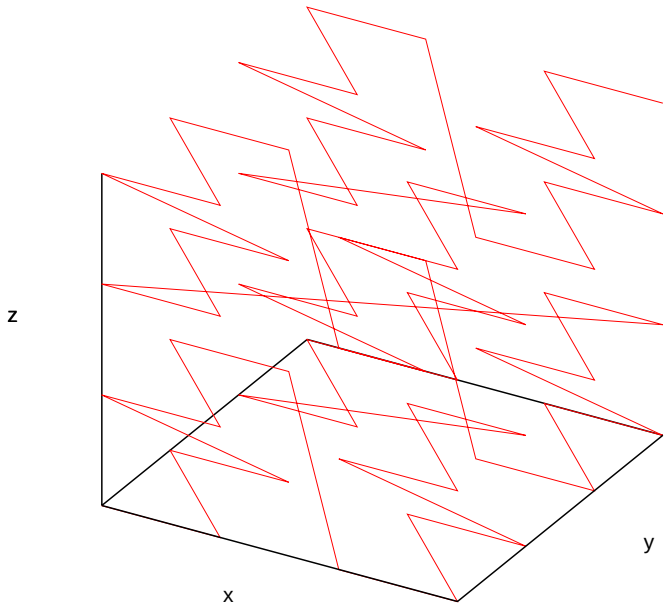

Fig. 3.6: Morton curve.

3.4 Proposing Method

In this section, we improve the method described in §3.3, and accelerate the tree–traversal on GPU further.

3.4.1 Vectorization and Grouping

"Warp branch" is an important issue in GPU computing. We explain the problem for the case of the NVIDIA Fermi architecture. In this architecture of GPUs, 32 cores work concurrently with the same instruction stream. In other words, CUDA cores work in the manner of SIMD (Single Instruction Multiple Data). This cluster of 32 cores is called a warp. When two or more different instructions emerge among the 32 cores, a large overhead arises because the instructions can only be processed sequentially within a warp. Therefore, we have to decrease the frequency of warp branches as much as possible.

Such warp branches occur in the tree–traversal part whenever we step to a daughter– or sister–cube. When the condition of Equation (3.4) is satisfied, each Thread just jumps to the daughter–cube pointed by the More–pointer. On the other hand, when Equation (3.3) is satisfied, each Thread jumps to the sister–cube pointed by the Next–pointer after calculating gravity between the i–particle and the j–cube. If there exist Threads which satisfy Equation (3.3), all Threads in the warp (32 CUDA cores) have to calculate gravity. For Threads which satisfy Equation (3.4), it is not necessary and leads to a large overhead. In this way, frequent warp branches will decrease the performance significantly. It is also important to decrease the frequency of accesses to the global memory since the access speed is very slow. Warp branches and accesses to the global memory will become less frequent if we bundle routes for given i–particles in the tree structure. The method of route bundling of i–particles is proposed by Barnes (1990). Bédorf et al. (2012) partially adopted it to accelerate the tree method on GPUs. To achieve this, we propose a method in 2 steps:

Vectorization

The first step is a "vectorization" step. We vectorize the operations of route selection in the tree structure and that of calculating gravitational acceleration for V i–particles, where V is the vector length or the number of particles per Thread. We show a conceptual diagram of this step in Figure 3.7. We bundle the routes of V i–particles in a Thread by measuring the distance to the cube from the nearest particle. We select the next step in the tree structure, a daughter– or sister–cube, by using the distance to the present cube from the nearest particle among the bundled ones which are circled red in Figure 3.7. If $d < D_{\rm crit}$ for the nearest particle, we take a step to a daughter–cube even if other particles are sufficiently far from the present cube. If $d \geq D_{\rm crit}$ for the nearest particle, we compute gravitational acceleration from that cube to the i–particles by using the respective distance between each i–particle and the cube. After that, the walk continue to a sister–cube. The frequency of warp branches drops with increasing vector length, V. Concomitantly with this, the frequency of accesses to the global memory will decrease. However, the amount of work per Thread is proportional to V. Thus it is not advisable to set V very large.

Vectorizing and grouping will decrease the frequency of warp branches and global memory accesses, but will increase the amount of computation. This is because, by choosing the particle in a vector or group the nearest to the cube, will reduce the number of particles for which $d \geq D_{\rm crit}$ and for which we could treat the cube as a single heavy j–particle. Thus we expect that there exist an optimal pair of values for the vector length and number of group members.

3.4.2 Peano–Hilbert Curve

As shown in N12, sorting of particle data obeying Morton curve in the memory space increases the cache hit rate. It is also effective to decrease the frequency of warp branches. Peano–Hilbert (PH) curve shown in Figure 3.9 is one of the space filling curves applied to manage one–dimensionally particles distribute in three dimensions.

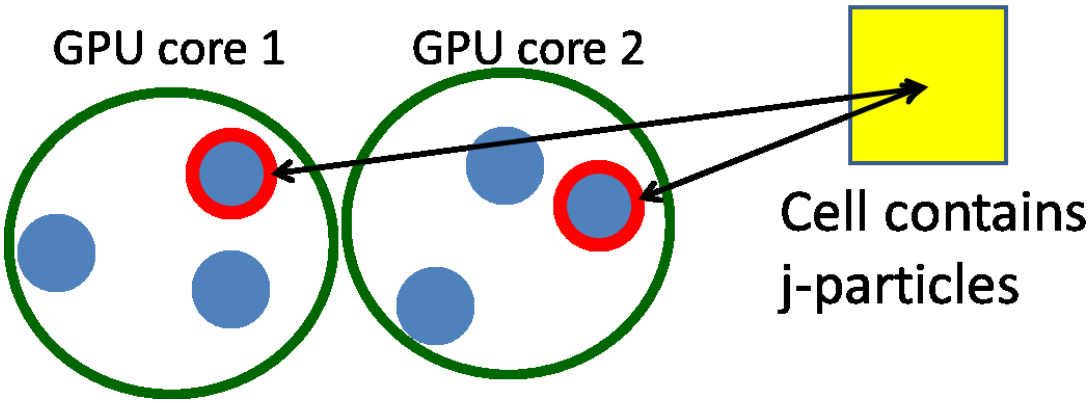

Fig. 3.7: Conceptual diagram of vectorization. Blue dots represent i–particles. The red circled particles are the closest ones to the cube of j–particles. In this case, each GPU core holds 3 i–particles ($V = 3$).

Grouping

The second step is a "grouping" step, which alleviates the problem of vectorization described above to some degree. As shown in Figure 3.8, we bundle routes for i–particles among several Threads in the same fashion as we bundle the routes for i–particle in a Thread. Again, the nearest particle in the group is circled red. We select the next step in the tree–traversal for i–particles by the value of the distance to a cube from the nearest particle. By grouping, we can increase the number of bundled i–particles without increasing the number of particles owned by a Thread. The number of bundled particles becomes $V \times G$, where G is the number of group members.

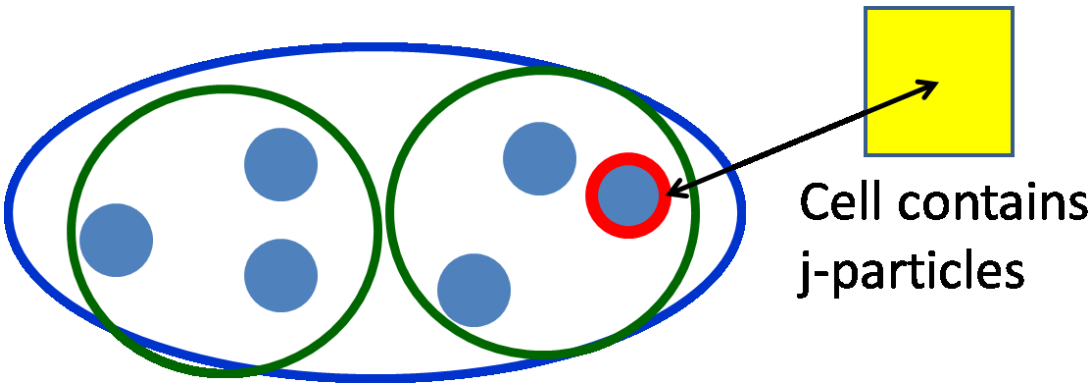

Fig. 3.8: Conceptual diagram of grouping. The same i–particles are shown as Figure 3.7. In this case, the number of group member, G, is 2, and 6 i–particles have been bundled into a group.

The Peano–Hilbert ordering of particles is very important in our method since bundling routes for spatially distant particles results in a large amount of unnecessary computations. Compared with Morton curve, the advantage of PH curve is the spatial "jump" is smaller than that of Morton one (see also Figure 3.6). Since Morton curve is drawn just like recursive drawing of "Z" symbols, the diagonal jump arises certainly. In this case, neighbor particles in the memory scape may not be located near in the real space. On the other hand, the gap between the memory and real spaces will be shrunk when we use PH curve, because it is extended to the nearby region. We extend an algorithm proposed by Lam & Shapiro (1994) to calculate

the indices of PH curve.

As described above, the PH ordering is expected to lead to increasing of the cache hit rate and decreasing of the frequency of warp branches. Such advantages should become obvious when we bundle the routes of i–particles in the tree structure. If we use the Morton ordering, a cluster of bundled particles might be decoupled into two groups by the spatial jump of the Z symbol. In such case, it becomes hard to satisfy the condition, Equation (3.3), and the amount of computation increases beyond necessity. Because the jumps in PH curve are smaller than those in Morton one, each Thread can traverse the tree structure more efficiently. For the same reason, the PH ordering has advantages over Morton curve. Although the computing cost of the index of PH curve is larger than that of Morton curve, it can be negligible. A famous open code for studying galaxy formation and evolution, GADGET–2 (Springel 2005) also uses the PH ordering.

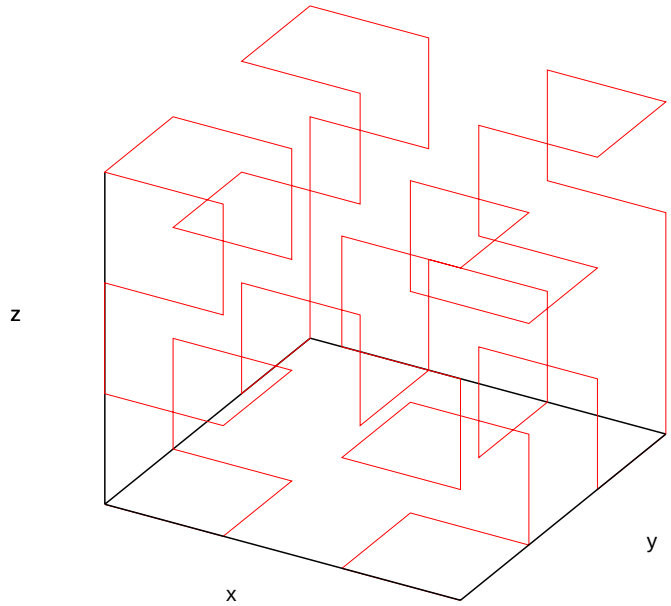

Fig. 3.9: Peano–Hilbert (PH) curve.

3.5 Performance Measurements of Tree–Traversal on Single GPU

In this section, we implement the vectorization, grouping, and PH ordering and measure the performance of tree–traversal on a single GPU.

3.5.1 Computing Environment for Performance Measurements

We measure the performance of our code on the GPU cluster, HA–PACS, which was installed at the Center for Computational Sciences of University of Tsukuba in 2012 (HA-PACS 2012). HA–PACS has 4 NVIDIA Tesla M2090 GPU cards per node. The specifications of HA–PACS are shown in Table 3.1. We argue MPI parallelization in §3.6.

In this test, we simply follow the evolution of particles initially distributed with the Navarro–Frenk–White (NFW) profile, which is often used for CDM halos (Navarro et al. 1997) and a random velocity field. We

Table. 3.1: Specification of performance measurement environment (HA-PACS).

CPU	Intel(R) Xeon(R) CPU E5-2670 2.60GHz (8 cores/socket × 2 sockets = 16 cores/node)
GPU	NVIDIA Tesla M2090 (4 GPUs / node)
Main Memory	128 GB, DDR3 1600MHz, 4 channel / socket, 102.8 GB/s/node
OS	CentOS release 6.1 (Final)
CPU Compiler	GCC 4.4.5-6
GPU Toolkit	CUDA 4.0.17
Interconnection	Infiniband QDR × 2 rails
MPI	MVAPICH2 1.7

set the tolerance parameter of the tree method, $\theta = 0.6$ which is the typical value for simulations of galaxy formation and evolution, and the critical number of particles to stop the tree construction, $N_{\rm crit} = 1$. The number of Threads per Block is 256 and the number of Blocks is $N/(256 \times V)$. In the following analyses, we use CUDA Profiler. It allows us to measure Occupancy (will be discussed below), the number of L1 cache hits/misses per SM, number of warp branches per SM, and usage of register per Thread and so on. Although measured values are not exact unless all SMs work identically, we apply them as representative ones.

3.5.2 Performance

Vectorization and Grouping

We set the number of particles, $N = 2^{23} \approx 8$ million. Particle data are sorted by obeying Morton curve. We measure the performance of the tree–traversal part which is computed by GPU for $(V, G) = (1, 1) \sim (8, 8)$. Since a warp consists of 32 Threads, we restrict the number of group member, G, to power of two. Because the number of particles, N, is also a power of two, we can not test for $V = 3, 5$ in which the residual exists.

Figure 3.10 demonstrates the effects of the vectorization and grouping by comparing runs with different combinations of V and G. Compared with the case of no vectorization or grouping, $(V, G) = (1, 1)$, tree–traversal becomes about 3.6 times faster. As expected, there exists an optimal pair of values for the vector length and the number of group members. In this test, the optimal pair is $(V, G) = (4, 4)$. In general, the optimal pair of values depends on the N–body problem and the GPU architecture.

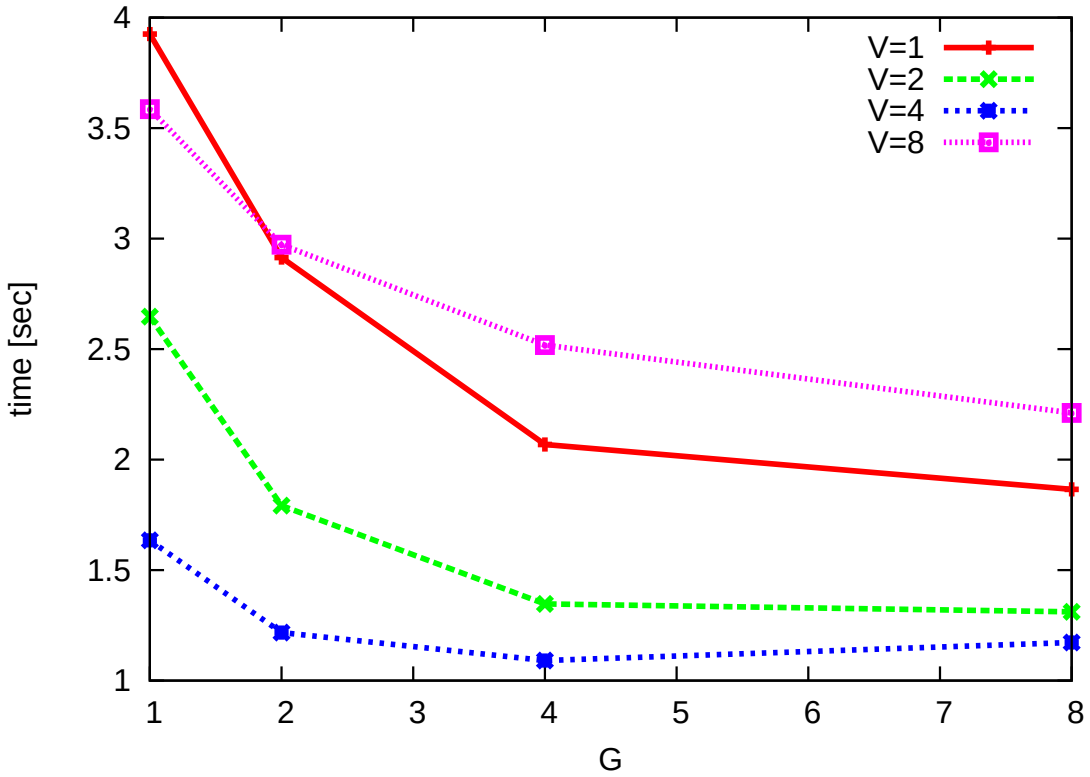

Fig. 3.10: Advantage due to vectorization and grouping on performance of the function of the tree–traversal. X– and Y–axes show the number of group members (G) and execution time, respectively. Respective lines show the results of $V = 1, 2, 4, 8$, where V means vector length.

In the following part of this section, we discuss the reason for the obtained performance distribution through several analyses.

At first, Figure 3.11 shows the rate of L1 cache hit as a fuction of V and G. For $V \leq 4$, we gain a high cache hit rate of more than 90%. However, for $V = 8$, the cache hit rate gets worse rapidly. Each Thread utilizes the register to memory data of i–particles (position etc.). When we raise V, the capacity of the register becomes insufficient. In this case, data of i–particles are spilled into the slow area, the local memory, and the performance falls to a low level. Table 3.2 shows the usage of the register for each V. We fix the number of group members, $G = 1$. Fermi architecture can assign up to 48 warps per SM (called active state). Occupancy=1.0 means 48 warps are in the active state. Here, we evaluate the total amount of used register by (Number of Threads per warp)×(Number of warps work concurrently)×(Used register per Thread)=32 × (48 × Occupancy)× (Used register per Thread). To memory the data of an i–particle, about 44 bytes are required. For $V = 1 \rightarrow 2$ and $V = 2 \rightarrow 4$, the amount of used register per Thread increases along with this law approximately. However, for $V = 4 \rightarrow 8$, the amount of used register per Thread increases by only 8 bytes. NVIDIA Tesla M2090 has registers of 131072 bytes per SM. When we set $V = 8$, the amount of the register becomes insufficient. Figure 3.11 also shows that larger G leads to higher cache hit rate. This is because of the efficient reuse of the tree data which have been copied onto the L1 cache.

Table. 3.2: Register usage.

V	Occupancy	Used Registers per Thread [Bytes]	Total Used Registers [Bytes]
1	0.667	108	110592
2	0.5	152	116736
4	0.333	244	124928
8	0.333	252	129024

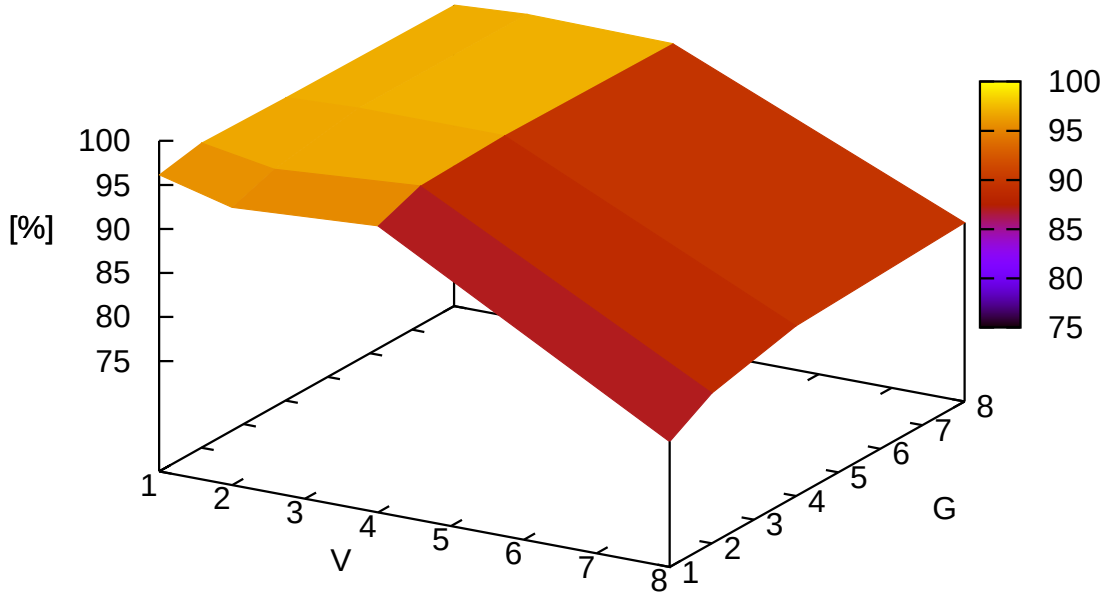

Fig. 3.11: L1 cache hit rate. X–, Y– and Z– axes mean V, G and L1 cache hit rate for each (V, G), respectively.

We estimate the number of memory accesses by summing the numbers of L1 cache hits and misses. Here, we assume a L1 cache miss corresponds to a global memory access. Figure 3.12 shows the number of memory accesses per particle. Using CUDA Profiler, we measure the number of L1 cache hits/misses per SM. Since 16 SMs have been mounted on an NVIDIA M2090 card, we evaluate the number of memory accesses by (Number of L1 cache hits + misses)/SM $\times$ 16 / N. As expected, the number of memory accesses decreases with increasing of V and G.

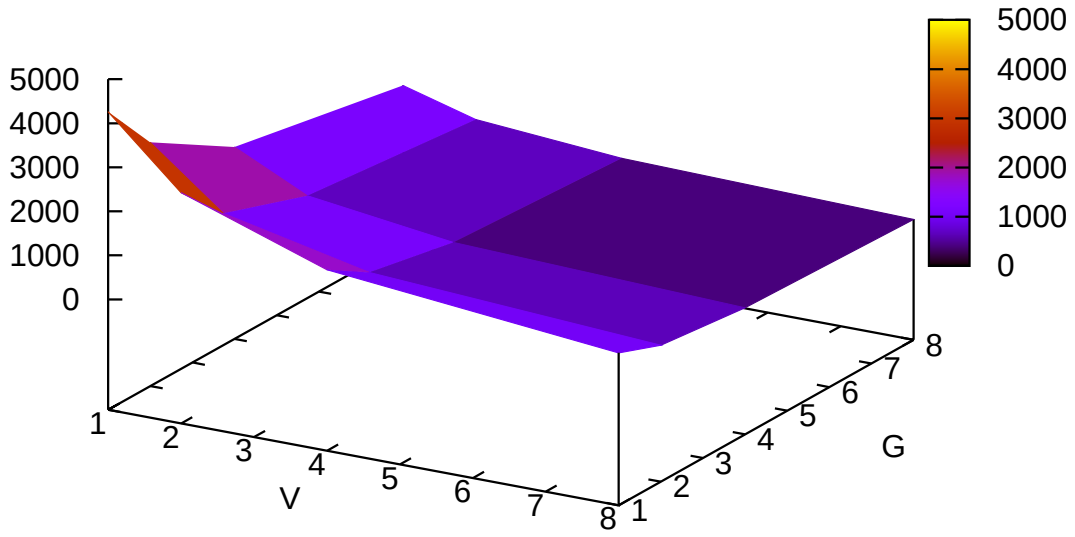

Fig. 3.12: Number of memory accesses per particle. X–, Y– and Z– axes mean V, G, and number of memory accesses per particle for each (V, G), respectively.

We demonstrate the dependence of the number of warp branches on V and G in Figure 3.13. Setting larger (V, G) corresponds to the route bundling of a larger number of i–particles. Thus the number of warp branches becomes small when we set a large (V, G). We estimate the the number of warp branches per particle by (Number of warp branches/SM) $\times$ 16 / N.

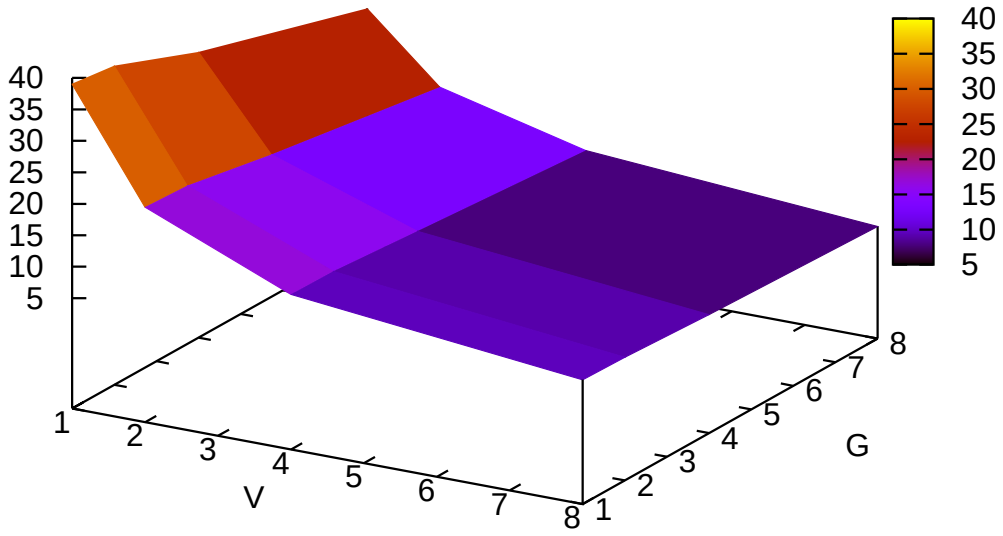

Fig. 3.13: Number of warp branches per particle. X–, Y– and Z– axes mean V, G, and number of warp branches per particle for each (V, G), respectively.

Figure 3.14 shows the number of gravity computation between the representative i–particle and j–cubes as a function of V and G. We choose a particle located in the center of the N–body system as the representative. The number of gravity computation of the representative is $4-5$ times larger than that of particles which locate at the outskirt when we set $(V, G) = (1, 1)$. As expected, larger (V, G) makes i–particles hard to satisfy $d \geq D_{\mathrm{crit}}$ and leads to the increasing of the number of gravity computation. In addition, it also causes frequent measurements of distances between i–particles and cubes and the amount of computation increases.

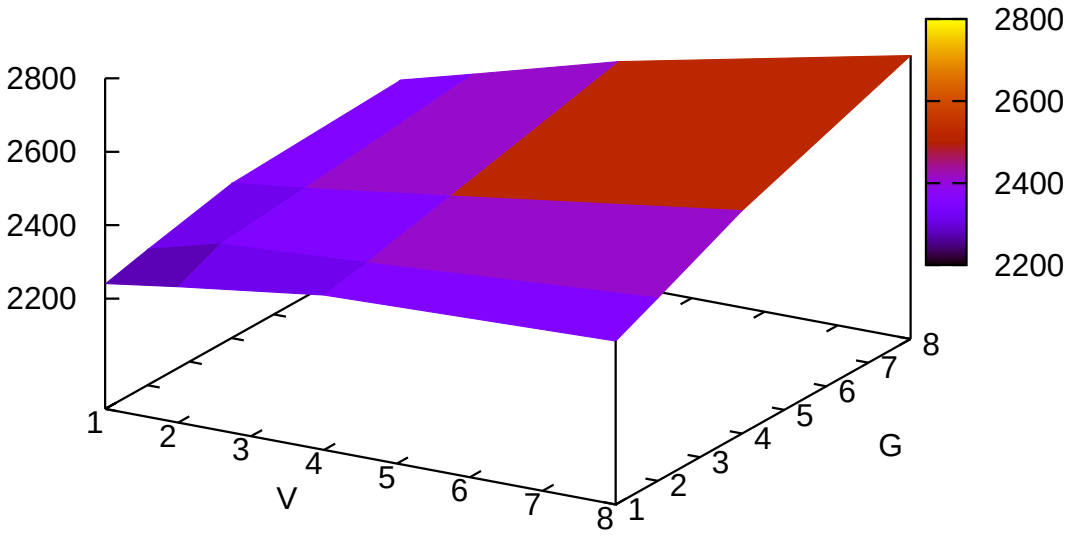

Fig. 3.14: Number of gravity computation between the representative i–particle and j–cubes. X–, Y– and Z– axes mean V, G, and number of gravity computation for each (V, G), respectively.

We summarize the effects of the vectorization and grouping as follows. As shown in Figure 3.10, the vectorization and grouping dramatically accelerate the function of the tree–traversal on GPU, and there exists an optimal pair of values for the vector length and number of group members to gain the maximal performance. This result is due to the complex web of the following factors.

1. The rate of L1 cache hit decreases when we set too large V (disadvantage for the performance). This is caused by the spill of the i–particle data from the register to the slow memory area.
2. Large (V, G) leads to the decreasing of the frequency of warp branches (advantage), since it corresponds to the route bundling of a large number of i–particles.
3. When we set large (V, G), the number of memory accesses decreases (advantage).
4. Setting larger (V, G), to satisfy the condition, $d \geq D_{\mathrm{crit}}$, becomes harder and the amount of calculation increases (disadvantage).

At the moment, the optimal pair of (V, G) should be searched by the survey of parameters. It might be possible to model the advantages and disadvantages analytically, and to estimate the optimal pair. However,

it should strongly depend on the distribution of particles. Applying this idea to the problems of astrophysics in which the particle distribution changes with time is difficult. In practice, it may be valid to search the optimal pair of (V, G) experimentally during computation.

Morton Curve vs Peano–Hilbert Curve

We test the effects of the PH ordering by comparing the performance with that applying the Morton ordering. We set $N = 2^{17} \sim 2^{23}$, $(V, G) = (4, 4)$. Other parameters are the same as those in the previous test.

Figure 3.15 shows the speed–up rate of adopting PH curve over Morton one. Applying PH curve, the tree–traversal has been accerelated by about 10 %. Combining with the acceleration due to the vectorization and grouping, the tree–traversal becomes $3.6 \times 1.1 \sim 4$ times faster. The speed–up rate may depend on the distribution of particles. We adopt a spherical model in this test. The advantage of PH curve for the localization in the memory space is expected to become more obvious if the particles distribute inhomogeneously. Such inhomogeneous distributions often arise in the astrophysical simulations.

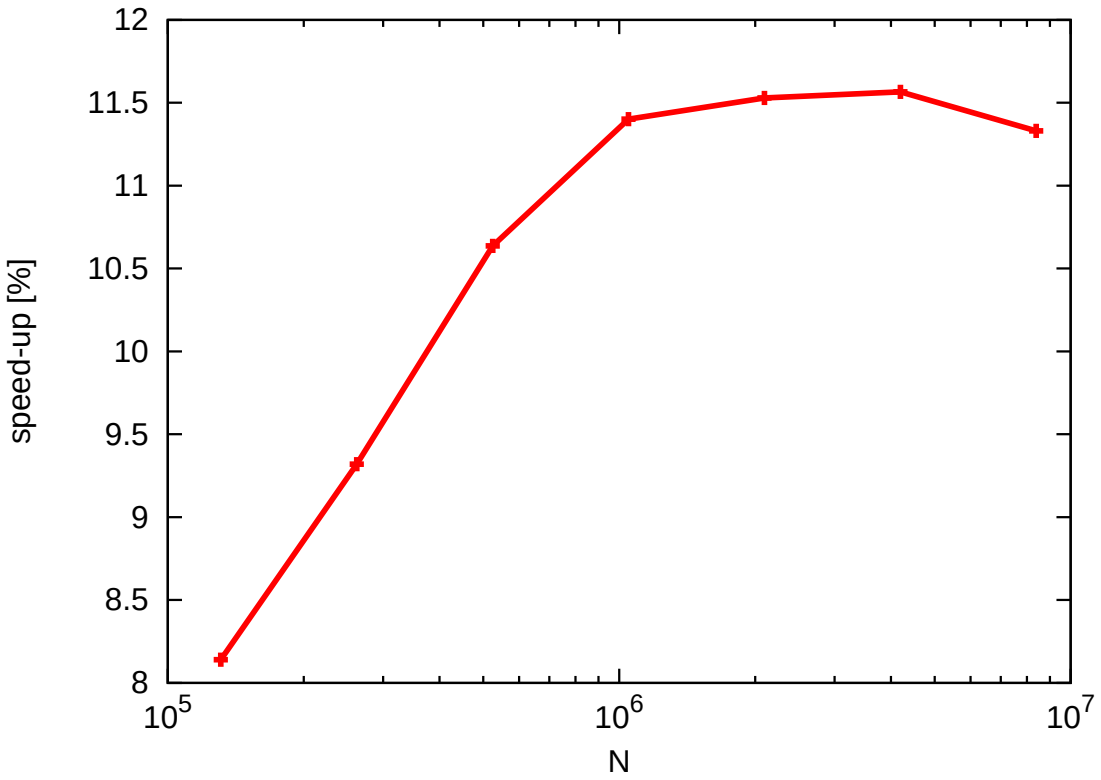

Fig. 3.15: Speed–up rate of adopting PH curve against Morton curve. X– and Y– axes mean the number of particles (N) and speed–up rate, respectively.

In Figure 3.16, we demonstrate the comparison of the number of warp branches adopting Morton or PH curve for the sorting of particle data. The number of warp branches becomes smaller when we adopt PH curve owing to the smaller gap. Since the number of tree layers increases with N, the number of warp branches also increases. It causes the grow of the speed–up rate shown in Figure 3.15. The reason for the saturation of the speed–up rate is still unclear. According to our measurements, the cache hit rate does not depend on the choosing of the space–filling curves. Therefore, we conclude that using the PH ordering, the tree–traversal is accelerated because of the decrease of the number of warp branches.

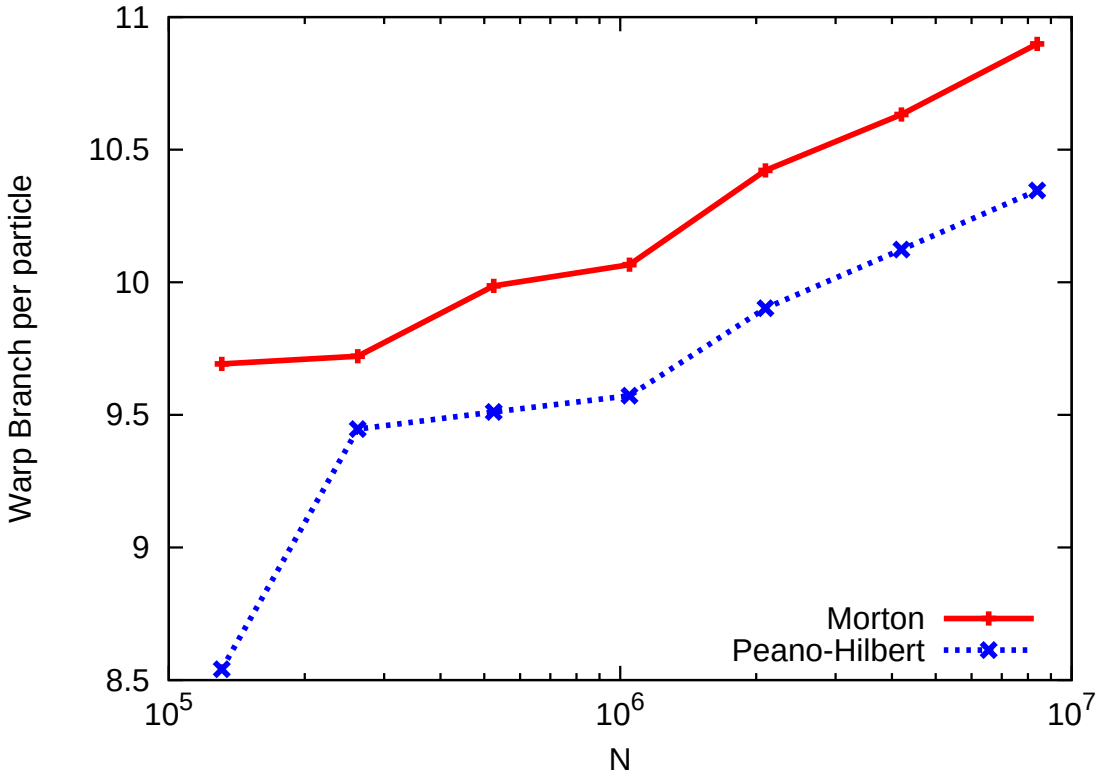

Fig. 3.16: Comparison of the number of warp branches adopting Morton or PH curve for sorting of particle data. X– and Y–axes mean N and number of warp branches per particle, respectively.

Although PH curve has an advantage in the performance of the tree–traversal, the cost for the index computation is about 3 times higher than that of Morton curve. However, the sorting of particle data is not a necessary procedure in every time–step. We can alleviate the increase of the cost by reducing the frequency of the procedure for the particle sorting. This is justified because the particle distribution does not change significantly in several time–steps. Hence, the cost for the index computation is not a problem for the performance of the whole code.

3.6 MPI Parallelization

We have parallelized the tree–construction and tree–traversal operations with MPI. N particles are sorted according to the Peano–Hilbert space–filling curve, and $N/N_{\rm p}$ particles are assigned to each MPI process, where $N_{\rm p}$ is the number of MPI processes or GPU cards.

We now check the performance of the whole code. The tree–construction, tree–traversal, and the construction of the minumum partial trees that are communicated to other processes (Locally Essential Tree; LET) take up most of the computational time. This method is proposed by Warren & Salmon (1993). The execution times of making LET and communications are overlapped by that of the GPU function traversing partial trees constructed personally.

In the following performance measurements, we set $\theta = 0.6$, $N_{\rm crit} = 4$, and $(V, G) = (4, 4)$. The number of Threads per Block is 256 and the number of Blocks is $N/(256 \times V \times N_{\rm p})$. Particles distribution follows the NFW profile.

3.6.1 Strong Scaling

Figure 3.17 shows the performance for strong scaling as a function of $N_{\rm p}$. We set the total number of particles, $N = 2^{24} \approx 16$ million. When $N_{\rm p} < 10$, the scaling is good. However, the performance saturates for $N_{\rm p} > 10$. We suspect the reason for the performance saturation of the GPU function (blue line) is the worsening load balance among MPI processes. Because we have sorted and assigned $N/N_{\rm p}$ particles to each process, some processes are assigned particles from the central part of the computational domain while others are assigned from the outskirts of the domain. The number of cubes encountered in the tree–traversal for these processes can differ in this test by a factor ~ 5. To improve the load balance, we need to change the way to assign particles to processes. The execution times of making LET and communications have been hided by that of the GPU function traversing partial trees constructed personally in $N_{\rm p} < 32$. The former exceeds the latter in $N_{\rm p} \geq 32$ and blue line represents the former. This can be understood as follows: The number of cubes contained in a LET decreases along with $N_{\rm p}^{-1}$. However, the number of LETs is $(N_{\rm p} - 1)$. Hence, the execution time of LET construction is almost independent of $N_{\rm p}$. Since the execution time of the GPU function traversing partial tree decreases with $N_{\rm p}$, that of LET construction and communications exceeds it. For the same reason, the execution time of the GPU function traversing LETs (magenta line) is almost constant, and it becomes one of the dominant parts when $N_{\rm p} > 10$.

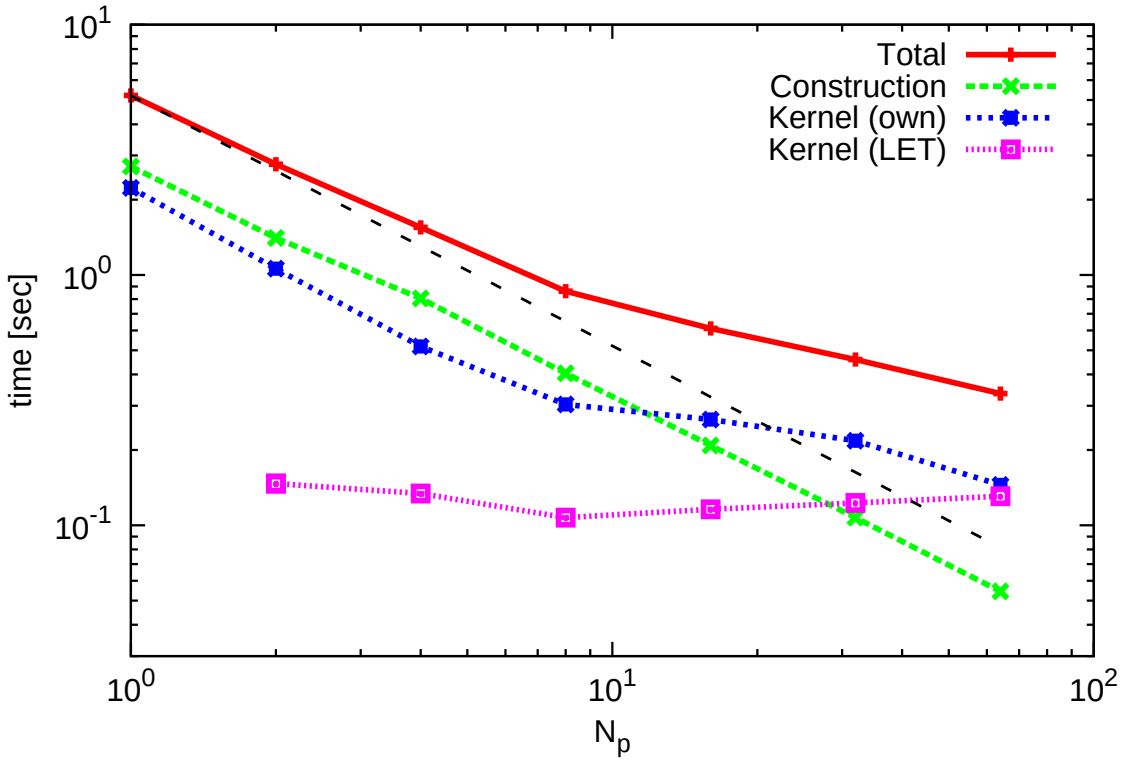

Fig. 3.17: Strong scaling performance ($N = 2^{24}$). X– and Y–axes mean number of MPI processes ($N_{\rm p}$ as well as number of GPUs) and execution time, respectively. Red and green lines represent the total execution time and tree construction, respectively. Blue and magenta ones represent the execution times of the GPU function traversing partial trees constructed personally and by other processes, respectively. Black one is the ideal scaling, $\propto N_{\rm p}^{-1}$.

3.6.2 Weak Scaling

We show the performance for weak scaling in Figure 3.18. Each process holds $N_1 = 2^{24} \sim 16$M particles. The total number of particles is $N = N_1 \times N_p$. The expected scaling is proportional to $\log N_p$ (black line). This can be explained as follows: The computational cost of the tree method is $\mathcal{O}(N \log N) = \mathcal{O}(N_1 N_p \log N_1 N_p)$. Through parallelization, it becomes $\mathcal{O}(N_1 \log N_1 N_p)$. Since N_1 is a constant, the computational cost will be proportional to $\log N_p$. In other words, the depth of the tree structure is proportional to $\log N \propto \log N_p$. When $N_p < 10$, the total execution time (red line) follows this scaling well. However, in $N_p > 10$, it grows faster than the expected scaling, because of the performance worsening of the GPU function (blue and magenta lines). The execution time of making LETs and communications are overlapped by that of the GPU function traversing partial trees constructed personally when $N_p < 16$. The former exceeds the latter, and blue line means the execution time for making LET and communications in $N_p \geq 16$. The execution time of the GPU function traversing LETs is approximately proportional to N_p. Since the geometrically overlaps of the assigned computational domain arise in our implementation, we suspect the reason for the worsening of the GPU function (megenta line) is that the increasing of the particle–particle interactions just like the direct method in the overlapping regions. In that case, since the calculation of $\mathcal{O}(N^2) \propto \mathcal{O}(N_p^2)$ is parallelized by N_p processes, the computation time will be proportional to N_p. We expect that this issue will be solved by jointing LETs before traversing LETs to reduce the number of disjunctions of the tree structure.

Considering the performance of our code quantitatively, it computes the gravity among a billion particles within about 18 seconds per time ($N_p = 64$). We can perform simulations with such a number of particles within a reasonable computation time using this code.

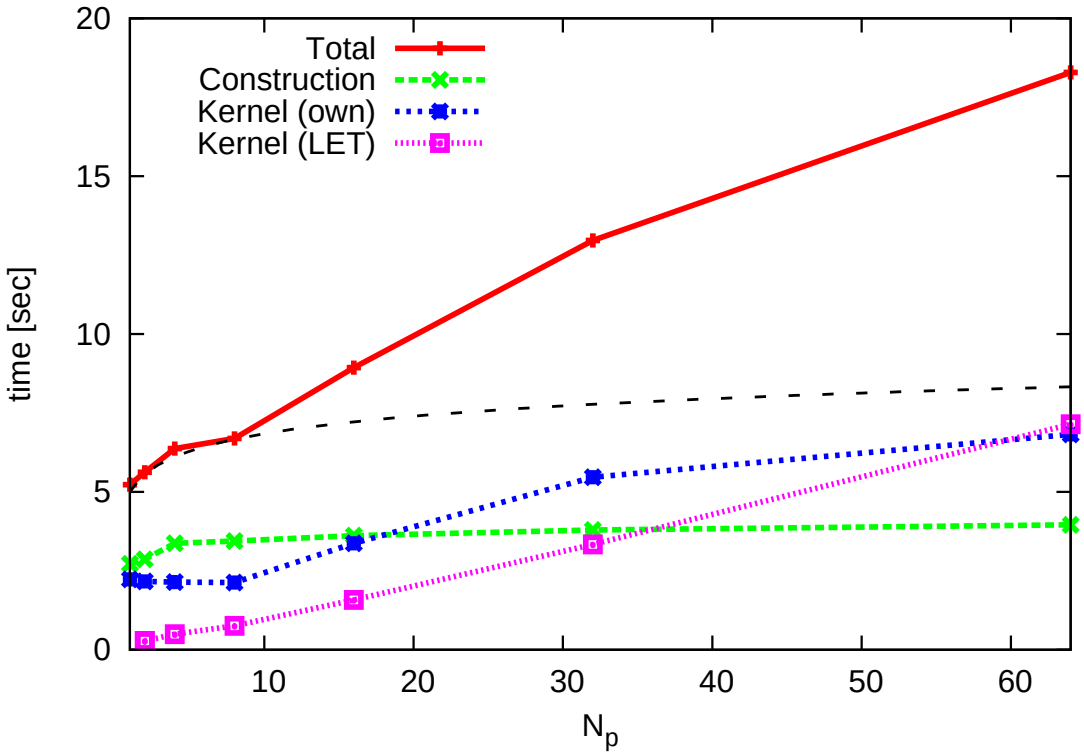

Fig. 3.18: Weak scaling performance. Number of particles per MPI process, $N_1 = 2^{24}$. Each axis and line have same meaning with in Figure 3.17. Black line shows expected scaling, $\propto \log N_p$. In $N_p \geq 16$, blue line means the execution time for making LET and communications.

3.7 Extension to Smoothed Particle Hydrodynamics

The Smoothed Particle Hydrodynamics (SPH) is a Lagrangian scheme to solve the dynamics of fluid. It was developed by Gingold & Monaghan (1977) and Lucy (1977) originally to solve astrophysical problems and has been widely used in the various research areas of astrophysics (e.g., Monaghan 1992, 2005; Rosswog 2009; Springel 2010; Price 2012, and references therein). In this section, we extend our tree code to SPH. There exists a good synergy between the tree method and SPH (Hernquist & Katz 1989).

3.7.1 Overview of SPH

In SPH, physical quantities are defined by the kernel interpolants,

$$< f > (\mathbf{r}) = \int f(\mathbf{r}')W(|\mathbf{r}-\mathbf{r}'|, h)d\mathbf{r}', \tag{3.5}$$

where W is the "kernel function" and h is the characterictic width of the kernel, so called the smoothing length. In practice, we know physical quantities only at a set of discrete points (i.e., position of particles). Thus we approximate the integration in Equation (3.5) by a summation. We can estimate a quantity, f, of the i–particle by

$$f(\mathbf{r}_\mathrm{i}) \approx \sum_\mathrm{j} f(\mathbf{r}_\mathrm{j})W(|\mathbf{r}_\mathrm{i}-\mathbf{r}_\mathrm{j}|, h_\mathrm{i})\Delta V_\mathrm{j}, \tag{3.6}$$

where $\mathbf{r}_\mathrm{i}$ and $\mathbf{r}_\mathrm{j}$ are the position vectors of the i– and j–particles, respectively. We assume that each particle has an independent smoothing length, h_i (mentioned below). In the standard SPH formulation, the finite volume element, ΔV is defined by

$$\Delta V_\mathrm{j} \equiv m_\mathrm{j}/\rho_\mathrm{j}, \tag{3.7}$$

where m_j and ρ_j are the mass and mass–density of the j–particle, respectively. For example, the mass–density of the i–particle is evaluated by

$$\rho_\mathrm{i} = \sum_\mathrm{j} m_\mathrm{j}W(|\mathbf{r}_\mathrm{i}-\mathbf{r}_\mathrm{j}|, h_\mathrm{i}) = \sum_\mathrm{j} m_\mathrm{j}W_\mathrm{ij}(h_\mathrm{i}). \tag{3.8}$$

$W_\mathrm{ij}(h_\mathrm{i})$ is defined by

$$W_\mathrm{ij}(h_\mathrm{i}) \equiv W(|\mathbf{r}_\mathrm{i}-\mathbf{r}_\mathrm{j}|, h_\mathrm{i}). \tag{3.9}$$

The kernel function, W, is normalized to unity and approaches a Dirac's δ–function in the limit of $h \to 0$. It also has a symmetric property and is differentiable. The cubic spline is usually adopted

$$W(|\mathbf{r}-\mathbf{r}'|, h) \equiv \frac{1}{\pi h^3}\begin{cases} 1-\frac{3}{2}q^2+\frac{3}{4}q^3, & (0 \le q < 1) \\ \frac{1}{4}(2-q)^3, & (1 \le q < 2) \\ 0, & (2 \le q) \end{cases} \tag{3.10}$$

where $q = |\mathbf{r}-\mathbf{r}'|/h$.

Since the kernel function is supported in a finite region, we only have to compute interactions between the i–particle and j–particles within $|\mathbf{r}_\mathrm{i}-\mathbf{r}_\mathrm{j}| \le 2h$. The tree structure of particles allows us to search such "neighbor particles" efficiently (Hernquist & Katz 1989). Through the tree traversal, i–particles find their neighbors and estimate physical quantities, such as the mass–density, pressure gradient and so on.

3.7.2 Density Independent SPH

SPH is a developing scheme and has been improved (e.g., Springel & Hernquist 2002, and references therein). Agertz et al. (2007) compared the simulation results of SPH and Eulerian codes, and pointed

out that the Kelvin–Helmholtz instability (KHI) was suppressed in simulations applying standard SPH formulation. Okamoto et al. (2003) have reported similar results. Recently, Saitoh & Makino (2013) clarified the reason for the suppression of KHI and proposed a novel formulation of SPH which clears such difficulty.

The KHI suppression is caused by the unphysical tention at the contact discontinuity. In the standard SPH formulation, the pressure gradient term of Euler equation is estimated using the mass–density. At the contact discontinuity, the densities of the low– and high–density regions are overestimated and underestimated, respectively. This error causes the overestimation/underestimation of the pressure in the low/high density region. As a result, unphysical repulsive force appears at the contact discontinuity and suppresses KHI. In the new formulation proposed by Saitoh & Makino (2013), the density of the internal energy, q, which corresponds to the pressure is adopted as the most fundamental quantity in substitution for the mass–density. The finite volume element is defined by

$$\Delta V \equiv U/q, \tag{3.11}$$

where U means the internal energy. The new type of SPH named density independent SPH (DISPH) handles the contact discontinuities, KHI and the Rayleigh–Taylor instabilities well.

The energy density of the i–particle, $q_{\rm i}$, is estimated by

$$q_{\rm i} = \sum_{\rm j} U_{\rm j} W_{\rm ij}(h_{\rm i}). \tag{3.12}$$

The equation of motion and energy equation are represented by

$$m_{\rm i}\frac{d^2\mathbf{r}_{\rm i}}{dt^2} = -(\gamma-1)\sum_{\rm j} U_{\rm i}U_{\rm j}\left[\frac{1}{q_{\rm i}}f_{\rm i}^{\rm grad}\nabla_{\rm i}W_{\rm ij}(h_{\rm i}) + \frac{1}{q_{\rm j}}f_{\rm j}^{\rm grad}\nabla_{\rm i}W_{\rm ij}(h_{\rm j})\right], \tag{3.13}$$

$$\frac{dU_{\rm i}}{dt} = (\gamma-1)\sum_{\rm j}\frac{U_{\rm i}U_{\rm j}}{q_{\rm i}}f_{\rm i}^{\rm grad}\mathbf{v}_{\rm ij}\cdot\nabla_{\rm i}W_{\rm ij}(h_{\rm i}), \tag{3.14}$$

respectively. Here, γ means the specific heat ratio, and $f_{\rm i}^{\rm grad}$ is the factor to take account the effects caused by change of the smoothing length, and is defined by

$$f_{\rm i}^{\rm grad} = \left(1 + \frac{h_{\rm i}}{3q_{\rm i}}\frac{\partial q_{\rm i}}{\partial h_{\rm i}}\right)^{-1}. \tag{3.15}$$

The gradient operator, $\nabla_{\rm i} = \partial/\partial\mathbf{r}_{\rm i}$, and $\mathbf{v}_{\rm ij} = \mathbf{v}_{\rm i} - \mathbf{v}_{\rm j}$. These equations are derived from the Lagrangian formulation. As a constraint condition,

$$\frac{4\pi}{3}(2h_{\rm i})^3\frac{q_{\rm i}}{U_{\rm i}} = N_{\rm ngb}, \tag{3.16}$$

is adopted for each particle. $N_{\rm ngb}$ is the number of neighbor particles. Equation (3.16) means that the spherical region with the radius $2h_{\rm i}$ covers a volume of $N_{\rm ngb}\Delta V_{\rm i}$. We determine $h_{\rm i}$ by requiring that a fixed number of particles, $N_{\rm ngb}$, is contained within the volume.

We adopt the DISPH formulation in our code.

3.7.3 Artificial Viscosity

In SPH simulations, we have to add a dissipation term, so called the artificial viscosity, to Equations (3.13) and (3.14) in order to deal with shocks. The terms of the artificial viscosity in the equation of motion and energy equation are represented by

$$\left(m_{\rm i}\frac{d^2\mathbf{r}_{\rm i}}{dt^2}\right)_{\rm vsc} = -m_{\rm i}\sum_{\rm j} m_{\rm j}\Pi_{\rm ij}\nabla\tilde{W}_{\rm ij}, \tag{3.17}$$

$$\left(\frac{dU_{\rm i}}{dt}\right)_{\rm vsc} = \frac{m_{\rm i}}{2}\sum_{\rm j} m_{\rm j}\Pi_{\rm ij}\mathbf{v}_{\rm ij}\cdot\nabla\tilde{W}_{\rm ij}, \tag{3.18}$$

where $\tilde{W}_{ij} = 0.5[W_{ij}(h_i) + W_{ij}(h_j)]$, and Π_{ij} is a function to determine the strength of the artificial viscosity. We adopt the artificial viscosity function proposed by Monaghan (1997),

$$\Pi_{ij} = \begin{cases} -\frac{\alpha}{2}\frac{v_{ij}^{sig} w_{ij}}{\rho_{ij}}, & (\mathbf{v}_{ij} \cdot \mathbf{r}_{ij} < 0) \\ 0, & (\mathbf{v}_{ij} \cdot \mathbf{r}_{ij} \geq 0) \end{cases} \tag{3.19}$$

Here, $\mathbf{r}_{ij} = \mathbf{r}_i - \mathbf{r}_j$, $w_{ij} = \mathbf{v}_{ij} \cdot \mathbf{r}_{ij}/r_{ij}$ and $\rho_{ij} = 0.5(\rho_i + \rho_j)$, respectively. Throughout this thesis, the control parameter, $\alpha = 3$. Although it is possible to evaluate the mass–density by

$$\rho_i = \frac{m_i q_i}{U_i}, \tag{3.20}$$

we use Equation (3.8), since Equation (3.20) leads to unstable behavior under strong shocks (Saitoh & Makino 2013). Equation (3.19) was derived from the analogy of the Riemann solver and shows that the artificial viscosity decays when the distance between the i– and j–particles increases. The signal velocity, v_{ij}^{sig}, is defined by

$$v_{ij}^{sig} \equiv c_{s,i} + c_{s,j} - 3w_{ij}, \tag{3.21}$$

where c_s means the sound speed.

In addition, we adopt the standard Balsara switch (Balsara 1995) in order to suppress the shear viscosity,

$$F_i^{Balsara} = \frac{|\nabla \cdot \mathbf{v}_i|}{|\nabla \cdot \mathbf{v}_i| + |\nabla \times \mathbf{v}_i| + \epsilon_b c_{s,i}/h_i}, \tag{3.22}$$

where ϵ_b is a small constant value. Throughout this thesis, we set $\epsilon_b = 10^{-4}$. We can evaluate the divergence and rotation of the velocity by

$$\nabla \cdot \mathbf{v}_i = -\frac{1}{q_i}\sum_j U_j \mathbf{v}_{ij} \cdot \nabla W_{ij}(h_i), \tag{3.23}$$

$$\nabla \times \mathbf{v}_i = -\frac{1}{q_i}\sum_j U_j \mathbf{v}_{ij} \times \nabla W_{ij}(h_i), \tag{3.24}$$

(cf. Monaghan 1992). The net viscosity is

$$\Pi_{ij}^{Balsara} = 0.5(F_i^{Balsara} + F_j^{Balsara})\Pi_{ij}. \tag{3.25}$$

3.7.4 Time–Step

We adopt a time varying step size, Δt, for the time integration of particle orbits in simulations. Here, all particles always have same Δt, so called "shared time–step". We determine Δt for the next step by

$$\Delta t = \min\left[C_{VA}\frac{\epsilon}{v_{max}}, C_{VA}\sqrt{\frac{2\epsilon}{a_{max}}}, C_{CFL}\left(\frac{h}{v^{sig}}\right)_{min}\right], \tag{3.26}$$

where v_{max} and a_{max} are the maximums of the absolute values of the particle velocity and acceleration, respectively. They are evaluated every time from the particle data of velocity/acceleration. Here, C_{VA} and C_{CFL} are the parameters to control the accuracy of the time integration. Throughout this thesis, $C_{VA} = 0.5$ and $C_{CFL} = 0.25$. In N–body simulations, we use only the first two conditions of Equation (3.26). They are imposed to prevent moving or accelerating of particles larger than the softening length, ϵ, in a step. The last condition is the Courant–Friedrichs–Lewy (CFL) condition.

3.7.5 Performance of Our Tree–SPH Code

Here, we measure the performance of our Tree–SPH code for the self–gravitational fluid. In this test, a glass–like particle distribution is used, and the velocity of gas particles is $\mathbf{v} = 0$ initially. We set the tolerance parameter of the tree method, $\theta = 0.6$, the critical number of particles to stop the tree construction, $N_{\rm crit} = 4$, and the number of neighbor particles for SPH computation, $N_{\rm ngb} = 32 \pm 3$. The number of Threads per Block is 256 and the number of Blocks is $N/(256 \times V \times N_{\rm p})$.

We implement four GPU functions to calculate (1) the mass– and energy–density, (2) divergence and rotation of the velocity, (3) pressure gradient and change ratio of the internal energy, and to determine (4) the smoothing length. The vectorization and grouping are implemented and accelerate the some of the GPU functions by $\sim 2-3$ times. The optimal pairs of respective functions are $(V, G)_1 = (4, 16)$, $(V, G)_2 = (2, 32)$, $(V, G)_3 = (1, 1)$, and $(V, G)_4 = (1, 1)$, respectively. We adopt them in this test.

Figure 3.19 shows the performance for weak scaling. Each process holds $N_1 = 2^{19} \sim 512$K particles. The total number of particles is $N = N_1 \times N_{\rm p}$. We know that the expected scaling is proportional to $\log N_{\rm p}$ by analogy with the performance measurement for weak scaling shown in §3.6.2, but the total execution time is almost constant in this test. The execution time of the GPU function to calculate the pressure gradient and rate of the energy variability, (3), is about double of those of others. Other GPU functions take approximately same time for calculation. Here, the GPU function to determine the smoothig length is performed one time out of ten. Although the breaking the constraint of the constant number of neighbor particles is possible, our code works well. For example, the total energy is well conserved and the test of the Sedov–Taylor problem (e.g., Sedov 1959) is passed. Hence we adopt this recipe throughout this thesis. The performance of the GPU function to compute gravity is lower than that shown in the previous sections. This may be due to the data alignment in the memory space. The amount of data required to compute SPH is larger than that to compute gravity (e.g., velocity, smoothing length, internal energy). This causes the increasing of the number of accesses to the global memory and decreasing of the cache hit rate, and the performance has been lowewed. By optimizing the data alignment, we will resolve such issue. The performances of other functions are also expected to be improved.

3.8 Summary

In this chapter, we have developed a fast tree code designed for GPU clusters. We improve the method proposed by Nakasato (2012), and accelerate the tree–traversal on GPUs further. In order to gain a high rate of L1 cache hit and to decrease the frequency of warp branches and number of accesses to the global memory, the vectorization and grouping, route bundling of i–particles while they traverse the tree structure, are devised and implemented. Thanks to these methods, the tree–traversal part on GPU becomes 3.6 times faster. Applying Peano–Hilbert curve in substitution for Morton curve which adopted in Nakasato (2012), the GPU function is accelerated by 10 %. Combining all of them, we have made the tree–traversal 4 times faster.

The code is parallelized with MPI. The policy is similar to that adopted in parallelized CPU codes. Our code has achieved a performance to compute the gravity among a billion particles within about 18 seconds per time ($N_{\rm p} = 64$). Thus we can perform simulations with such a number of particles within a reasonable computation time.

We have extended the code to the Smoothed Particle Hydrodynamics (SPH). The vectorization and grouping also accelerate some of GPU functions implemented for SPH. As future work, there is still room for improvement.

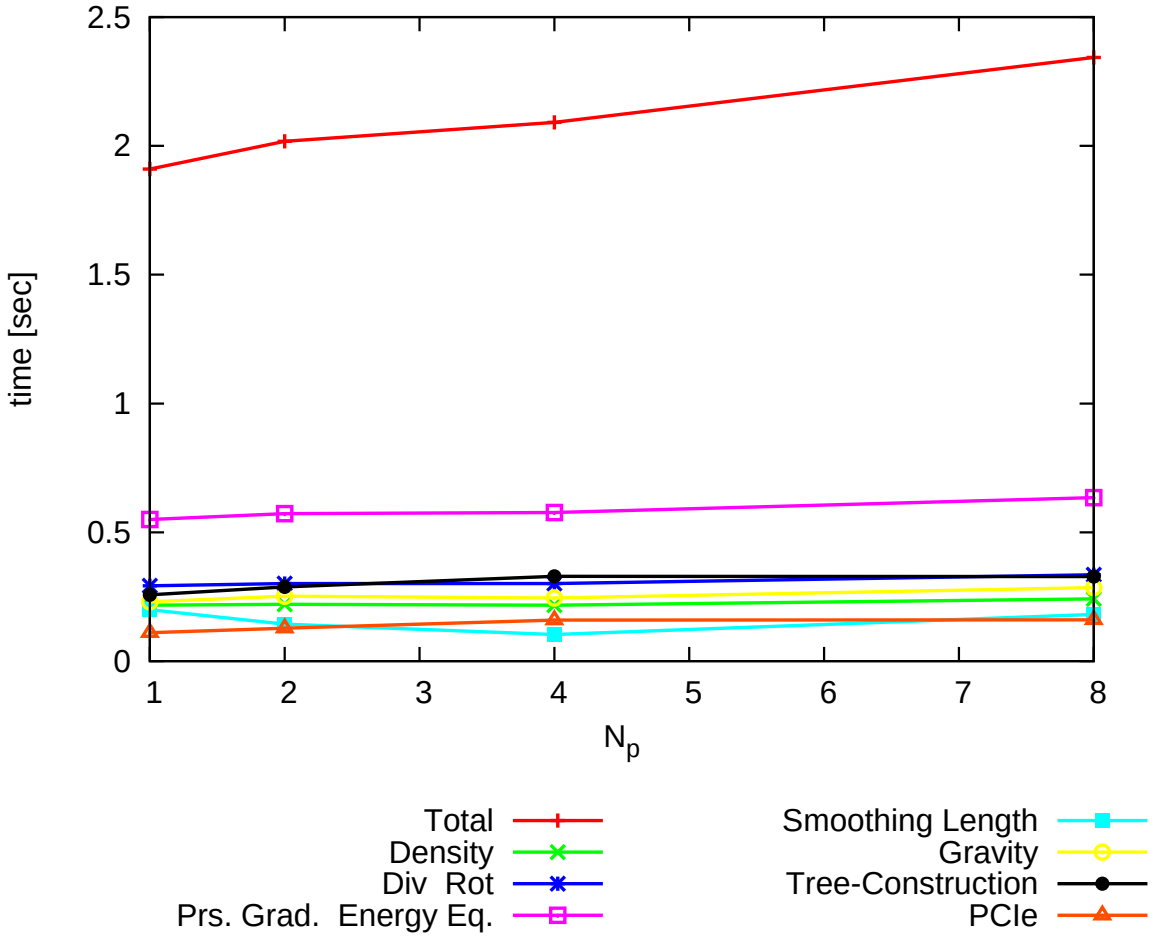

Fig. 3.19: Weak scaling performance of our Tree–SPH code. Number of particles per MPI process, $N_1 = 2^{19}$. X– and Y–axes are the number of MPI processes (N_p as well as number of GPUs) and execution time, respectively. Red line is the total execution time. Green, blue, magenta, and sky–blue lines represent the execution time of the GPU functions for (1) the mass– and energy–density, (2) the divergence and rotation of the velocity, (3) the pressure gradient and rate of the energy variability, and (4) the smoothing length, respectively. Yellow, black and orange lines mean the GPU function to compute gravity, tree construction and data transfer between CPUs and GPUs, respectively.

Part III

Dynamical Effects of Gravitational Potential Change Driven by Stellar Feedback on Dark Matter Halos

Chapter 4 Dynamical Effects of Gas Mass–Loss on Dark Matter Halos

4.1 Introduction

The present standard paradigm of structure formation in the universe, cold dark matter (CDM) cosmology, has several serious-unsolved problems. One of them is well known as the core–cusp problem. To solve this problem, so far, numerical simulations and analytical methods have been used to study the dynamical response of dark matter (DM) halos to the variance of the gravitational potential. Supernova feedback to the interstellar medium plays a significant role on forming less massive galaxies, because such galaxies have a shallower gravitational potential well than giant galaxies. The effects of stellar feedback differ substantially from one galaxy to another depending on the gravitational potential (e.g., Mori et al. 1999; Mac Low & Ferrara 1999). In low-mass dwarf galaxies, supernovae blow gas out from the galaxy centers. This mass loss makes the gravitational potential around the center of the DM halos shallower, and the mass-density distribution has a flat core (e.g., Navarro et al. 1996a; Read & Gilmore 2005). These previous works have always assumed that mass–loss from the center of DM halos occurs instantaneously or within a fixed period (see also Gnedin & Zhao 2002). However, the timescale of mass loss may be also a key factor in determining the dynamical response of DM halos. Furthermore, each dwarf galaxy in the local group has a unique star formation history (e.g., Mateo 1998; Weisz et al. 2011). de Souza et al. (2011) analytically demonstrated that the energy gain of particles flattens the central cusp; however, they assumed that each particle receives an equal amount of energy. This assumption must be verified by numerical simulations with sufficient accuracy. Therefore, in this chapter, we run collisionless N-body simulations that focus on the dependence of the dynamical response of DM halos on the timescale of gravitational potential variance. In other words, we study how the dynamics of DM halos depend on star formation activities. We demonstrate that the timescale of mass loss is one of the important factors in determining the dynamical response of DM halos. Finally, we discuss the surprising result: the mass loss of the baryon is not an effective mechanism for flattening the central cusp.

The structure of this chapter is as follows. In §4.2, we describe the numerical simulations. In §4.3, we show the simulation results. Finally, we discuss the results in §4.4.

4.2 Numerical Models

4.2.1 The DM Halo Model

The density distribution of a DM halo obtained from N-body simulations based on CDM cosmology is well fitted by the following:

$$\rho_{\rm DM}(r) = \frac{\rho_0 R_{\rm DM}^3}{r^\alpha (r + R_{\rm DM})^{3-\alpha}} \tag{4.1}$$

where r is the distance from the center of a DM halo, α is a power-low index, and ρ_0 and $R_{\rm DM}$ are the scale density and scale length of the DM halo, respectively. The density distribution changes from $\rho \propto r^{-\alpha}$ in the center of a DM halo ($r < R_{\rm DM}$) to $\rho \propto r^{-3}$ its outskirts ($r > R_{\rm DM}$). Here, $\alpha = 1.0$ corresponds to the Navarro–Frenk–White (NFW) model (Navarro et al. 1996b, 1997) and $\alpha = 1.5$ corresponds to the

Fukushige–Makino–Moore (FMM) model (Fukushige & Makino 1997; Moore et al. 1999b). To generate equilibrium N-body systems, we use the fitting formulation of the distribution function (DF) proposed by Widrow (2000). In this case, the DF only depends on energy, and the velocity dispersion of the system is isotropic.

4.2.2 The Baryon Model

Hernquist model (Hernquist 1990) is frequently used to describe bulges or elliptical galaxies, because its surface brightness profile matches de Vaucouleurs law (de Vaucouleurs 1948). Therefore, we adopt the Hernquist potential to describe the baryon potential around the center of DM halos. The external potential is given by

$$\Phi_{\rm b}(r) = -\frac{GM_{\rm b}}{r + R_{\rm b}} \tag{4.2}$$

where G is the gravitational constant, and $M_{\rm b}$ and $R_{\rm b}$ are the baryon mass and scale length of the external potential, respectively. To generate the initial condition, we relax the equilibrium N-body system quoted above in the external baryon potential for $\sim 30\ t_{\rm d}$, where $t_{\rm d}(r)$ is the dynamical time defined by

$$t_{\rm d}(r) = \sqrt{\frac{3\pi}{32G\bar{\rho}(< r_{\rm d})}} \tag{4.3}$$

where $\bar{\rho}(< r)$ is the average density of a DM halo within a radius $r = 0.2$ kpc throughout this chapter. Then, to represent baryon ejection from the center of galaxies, we change the baryon mass $M_{\rm b} = M_{\rm b,tot}(1-t/T_{\rm out})$, where $M_{\rm b,tot}$ and $T_{\rm out}$ are the total baryon mass and the timescale of mass loss. For the instantaneous mass-loss model, we simply set $M_{\rm b} = 0$.

4.2.3 Description of Runs

Here, we simulate the dynamical response of a DM halo with the virial mass $M_{\rm vir} = 10^9 M_\odot$, the virial radius $R_{\rm vir} = 10$ kpc, and the scale length $R_{\rm DM} = 2$ kpc. In this case, the mean dynamical time within 200 pc is $t_{\rm d} = 4$ Myr for the FMM model and 10 Myr for the NFW model. The total baryon mass is $M_{\rm b,tot} = 1.7 \times 10^8 M_\odot$, and the scale length of the baryon potential is $R_{\rm b} = 0.04$ kpc. Here, we assume that the total baryon mass included in the dwarf galaxies is initially 17% of the halo mass. This fraction matches the cosmic baryon fraction, $f_{\rm b}$, obtained from Wilkinson Microwave Anisotropy Probe (*WMAP*) observations (Spergel et al. 2007; Komatsu et al. 2009, 2011). The adopted parameters for each of our simulations are given in Table 4.1. Numerical simulations are performed applying an MPI parallelized tree–code for "CPU" clusters (we use the Tree–SPH code developed in chapter 3 in the following chapter). Throughout this chapter, the opening parameter of the Barnes–Hut tree algorithm (Barnes & Hut 1986) is $\theta = 0.8$ and the softening parameter is $\epsilon = 0.008$ kpc. The second-order Runge-Kutta scheme is employed as the time integration method.

Table. 4.1: Summary of simulation run

ID	DM halo	N	$T_{\rm rel}$	Mass-loss ($T_{\rm out}$)	Fitted α
UP1	FMM	1,048,576	495 $t_{\rm d}$	-	
UP2	FMM	16,384	7.74 $t_{\rm d}$	-	
UP3	NFW	1,048,576	148 $t_{\rm d}$	-	
UP4	NFW	16,384	2.32 $t_{\rm d}$	-	
ML1	FMM	1,048,576	495 $t_{\rm d}$	instantaneous	0.85
ML2	FMM	1,048,576	495 $t_{\rm d}$	1 $t_{\rm d}$	1.20
ML3	FMM	1,048,576	495 $t_{\rm d}$	10 $t_{\rm d}$	1.44
ML4	FMM	1,048,576	495 $t_{\rm d}$	50 $t_{\rm d}$	1.46
ML5	NFW	1,048,576	148 $t_{\rm d}$	instantaneous	0.42
ML6	NFW	1,048,576	148 $t_{\rm d}$	50 $t_{\rm d}$	0.89

Note: ML indicates mass–loss runs, and UP indicates unperturbed runs to examine the stability of the N–body system and the effects of two–body relaxation. $T_{\rm rel}$ is a two–body relaxation time within 0.2 kpc (Binney & Tremaine 2008).

4.3 Simulation Results

In this section, we present the simulation results showing the evolutionary processes in the instantaneous and quasi–adiabatic mass–loss models.

4.3.1 Dynamical Evolution of DM Halos

We show how the density profile of a DM halo evolves after mass loss for the instantaneous mass-loss case with the FMM initial condition (ML1) at the left panels in Figure 4.1. During the first $\sim 30\ t_{\rm d}$ (see Figure 4.1b), the system expands and the central cusp is flattened to the core. In this phase, the bulk of particles in the center of DM halo moves outward, and then the self–gravity of the DM halo slows the particles. After 30 $t_{\rm d}$, the particles lose their radial velocity and fall back into the center. In Figure 4.1c-4.1d, these particles assemble at the center of the halo, and the cusp is regenerated. This cusp regenerating process occurs from the center to the outward, and finally, the system reaches the quasi-equilibrium state (see Fig 4.1e). We emphasize that the central cusp has been regenerated, but the power–law index of density at the center $\alpha = 0.85$ is smaller than the initial condition $\alpha = 1.5$. A similar phenomenon occurs for the instantaneous mass–loss case with the NFW initial condition (ML5): the density at the center is $\alpha = 0.42$ for the initial condition $\alpha = 1.0$. Therefore, instantaneous mass–loss flattens the central cusp in the density distribution to some degree.

In the right panels of Figure 4.1, we show how the density profile of a DM halo evolves during and after mass–loss for the slow (quasi–adiabatic) mass–loss case with the FMM initial condition (ML4). Before the mass–loss operation, the DM halo has a high central density because of the baryon potential; this density decreases with decreasing baryon mass. Slow mass–loss does not significantly flatten the central cusp in the density distribution. Moreover, the system always keeps the virial state for the slow mass–loss process, and the final density profile of the DM halo recovers the FMM initial condition. A similar phenomenon occurs for the adiabatic mass–loss case with the NFW initial condition (ML6).

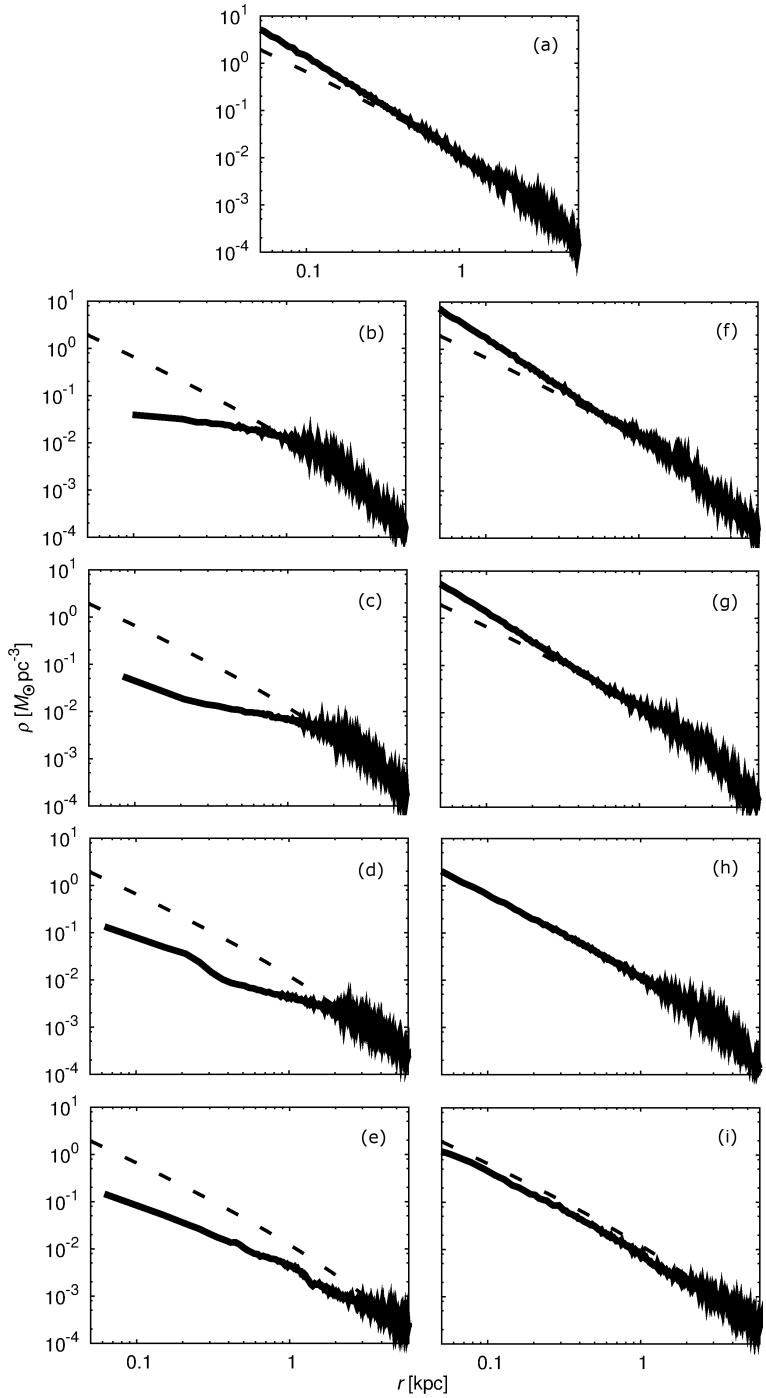

Fig. 4.1: Evolution of the density profiles of a DM halo for the instantaneous mass–loss model (ML1; left panels) and the adiabatic mass–loss model (ML4; right panels). The top panel (a) shows the density profile of the quasi–equilibrium state after adding the external potential on the initial FMM model. The other panels show the density profiles of a DM halo at 15 $t_{\rm d}$ (b and f), 30 $t_{\rm d}$ (c and g), 50 $t_{\rm d}$ (d and h) and 110 $t_{\rm d}$ (e and i), respectively. Dashed–line represents the FMM initial condition.

4.3.2 Final States of DM Halos

Figure 4.2 shows the results of simulations for the FMM model (left panels) and the NFW model (right panels). The upper left (right) panel shows the density profile of a DM halo for the unperturbed model with the FMM (NFW) initial condition, respectively. The thick–solid line corresponds to the high–resolution run (UP1 and UP3) and the thin–solid line corresponds to the low–resolution run (UP2 and UP4). In unperturbed runs with only a small number of particles, even though no external potential exists, a cusp–to–core transformation caused by two–body relaxation occurs. Previous studies could not rule out this effect, because they did not use a sufficient number of particles in the central region. However, two of unperturbed runs clearly show that we have a sufficient number of particles to suppress the effect of two–body relaxation and the system remains stable at least several 100 dynamical times.

The middle panels in Figure 4.2 show that the density profile of a DM halo has reached the quasi–equilibrium state after mass loss in ML runs. The thick–solid lines represent the instantaneous mass–loss model (ML1 and ML5) and the thin–solid line corresponds $T_{\rm out} = 50 t_{\rm d}$ (ML4 and ML6). We fit the quasi–equilibrium density profiles for all of ML runs using the least–squares method, and we find the following values for the parameter α. For the FMM model, α is 0.85 for the instantaneous mass–loss (ML1), 1.20 for $T_{\rm out} = t_{\rm d}$ (ML2), 1.44 for $T_{\rm out} = 10\ t_{\rm d}$ (ML3), and 1.46 for $T_{\rm out} = 50\ t_{\rm d}$ (ML4). In Table 4.1, we summarize the resultant α including for the NFW model. It is clear that mass–loss occurs in a short timescale; in other words, intense stellar activities cause the density profiles of DM halos to become shallower. In the slow mass–loss cases (ML3, ML4 and ML6; $T_{\rm out} \gtrsim 10\ {\rm t_d}$), α is approximately conserved. Therefore, to flatten the central cusp needs intense stellar activity; however, even for cases ML1 and ML5 that have such intense stellar activity, α is still larger than the typical observational values of $\alpha \sim 0.2 - 0.3$ (Spekkens et al. 2005).

The lower panels of Figure 4.2 show the amount of energy gained from the external baryon potential. While the baryon potential is added into DM halos, particles in the system acquire kinetic energy to balance the potential energy; conversely, during mass–loss, particles lose kinetic energy. After mass–loss operation has finished, the total energy conserves. The lower panels of Figure 4.2 demonstrate that after mass–loss in the instantaneous mass–loss cases (ML1 and ML5; thick solid lines), DM halos gain more energy than that gained in the slower mass–loss cases (ML2 and ML6; thin solid lines). Therefore, the shorter the timescale of mass–loss, the farther the DM halos expand and the flatter they become.

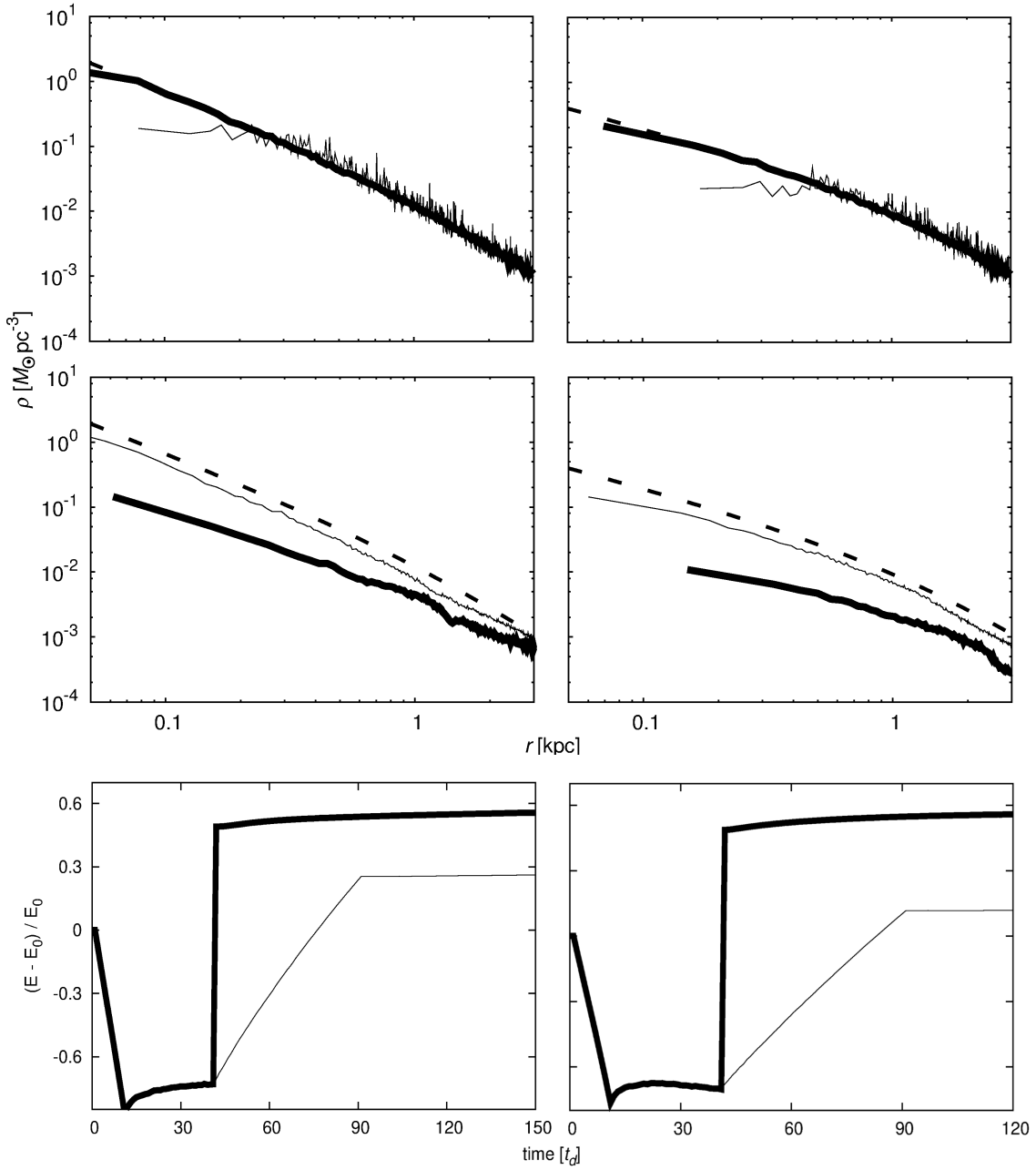

Fig. 4.2: The upper left panel shows the density profile of a DM halo for the unperturbed (UP) model (solid lines) with the FMM initial condition (long–dashed line). The thick–solid line represents $N = 1,048,576$ (UP1) and the thin–solid line represents $N = 16,384$ (UP2). The middle left (right) panel shows the quasi–equilibrium density profile of a DM halo for the FMM (NFW) model with the mass–loss. The thick–solid line represents the instantaneous mass–loss model (ML1 and ML5), and the thin–solid line corresponds $T_{\rm out} = 50 t_{\rm d}$ (ML4 and ML6). The lower left (right) panel shows the variance of the total energy of the system for the FMM model (NFW model). Thick–solid line corresponds the instantaneous mass–loss model, and thin–solid line corresponds $T_{\rm out} = 50\ t_{\rm d}$, where E_0 and E are the total energies of DM halos at the initial and given times, respectively.

4.4 Summary and Discussion

Previous numerical attempts to solve the core–cusp problem of the CDM scenario (e.g., Navarro et al. 1996a; Read & Gilmore 2005) have been limited by two factors: (1) they did not consider the timescale of mass–loss and (2) they could not remove the effects of the two–body relaxation, because they did not use the sufficient number of particles in the center of the DM halos. Our current numerical study overcomes these limitations by considering the timescale of mass loss and including a larger number of particles in the center of DM halos. We find that the timescale of mass–loss is an important factor affecting DM halo dynamics.

Our study determines the dynamical response of DM halos to changes in the gravitational potential induced by stellar activities that remove the baryons from galaxy centers. We especially focus on the timescale of gravitational variance. We find that the central cusp of the DM halo is flatter when mass–loss occurs over a short time than when it occurs over a long time; this result is consistent with the analytical insight of Hills (1980). However, the power–law index of the central cusp α is still larger than typical observational values; in other words, the central cusp remains even for instantaneous mass–loss models. Therefore, mass–loss may not be an effective mechanism to flatten the central cusp, at least in spherical systems. This suggests that DM halos may be stable to mass loss.

Figure 4.3 shows the DF for the FMM initial condition, the quasi–equilibrium state with the external baryon potential, ML1 and ML4. The shape of the DFs after mass loss is similar to the initial condition, suggesting that DM halos return to the initial condition not only in spatial–space but also in phase–space; therefore, DM halos are stable to mass–loss.

In this chapter, we find that a temporal cusp–to–core transformation occurs for instantaneous mass–loss. After a few dozen dynamical times, the cusp regenerates from the center. However, this cusp has a smaller α than the initial conditions, suggesting that the cusp has been somewhat flattened by mass–loss. In addition, we find that not only the density profile but also the energy distribution almost returns to the initial condition for adiabatic mass–loss. The physical mechanism of this cusp regeneration has not been revealed, but it may aid in understanding the formation of the universal density profiles of CDM halos. Only in the linear perturbation regime, the Doremus–Feix–Baumann theorem (Doremus et al. 1971; Binney & Tremaine 2008) states that collisionless N–body systems with DF $f(E)$, $df(E)/dE < 0$ are stable to radial perturbation. However, it is open question in the non–linear regime.

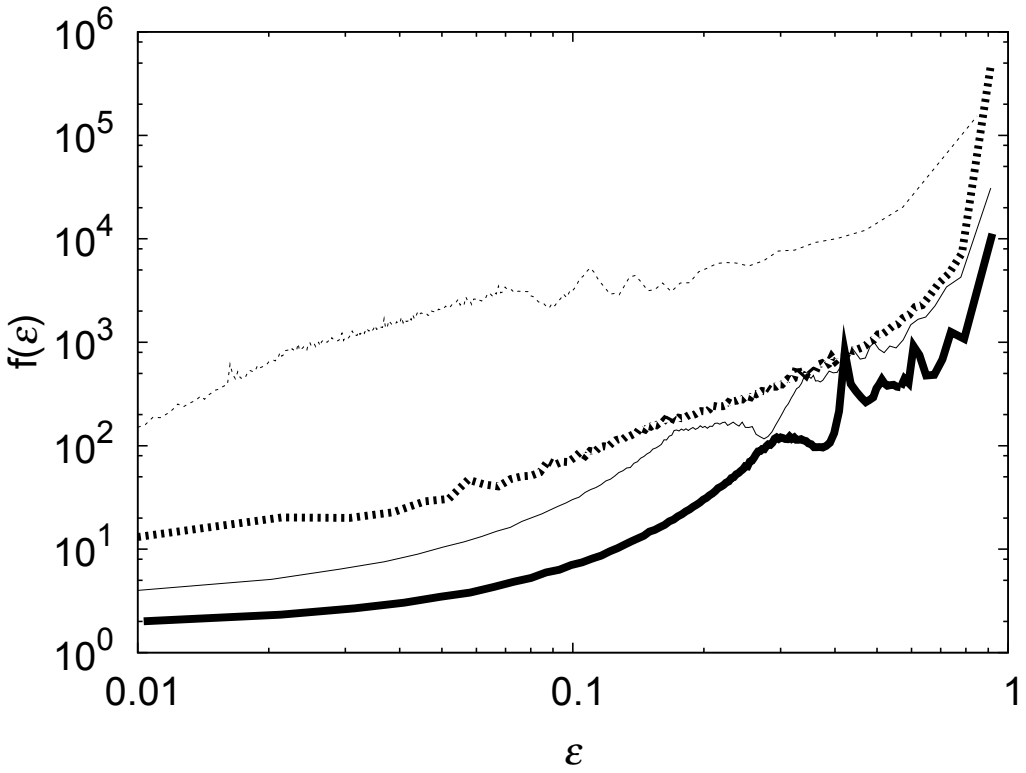

Fig. 4.3: The distribution function of DM halos on the normalized particle energy. This energy is normalized by multiplying by the normalization factor A. Shown are the initial conditions for the FMM model (thick dashed line; $A = -0.70$), the quasi–equilibrium state before the mass–loss operation (thin dashed line; $A = -0.095$), the quasi–equilibrium state for the instantaneous mass–loss model ML1 (thick solid line; $A = -2.0$) and the quasi–adiabatic mass–loss model ML4 (thin solid line; $A = -1.05$).

Chapter 5 Dynamical Effects of Gas Oscillation on Dark Matter Halos

5.1 Introduction

To solve the core–cusp problem, in this chapter, we focuse on the manner in which baryon components gravitationally affect dark matter (DM) halos, because less–massive galaxies, such as dwarf galaxies, are more sensitive to stellar activity such as supernova explosions, as compared to giant galaxies, owing to their shallow gravitational potential well. The hydrodynamic response of dwarf galaxies to stellar activity depends on various factors such as their mass, morphology, and star formation rate (e.g., Dekel & Silk 1986; Yoshii & Arimoto 1987; Mori et al. 1997, 1999, 2002; Mac Low & Ferrara 1999; Silich & Tenorio-Tagle 2001; Bland-Hawthorn et al. 2011).

In less–massive galaxies with smooth gas distribution, supernova feedbacks blow the interstellar gas out from the galaxy centers. This mass–loss reduces the depth of the gravitational potential around the centers of DM halos and may flatten their central cusps. The dynamical effects of this process on DM halos have been studied using collisionless N–body simulations (e.g., Navarro et al. 1996a; Gnedin & Zhao 2002; Read & Gilmore 2005; Ogiya & Mori 2011; Ragone-Figueroa et al. 2012). Ogiya & Mori (2011) discussed the relationship between the dynamical responses of DM halos and the timescale of mass loss (i.e., star formation rate). They found that the density profiles of DM halos correlate with the mass loss timescale, and are flatter when the mass loss occurs over a short time than that over a long time. However, even if the mass loss occurs instantaneously, which results in a maximal effect, the central cusp remains; thus, Ogiya & Mori (2011) concluded that mass loss is not a prime mechanism in flattening of the central cusp. Moreover, they found that the density profile of the DM halo recovers its initial cusp profile when the mass loss timescale is significantly longer than the dynamical time of the system.

Massive galaxies with moderate stellar activity are more robust against supernova feedback; therefore, supernovae can expel only a small fraction of the gas from such galaxies. The gas heated by supernova feedbacks shortly after a star formation burst expands temporarily, and the star formation is then terminated. The expanding gas loses energy by radiative cooling, and then falls back toward the galactic center. Then, the star formation is re–enhanced and subsequently ignites a starburst (Stinson et al. 2007). This repetitive gas motion leads to a repeated change in the gravitational potential. Previous studies have used N–body simulations to study the manner in which such recurring changes in the gravitational potential affect the density structures of DM halos (e.g., Mashchenko et al. 2006). By using hydrodynamic simulations, combined with star formation and supernova feedback, the dynamical effects of such recurring changes have been studied (e.g., Mashchenko et al. 2008; Governato et al. 2010, 2012; Pontzen & Governato 2012; Macciò et al. 2012; Teyssier et al. 2013), and it has been demonstrated that oscillations in the gravitational potential may modify the central cusp into a flat core. Read & Gilmore (2005) reported the importance of recurring changes in the gravitational potential. The oscillation timescale is also an important factor in determining the dynamical effects on DM halos, and dwarf galaxies in the Local Group each have distinctive star formation histories (SFHs; e.g., Mateo 1998; Tolstoy et al. 2009; McQuinn et al. 2010a,b; Weisz et al. 2011). Furthermore, recurring star formation activities duplicate dwarf spheroidal galaxies' properties, which include metal distribution and the velocity–dispersion profile (Ikuta & Arimoto 2002; Marcolini et al. 2006, 2008). However, several additional mechanisms have been proposed to solve the core–cusp problem.

Representative models involve the dynamical friction induced by the motion of gas or stellar clumps (e.g., El-Zant et al. 2001) and bar instability (Weinberg & Katz 2002). Del Popolo (2009) discussed the composite effects of these mechanisms on the density profiles of DM halos.

In this chapter, we investigate the physical mechanism of the cusp–to–core transformation under recurring changes in the gravitational potential of interstellar gas. As previously described, hydrodynamic simulations have demonstrated the repetition of large–scale outflows and inflows. However, the model of Mashchenko et al. (2006) does not reflect such phenomena; they used three particles with motion similar to that of harmonic oscillators to express the repetitive potential change in their standard runs. Pontzen & Governato (2012) constructed an analytical model to understand the mechanism through which the recurring potential flattens the cusps of DM halos. Their model assumes that a harmonic oscillator has the potential to govern the motion of the test particle and that the spring constant changes instantaneously and adiabatically. They determined that most particles in the system gain energy when the potential change occurs instantaneously, and thus the systems expand. However, the nature of the harmonic oscillator potential differs significantly from that of the gravitational potential, such that the acceleration of the harmonic oscillator increases with r, but gravity decays.

To determine the fundamental physical mechanism of the cusp–to–core transformation of DM halos, we adopt a more reasonable formula for the periodic potential by using the Fourier expansion, and analyze the dynamical response of DM halos to recurring potential change with arbitrary periods. Our model can precisely predict the resultant core scale. In addition, we evaluate the energy transfer rate from the oscillating potential to the DM halo, and estimate the number of oscillation cycles required to flatten the cusp and core scale. The resultant core scale determined by the resonance condition is consistent with the critical scale at which the energy transfer rate decays. Then, we clarify the cusp–core transition of DM halos by using collisionless N-body simulations. We also perform N–body + Smoothed Particle Hydrodynamics (SPH) simulations to test our analytical model in more realistic situations.

The rest of this chapter is structured as follows. Our analytic resonance model is described in §5.2. In §5.3, we present our numerical simulation results and interpret them using the resonance model. In §5.4, we discuss the energy transfer rate and some implications for the resonance mechanism. §5.5 describes the physical models of star forming gas and examines the analytical model using N–body + SPH simulations. Finally, we summarize the results in §5.6.

5.2 Analytic Model

We construct a simple analytic model to examine the energy transfer between DM particles and the density waves induced by the recurring expansions and contractions of interstellar gas. In this case, the baryon acts as a forced oscillator, and the resonance theory is applicable to the analysis of the energy transfer from the baryon to the DM halo. §5.2.1 describes the resonance model under an ideal situation, and §5.2.2 shows the resonance condition. The simple relationship between the core radius of a DM halo and the oscillation period is derived in §5.2.3.

5.2.1 Resonance Model

In this subsection, the dynamical evolution of a DM halo is assumed to be described by the linearized fluid equations of the perturbed equilibrium state. Hereafter, we label physical quantities in the initial equilibrium state as "0", the external forces as "ex", and the induced quantities as "ind". We assume an infinite constant density field as the equilibrium state ($\rho_0 = const.$) and select a group of particles with constant velocity ($v_0 = const.$). In addition, the absolute values of the induced quantities are assumed to

be significantly smaller than those of the equilibrium state and the external force. With these assumptions, the linearized equation of motion is given by

$$\frac{\partial v_{\rm ind}(t,r)}{\partial t} + v_0 \frac{\partial v_{\rm ind}(t,r)}{\partial r} = -\frac{\partial \Phi_{\rm ex}(t,r)}{\partial r}, \tag{5.1}$$

where the induced potential $\Phi_{\rm ind}$ is neglected.

By using the Fourier expansion, the periodic external force is expressed as

$$-\frac{\partial \Phi_{\rm ex}(t,r)}{\partial r} = \sum_{n=1}^{\infty} A_n \cos(kr - n\Omega t), \tag{5.2}$$

where A, k, and Ω represent the oscillation strength, which is a positive constant, the wavenumber, and the angular frequency of the external force, respectively. The index n corresponds to the n–th overtone mode. The solution of Equation (5.1) is given by

$$\begin{aligned} v_{\rm ind}(t,r) &= \sum_{n=1}^{\infty} v_{{\rm ind},n}(t,r) \\ &= -\sum_{n=1}^{\infty} \frac{A_n}{n\Omega - kv_0} \\ &\times \{\sin(kr - n\Omega t) - \sin(kr - kv_0 t)\}. \end{aligned} \tag{5.3}$$

The linearized equation of continuity is similarly obtained:

$$\frac{\partial \rho_{\rm ind}(t,r)}{\partial t} + v_0 \frac{\partial \rho_{\rm ind}(t,r)}{\partial r} = -\rho_0 \frac{\partial v_{\rm ind}(t,r)}{\partial r}, \tag{5.4}$$

and the solution is given by

$$\begin{aligned} \rho_{\rm ind}(t,r) &= \sum_{n=1}^{\infty} \rho_{{\rm ind},n}(t,r) \\ &= -\sum_{n=1}^{\infty} \frac{A_n \rho_0 k}{(n\Omega - kv_0)^2} \{\sin(kr - n\Omega t) \\ &- \sin(kr - kv_0 t) + (n\Omega - kv_0) t \cos(kr - kv_0 t)\}. \end{aligned} \tag{5.5}$$

These solutions satisfy the reasonable initial conditions $v_{\rm ind}(0,r) = 0$ and $\rho_{\rm ind}(0,r) = 0$. Although the coefficients of $v_{{\rm ind},n}$ and $\rho_{{\rm ind},n}$ appear to diverge when $n\Omega$ approaches kv_0, we can derive finite values for this limit by using l′Hôpital′s rule:

$$\lim_{n\Omega \to kv_0} v_{{\rm ind},n}(t,r) = A_n t \cos(kr - kv_0 t), \tag{5.6}$$

and

$$\lim_{n\Omega \to kv_0} \rho_{{\rm ind},n}(t,r) = \frac{A_n \rho_0 k}{2} t^2 \sin(kr - kv_0 t). \tag{5.7}$$

Equations (5.6) and (5.7) clearly show that the effects of resonances increase with time.

Next, we examine the energy interchange between the DM collisionless system and the oscillatory external force on the basis of resonance. By averaging the external force per volume $F = -(\rho_0 + \rho_{\rm ind})\nabla\Phi_{\rm ex}$ over a wavelength, the term of ρ_0 vanishes because of the nature of the trigonometric function:

$$\begin{aligned} < F > &= < \sum_{m=1}^{\infty} A_m \cos(kr - m\Omega t) \\ &\times \sum_{n=1}^{\infty} \frac{A_n \rho_0 k}{(n\Omega - kv_0)^2} [\sin(kr - n\Omega t) - \sin(kr - kv_0 t) \\ &+ (n\Omega - kv_0) t \cos(kr - kv_0 t)] > . \end{aligned} \tag{5.8}$$

Here, the interactions between different Fourier modes (i.e., $m \neq n$) are neglected, and only the self–interaction of the modes (i.e., $m = n$) is considered for simplicity. Spatially averaged force is determined through arithmetic calculations:

$$\begin{aligned} < F > &= \sum_{n=1}^{\infty} \frac{A_n^2 \rho_0 k}{2(n\Omega - kv_0)^2} \\ &\times \{\sin[(n\Omega - kv_0)t] - (n\Omega - kv_0)t\cos[(n\Omega - kv_0)t]\} \\ &= \sum_{n=1}^{\infty} \frac{A_n^2 \rho_0}{2} \frac{d}{dv_0}\left\{\frac{\sin[(n\Omega - kv_0)t]}{n\Omega - kv_0}\right\}. \end{aligned} \tag{5.9}$$

Note that we have thus far confined the argument to a particular group of particles. In actuality, the system consists of uncounted groups of particles, and each group has respective velocity in the equilibrium state. The energy transfer rate for the entire system, $\frac{dK}{dt}$, is estimated as

$$\frac{dK}{dt} = \int_{-\infty}^{\infty} d^3 v_0 < F > v_0 f(v_0), \tag{5.10}$$

where $f(v_0)$ is the distribution function (DF) of velocity. Assuming isotropic velocity field and applying Equation (5.9), Equation (5.10) becomes

$$\begin{aligned} \frac{dK}{dt} &= 4\pi \sum_{n=1}^{\infty} \frac{A_n^2 \rho_0}{2} \int_{-\infty}^{\infty} dv_0 f(v_0) v_0^3 \frac{d}{dv_0}\left\{\frac{\sin[(n\Omega - kv_0)t]}{n\Omega - kv_0}\right\} \\ &= 2\pi \sum_{n=1}^{\infty} A_n^2 \rho_0 \left\{ f(v_0) v_0^3 \frac{\sin[(n\Omega - kv_0)t]}{n\Omega - kv_0}\right|_{-\infty}^{\infty} \\ &- \int_{-\infty}^{\infty} dv_0 \frac{d}{dv_0}[f(v_0)v_0^3] \frac{\sin[(n\Omega - kv_0)t]}{n\Omega - kv_0}\Bigg\}. \end{aligned} \tag{5.11}$$

Here, we have used partial integration, and the first term of the second row is 0 because $f(v_0)$ dumps faster than v_0^2 for ordinary self–gravity systems (e.g., Maxwell–Boltzmann distribution). In the limit of $t \gg T$, where $T \equiv 2\pi/\Omega$ is the oscillation period, it is nicely approximated by

$$\frac{\sin[(n\Omega - kv_0)t]}{n\Omega - kv_0} \approx \frac{\pi}{k}\delta(v_0 - n\Omega/k). \tag{5.12}$$

By substituting Equation (5.12) into Equation (5.11), the energy transfer rate per volume is finally given by

$$\frac{dK}{dt} = -2\pi^2 \sum_{n=1}^{\infty} \frac{A_n^2 \rho_0}{k} \left(\frac{n\Omega}{k}\right)^3 \left.\frac{df(v_0)}{dv_0}\right|_{v_0 = n\Omega/k}. \tag{5.13}$$

In actual self–gravitational systems, the phase space density of lower velocity particles is usually dominant, as compared with that of higher velocity particles. Because the velocity of resonant particles, $v_0 = n\Omega/k$, is positive, $df(v_0)/dv_0|_{v_0 = n\Omega/k}$ is negative. Thus, dK/dt will be positive. That is, the system will gain substantial net energy from the external force.

On the basis of these results, we conclude that the particles satisfying the resonance condition

$$kv_0 \approx n\Omega \tag{5.14}$$

effectively gain kinetic energy, and that the system will expand to settle the new equilibrium state, resulting in a decrease in density.

5.2.2 Resonance Condition

We apply the resonance condition to spherically symmetric systems. Although the prescription in this subsection may appear to be somewhat ad hoc, it is designed to provide an intuitive understanding of the

physical mechanism responsible for the cusp–to–core transformation and gives a useful formula for predicting the resultant core scale created by the oscillatory external force.

First, the wave number as a function of distance r from the center of the system is redefined by

$$k(r) \equiv \frac{2\pi}{r}. \tag{5.15}$$

Second, we substitute v_0 in Equation (5.14) by velocity dispersion $\sigma(r)$, which can be regarded as the typical velocity of particles at r, and estimate the value by

$$\sigma(r) = \sqrt{\frac{GM(r)}{r}}, \tag{5.16}$$

where $M(r)$ is enclosed mass within r and G is the gravitational constant. Here, we attempt to expand the notion of the critical resonance condition given by Equation (5.14) as

$$k(r)\sigma(r) \approx n\Omega. \tag{5.17}$$

Then, we define the local dynamical time of the system as

$$t_{\rm d}(r) = \sqrt{\frac{3\pi}{32G\bar{\rho}(r)}}, \tag{5.18}$$

where

$$\bar{\rho}(r) = \frac{M(r)}{(4\pi/3)r^3}, \tag{5.19}$$

is the averaged density interior to radius r. With these applications, the resonant condition becomes

$$t_{\rm d}(r_n) = \frac{\pi}{2\sqrt{2}}\frac{T}{n} \sim \frac{T}{n}, \tag{5.20}$$

where T corresponds the oscillation period for the fundamental–tone ($n = 1$), and r_n is the radius around which the resonance condition of the n–th overtone mode is satisfied. Considering the Maxwell–Boltzmann DF for particle velocity, Equation (5.13) indicates $dK/dt \propto n^4 \exp(-n^2)$. The contribution of the fundamental–tone to the system will be greater than that of the overtone modes. Therefore, we focus on the resonance of the fundamental–tone.

The resonance of the overtone modes occurs in the dense region of a DM halo (i.e., around the center), while that of the fundamental–tone appears in the less–dense region (i.e., outskirts), whose local dynamical time is longer than that of the dense region. Thus, the effects of resonances will appear at more inner locations than r_1, where the resonance condition for the fundamental tone,

$$t_{\rm d}(r_1) \sim T, \tag{5.21}$$

is satisfied. By using the inversion procedure to solve this equation, the resonance radius is obtained by

$$r_1 = t_d^{-1}(T). \tag{5.22}$$

In the following subsection, we apply this prescription of the resonant cusp–to–core transformation to the models of CDM halos predicted by cosmological N–body simulations, and estimate the core scale.

5.2.3 Core Scale

The mass–density profile of a DM halo obtained from cosmological N–body simulations based on the CDM scenario can be fitted by the following formula:

$$\rho_{\rm DM}(x) = \frac{\rho_0}{x^\alpha(x+1)^{3-\alpha}}, \tag{5.23}$$

where $x \equiv r/R_{\rm DM}$, r is the distance from the center of a DM halo; α is the power–law index of the central cusp; and ρ_0 and $R_{\rm DM}$ are the scale density and scale length of a DM halo, respectively. This formula indicates that the density distribution of a DM halo changes from $\rho \propto r^{-\alpha}$ in the center ($r < R_{\rm DM}$) to $\rho \propto r^{-3}$ at the outskirts ($r > R_{\rm DM}$). Here, $\alpha = 1.0$ corresponds to the Navarro–Frenk–White (NFW) model (Navarro et al. 1996b, 1997), and $\alpha = 1.5$ corresponds to the Fukushige–Makino–Moore (FMM) model (Fukushige & Makino 1997; Moore et al. 1999b).

The mass profile derived by the volume integration of Equation (5.23) is given by

$$M(\alpha; x) = \frac{4\pi\rho_0 R_{\rm DM}^3}{3-\alpha} x^{3-\alpha}\, {}_2F_1[3-\alpha, 3-\alpha, 4-\alpha; -x], \tag{5.24}$$

where ${}_2F_1[3-\alpha, 3-\alpha, 4-\alpha; -x]$ is Gauss's hypergeometric function, which is hereafter denoted as ${}_2F_1[\alpha; -x]$. From Equation (5.24),

$$\rho_0 = \frac{3-\alpha}{4\pi R_{\rm DM}^3} \frac{1}{c^{3-\alpha}\, {}_2F_1[\alpha; -c]} M_{\rm vir}. \tag{5.25}$$

The virial mass of a DM halo is defined by

$$M_{\rm vir} = \frac{4\pi}{3} \rho_{\rm cri} (1+z)^3 \Delta R_{\rm vir}^3, \tag{5.26}$$

where $\rho_{\rm cri}$ is the critical density of the universe, z is the redshift, $\Delta (= 200)$ is a parameter of density enhancement, $c = R_{\rm vir}/R_{\rm DM}$ is a concentration parameter, and $R_{\rm vir}$ is the virial radius.

By using Equations (5.24) and (5.25), the averaged density of a DM halo interior to radius x is given by

$$\bar{\rho}(x) = \frac{3M_{\rm vir}}{4\pi R_{\rm DM}^3} \frac{x^{-\alpha}}{c^{3-\alpha}} \frac{{}_2F_1[\alpha; -x]}{{}_2F_1[\alpha; -c]}, \tag{5.27}$$

and by applying the resonance condition given in Equation (5.21), we finally arrive at the core scale $r_{\rm core} = x_{\rm core}\, R_{\rm DM}$.

We now discuss the utmost limit, $x_{\rm core} \ll 1$. In this case, the approximation ${}_2F_1[\alpha; -x] \sim 1$ holds. Thus, the core scale is expressed as

$$r_{\rm core} = R_{\rm DM} \left[\frac{8G}{\pi^2} \frac{M_{\rm vir} T^2}{R_{\rm DM}^3 c^{3-\alpha}\, {}_2F_1[\alpha; -c]} \right]^{1/\alpha}, \tag{5.28}$$

$$= R_{\rm DM} \left[\frac{32G}{3\pi} \Delta\rho_{\rm cri} (1+z)^3 \frac{c^\alpha}{{}_2F_1[\alpha; -c]} T^2 \right]^{1/\alpha}. \tag{5.29}$$

By using Equation (5.26), more convenient formulae are given by

$$r_{\rm core} = 0.74 \;\; {}_2F_1[1; -c]^{-1} (1+z)^2 \times \left(\frac{M_{\rm vir}}{10^9 M_\odot}\right)^{1/3} \left(\frac{T}{10^7 {\rm yr}}\right)^2 {\rm pc}, \tag{5.30}$$

for the NFW model, and

$$r_{\rm core} = 23 \;\; {}_2F_1[1.5; -c]^{-2/3} (1+z) \times \left(\frac{M_{\rm vir}}{10^9 M_\odot}\right)^{1/3} \left(\frac{T}{10^7 {\rm yr}}\right)^{4/3} {\rm pc}, \tag{5.31}$$

for the FMM model. Here, we show some values of ${}_2F_1[\alpha; -c]$ in Table 5.1 for $\alpha = 1.0, 1.5$ and some ordinary c parameters obtained from cosmological N–body simulations (e.g., Macciò et al. 2008). Moreover, assuming $c = 10$ and $z = 0$, we reach the core scale represented by the following simpler formulae:

$$r_{\rm core} = 25 \left(\frac{M_{\rm vir}}{10^9 M_\odot}\right)^{1/3} \left(\frac{T}{10^7 {\rm yr}}\right)^2 {\rm pc}, \tag{5.32}$$

for the NFW model, and

$$r_{\rm core} = 120\ \left(\frac{M_{\rm vir}}{10^9 M_\odot}\right)^{1/3}\left(\frac{T}{10^7 {\rm yr}}\right)^{4/3}{\rm pc}, \tag{5.33}$$

for the FMM model.

In the following section, we evaluate the quality and integrity of the analytical prediction by performing numerical experiments of N–body simulations.

Table. 5.1: Numerical values of ${}_2F_1[\alpha; -c]$ for conventional models of DM halos

α (Model)	$c = 5$	$c = 10$	$c = 15$	$c = 20$
1.0 (NFW)	0.07667	0.02978	0.01631	0.01046
1.5 (FMM)	0.16948	0.08681	0.05656	0.04117

Note: α is the power–law index of the central cusp of the DM halo and c is the concentration parameter.

5.3 N–body Simulations

5.3.1 Numerical Models

We develop a parallelized tree code for graphics processing unit (GPU) clusters that adopts the standard algorithm proposed by Barnes & Hut (1986) and employs the second–order Runge–Kutta scheme as the time integration method. In light of Nakasato (2012), we design CPU cores to compute tree construction and GPU cards to compute tree–traversal (Ogiya et al. 2013). To generate N–body systems with a cusp described in Equation (5.23), in the equilibrium state, we use the fitting formulation of the DF proposed by Widrow (2000). In this case, the DF depends only on energy, and the velocity dispersion of the system is isotropic.

We simulate the dynamical response of a DM halo with virial mass $M_{\rm vir} = 10^9 M_\odot$, virial radius $R_{\rm vir} = 10$, and scale length $R_{\rm DM} = 2$ kpc assuming the formation redshift $z = 1$. Here, we define $\tau = 10$ Myr for the NFW model and 4 Myr for the FMM model as the typical timescales of dynamical response near the innermost regions of DM halos. Throughout this chaper, the tolerance parameter of the Barnes–Hut tree algorithm (Barnes & Hut 1986) is $\theta = 0.6$ and the softening parameter is $\epsilon = 0.004$ kpc. The total number of particles is $N = 16,777,216$ for ordinary runs. In the high-resolution run for the check of numerical convergence, we use $N = 134,217,728$.

The baryon potential near the centers of DM halos is represented by the Hernquist–type potential (Hernquist 1990), which is given by

$$\Phi_{\rm b}(r,t) = -\frac{GM_{\rm b}}{r + R_{\rm b}(t)}, \tag{5.34}$$

where $M_{\rm b}$ and $R_{\rm b}(t)$ are the total baryon mass and the scale length of the external potential, respectively. We change the scale length of the baryon potential to $R_{\rm b}(t) = 0.5[R_{\rm b,max} - R_{\rm b,min}][1+\cos(\Omega t - \phi_0)] + R_{\rm b,min}$, T is the timescale of oscillation of the external potential, $R_{\rm b,max}$ and $R_{\rm b,min}$ are the maximum and minimum scale lengths, and ϕ_0 is the initial phase of oscillation, respectively. Note that even if no external potential exists, the cusp–to–core transformation may occur by two–body relaxation for a few particles to resolve the central cusp. Figure 5.1 clearly shows that in our model, the system remains stable for the entire time and that the effect of two–body relaxation is not observed for at least several 100τ.

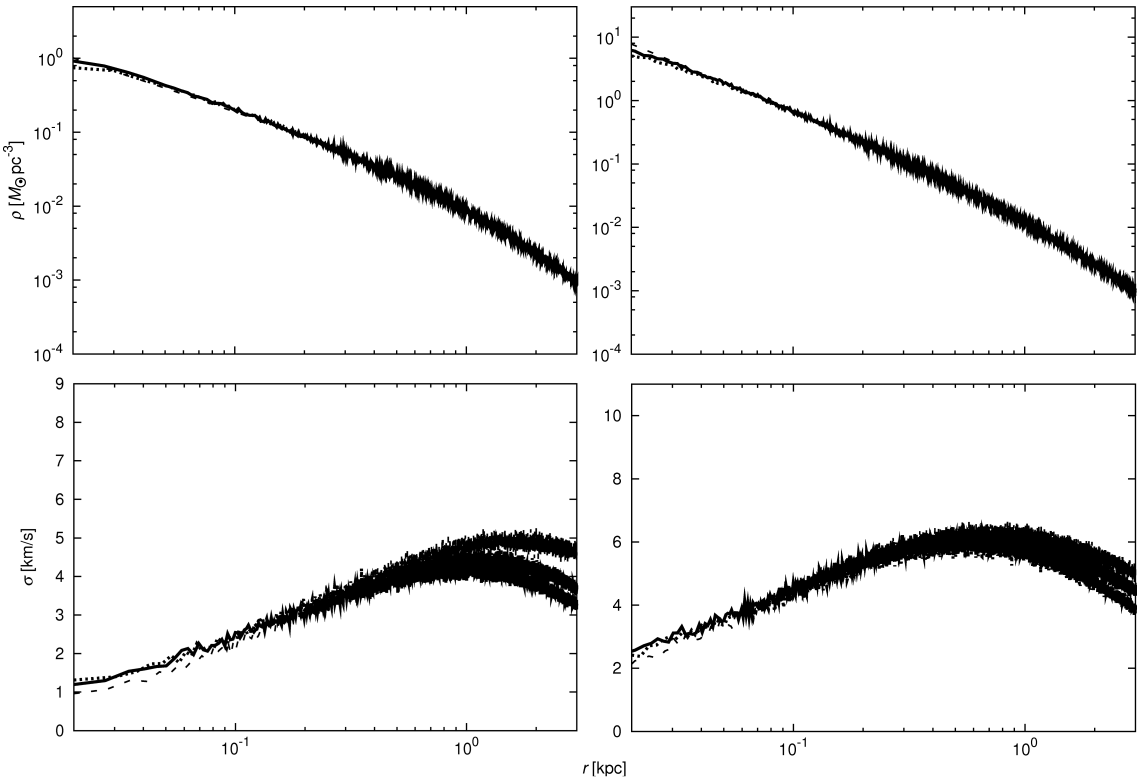

Fig. 5.1: Density and velocity dispersion profiles of nonperturbed (equilibrium) NFW (left) and FMM (right) halos. Dashed lines in the upper panels (density profile) are the analytical formulation given by Equation (5.23). In the lower panels (velocity dispersion), these lines represent the DM halos created by following the formula described in the text.

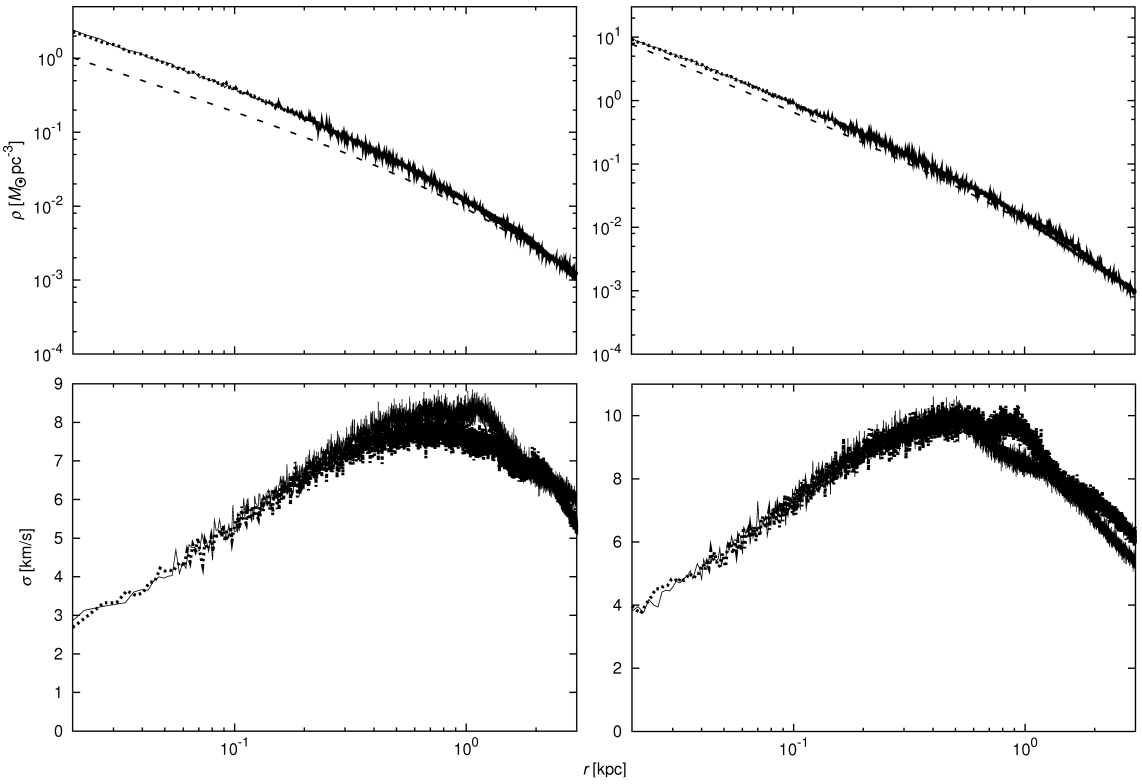

Fig. 5.2: State of the dynamically relaxed NFW (left) and FMM halo (right) with the static external potential for $R_{\rm b} = R_{\rm b,0}$. Top and bottom panels show the density and velocity dispersion profiles of DM halos, respectively. The thin solid line (thick dotted line) represents $t = 15\tau (t = 30\tau)$ after adding the static external potential for a constant scale length $R_{\rm b}(t) = R_{\rm b,0} = 1$ kpc defined by Equation (4.2).

To construct a stable initial condition, we dynamically relax the equilibrium N–body system in the abovementioned external baryon potential with the fixed scale length $R_{\rm b} = R_{\rm b,0}$ for $\sim 30\tau$ where $R_{\rm b,0}$ is the initial scale length of the baryon potential. We define the initial phase of oscillation as $\phi_0 = \arccos\left[2(R_{\rm b,0} - R_{\rm b,min})/(R_{\rm b,max} - R_{\rm b,min}) - 1\right]$.

The left (right) panel of Figure 5.2 indicates the states of dynamically relaxed NFW (FMM) halos. The top and bottom panels represent the density and velocity dispersion profiles of the DM halos, respectively. The thin solid line corresponds to the snapshot of the state exposed to the static external potential for 15τ. After 30τ, the system reaches the quasistable state and remains virtually unchanged (dotted line). Because of the static external potential, the DM halos show slight contraction (top panels). A comparison between the bottom panels of Figs. 5.1 and 5.2 reveals that the velocity dispersion becomes larger than the equilibrium state because of the deeper potential. Table 5.2 gives the summary of our simulation runs.

Table. 5.2: Summary of simulation runs

ID	T [τ]	$M_{\rm b}$ [$\times 10^8 M_\odot$]	$R_{\rm b,0}$ [kpc]	$R_{\rm b,max}$ [kpc]	$R_{\rm b,min}$ [kpc]
NFW–NP	–	–	–	–	–
NFW–1	1	1.7	1.0	2.0	0.04
NFW–2, 2HR	3	1.7	1.0	2.0	0.04
NFW–3	10	1.7	1.0	2.0	0.04
NFW–4	1 & 10	1.7	1.0	2.0	0.04
NFW–5	1	0.85	1.0	2.0	0.04
NFW–6	1	1.7	1.0	2.0	0.2
NFW–7	1	1.7	0.1	0.2	0.04
NFW–8	1	1.7	0.1	2.0	0.04
FMM–NP	–	–	–	–	–
FMM–1	1	1.7	1.0	2.0	0.04
FMM–2	3	1.7	1.0	2.0	0.04
FMM–3	10	1.7	1.0	2.0	0.04

Note: NFW and FMM indicate the initial DM halo model. NP is the nonperturbed run for testing the stability of the N–body systems. T and $M_{\rm b}$ are the oscillation period and total mass of the baryon potential, respectively. $R_{\rm b,0}$, $R_{\rm b,max}$, and $R_{\rm b,min}$ are initial, maximum, and minimum scale length of the external baryon potential, respectively. We adopt the mass ratio of the baryon component to the DM halo cosmic value obtained from *Wilkinson Microwave Anisotropy Probe* observations (Spergel et al. 2007; Komatsu et al. 2009, 2011).

5.3.2 Results

In this subsection, we present the results of our N–body simulations and compare them with the theoretical prediction of the simple analytic model given in §5.2.

Figure 5.3 demonstrates how the dynamical responses of DM halos depend on the oscillation frequency of the external baryon potential. In each panel, solid, dotted, dotted-dashed, and dashed lines correspond to $T = \tau, 3\tau$, and 10τ and the initial condition, respectively. The thin solid line represents the high–resolution run of $T = 3\tau$. It is clear that the results converge very well. The upper–left (upper–right) panel shows the resultant density profiles of DM halos for the initial NFW (FMM) model after 10 oscillation cycles. Models of $T = \tau$ and 3τ clearly show the cusp–to–core transformation, and the resultant core scale depends on the oscillation frequency of the external baryon potential. The vertical dashed lines in both panels represent the core scales predicted by Equations (5.30) and (5.31), whereas the left and right lines represent the cases for $T = \tau$ and $T = 3\tau$, respectively. The analytical predictions based on Equation (5.22) are indicated by vertical solid lines.

Figure 5.3 shows that our analytic model perfectly matches the core scale derived by these numerical experiments for runs of $T = \tau$ and 3τ. In the runs of $T = 10\tau$, the central cusps remain, while bump structures appear at the outskirts. Although it is beyond the appropriate range of the approximation $x_{\rm core} \ll 1$, Equation (5.31) gives a reasonable prediction for the bump structure of FMM halo. As discussed in §5.2, the overtone modes affect the center region, and the impacts of the overtones of high Fourier indexes are weaker than those of the fundamental tone and overtones of low indexes. Therefore, the number of oscillation cycles is not sufficient to flatten the cusp for the runs.

We computed the Fourier transformation of the radial velocity to verify the emergence of the energy transfer due to the resonance between the particles and the density waves. Because DM halos are perturbed radially in our model, the induced density waves will propagate in that direction. The Fourier transform technique is useful for decomposing wave components. By using snapshot data of a given time, t, we compute the radial velocity profile, $v_{\rm r}(r,t)$, which is the averaged radial velocity of particles in each radial bin. Then, $v_{\rm r}$ is transformed into the temporal Fourier components (i.e., spectrum), $\hat{v}_{\rm r}(r,\omega)$, by the conventional procedure,

$$\hat{v}_{\rm r}(r,\omega) = \int v_{\rm r}(r,t) e^{-i\omega t} dt, \tag{5.35}$$

with the sampling frequency of 0.1τ. The lower panels in Figure 5.3 show that $\hat{v}_{\rm r}$ of the angular frequency, ω, equals the oscillation frequency of the external potential $\Omega \equiv 2\pi/T$. The positions of the peaks clearly match the core or bump scale in the density profile and depend on T. The figure demonstrates the spectrum of the fundamental mode for each run. These results clearly show that, as expected, the core scale agrees with the peak's position predicted by Equation (5.22). As discussed in the previous section, the resonance of the slow oscillation appears at the less–dense region of the DM halo (i.e., outskirts), whereas that of the rapid oscillation appears at the central denser region. This result indicates that when DM halos are in resonance with the external potential, particles are accelerated effectively so that the core is created near the peak.

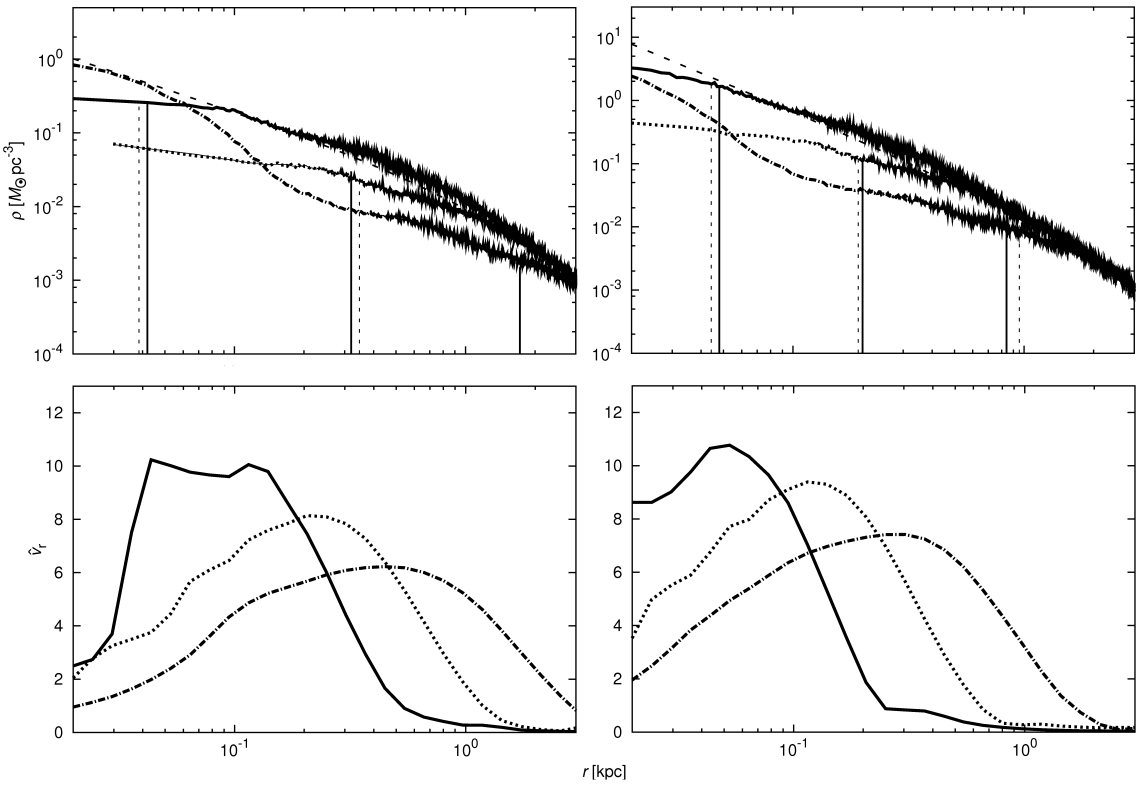

Fig. 5.3: Density profile (top panels) and spectrum of radial velocity (bottom panels) of DM halos after 10 oscillations of the external potential. Left panels show results of the NFW model (NFW–1, NFW–2, and NFW–3), and right panels show those of the FMM model (FMM–1, FMM–2, and FMM–3). Solid, dotted, dotted–dashed, and dashed lines represent $T = \tau, 3\tau$, and 10τ and the initial condition, respectively. The thin solid line in the upper left panel represents the high–resolution run of $T = 3\tau$ (NFW–2HR). Each vertical and solid line indicates the core scale predicted by Equation (5.22). The dashed ones are derived using Equations (5.30) or (5.31).

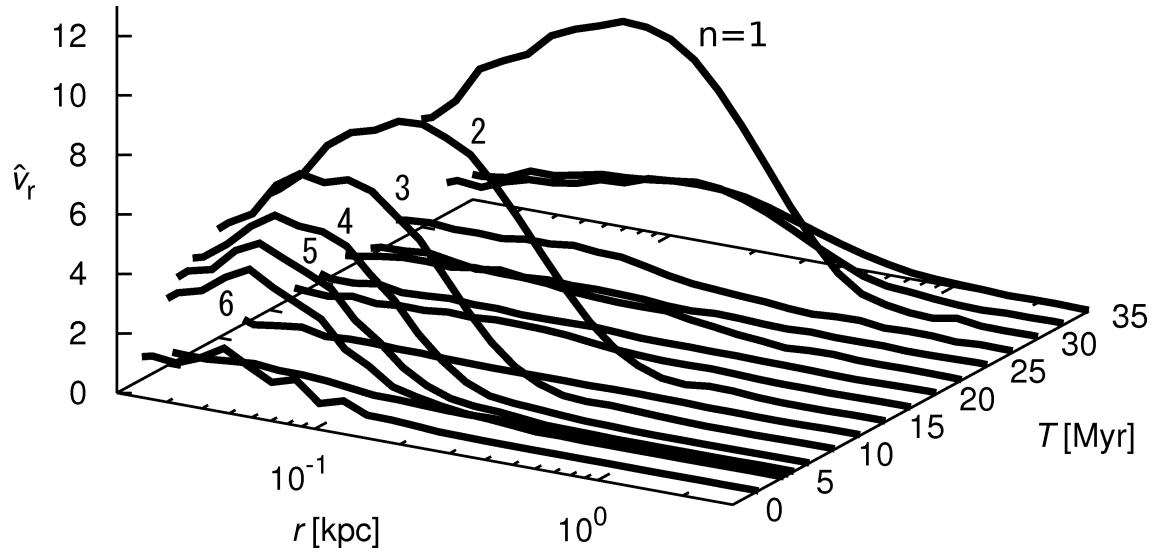

Fig. 5.4: Spectrum of radial velocity $\hat{v}_r$ of the DM halo (NFW–2) including the case of $\omega \neq \Omega$. Each line represents $\hat{v}_r$ for different frequencies, and ω is shown as the period, T (viz. $\omega = 2\pi/T$). The indices of the overtone modes, n, are denoted by the corresponding lines.

Figure 5.4 shows $\hat{v}_r$ including the case of $\omega \neq \Omega$. Although only the result of NFW–2 is shown in this figure, a similar phenomenon appears for other models. In the bottom panels of Figure 5.3, we show only the fundamental mode for each T. Figure 5.4 explains the resonances of the overtone modes expected from Equation (5.14); these appear with peaks, and their overtone indexes n are denoted. These peaks never appear outside the modes with integral indexes. The figure also shows a tendency that the signatures of the resonances of higher overtones are fainter than those of lower overtones or the fundamental tone, which implies that the influences of the resonances of the overtones weaken with an increase in n, as expected in §5.2. In the runs of $T = 10\tau$, the 10th overtone which corresponds to the mode of 10Myr $= \tau$ may contribute to particle acceleration; however, its impact is not sufficient to flatten the central cusp. On the contrary, in the runs of $T = 3\tau$, the effects of the third overtone which corresponds to the mode of 10Myr $= \tau$ are significant to the systems, and the core structure is created at the center. Because its fundamental tone which corresponds to the mode of $T = 30\text{Myr} = 3\tau$ is effective near $r \sim 340$ and 190 pc for NFW and FMM models, respectively, the core scale becomes larger than that of $T = \tau$ models (NFW–1 and FMM–1).

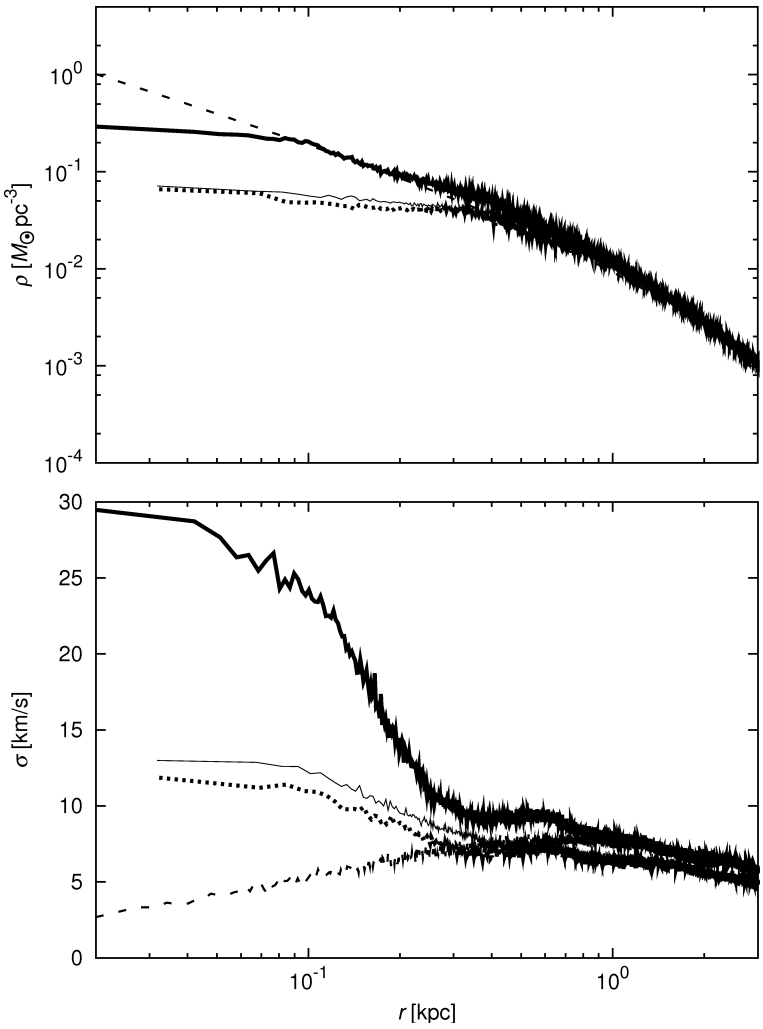

Fig. 5.5: Density and velocity dispersion profiles of the DM halo (NFW–1) after oscillation has stopped. The thick solid line represents the state at the end of 10 oscillation cycles. We then add the static external potential for $R_{\rm b} = R_{\rm b,0} = 1$ kpc to the system. The dotted and thin solid lines express the snapshots after 10τ and 50τ. Dashed line in the top panel is the NFW profile. That in the bottom panel represents the dynamically relaxed NFW halo with the static external potential for $R_{\rm b} = 1$ kpc.

We next determine whether the central cusp recovers when the gas oscillation stops. To review the dynamical evolution of the DM halo in such cases, we extend the simulation of NFW–1 from the snapshot after 10 oscillation cycles. In this extension, we add the static external potential for $R_{\rm b} = R_{\rm b,0} = 1$ kpc, which corresponds to the gravitational potential of the quiescent baryon component. Figure 5.5 clearly shows that after the gas oscillation has stopped, the central cusp does not recover, despite the attracting force of the static external potential. Because of the heating by the oscillatory potential, the system expands and the core scale increases after the oscillation process ends. The DM halo then reaches the new quasiequilibrium state.

The cusp remains when the oscillation period is sufficiently longer than the local dynamical time near the center (dotted-dashed lines in Figure 5.3). Although we have thus far assumed mono–periods for simplicity, multiperiodic oscillations occur in real galaxies. Because the resonance scale is determined by the period, such oscillations are expected to show effects in multiscales, and the remaining cusp may be erased. To test this hypothesis, we conduct an N–body simulation (NFW–4). In this run, we modify the external potential as

$$\Phi_{\rm b}(r,t) = -\frac{GM_{\rm b}}{2}\left[\frac{1}{r+R_{\rm b,1}(t)} + \frac{1}{r+R_{\rm b,2}(t)}\right]. \tag{5.36}$$

Here, $R_{\rm b,1}(t)$ and $R_{\rm b,2}(t)$ are the scale length of the external potential and have periods $T_1 = \tau = 10$Myr and $T_2 = 10\tau = 100$Myr, respectively.

In Figure 5.6, we compare the results of this simulation with those of NFW–3. The central cusp is flattened in the run of NFW–4 (solid line). Interestingly, the core size is almost the same as the bump scale of NFW–3. As discussed in §5.2, the core size is determined by the resonance of the slowest mode. In the runs of NFW–3 and NFW–4, the slowest modes are the same (T = 100 Myr). Conversely, the density structures at the innermost regions differ significantly because of the strength of the rapid mode resonation near the center, which may have flattened the cusp. As described in §5.2, although the external potential in NFW–3 contains the modes' affect at the center, they are higher overtone modes and their strengths decrease with the index of Fourier components, n. In NFW–4, however, the mode of $T = 10$ Myr is included as one of the fundamental tones, and its strength is sufficiently large to significantly affect the central cusp. Consequently, the resonance of the rapid mode, $T_1 = \tau$, destroys the cusp, and that of the slow mode, $T_2 = 10\tau$, expands the core size in this run.

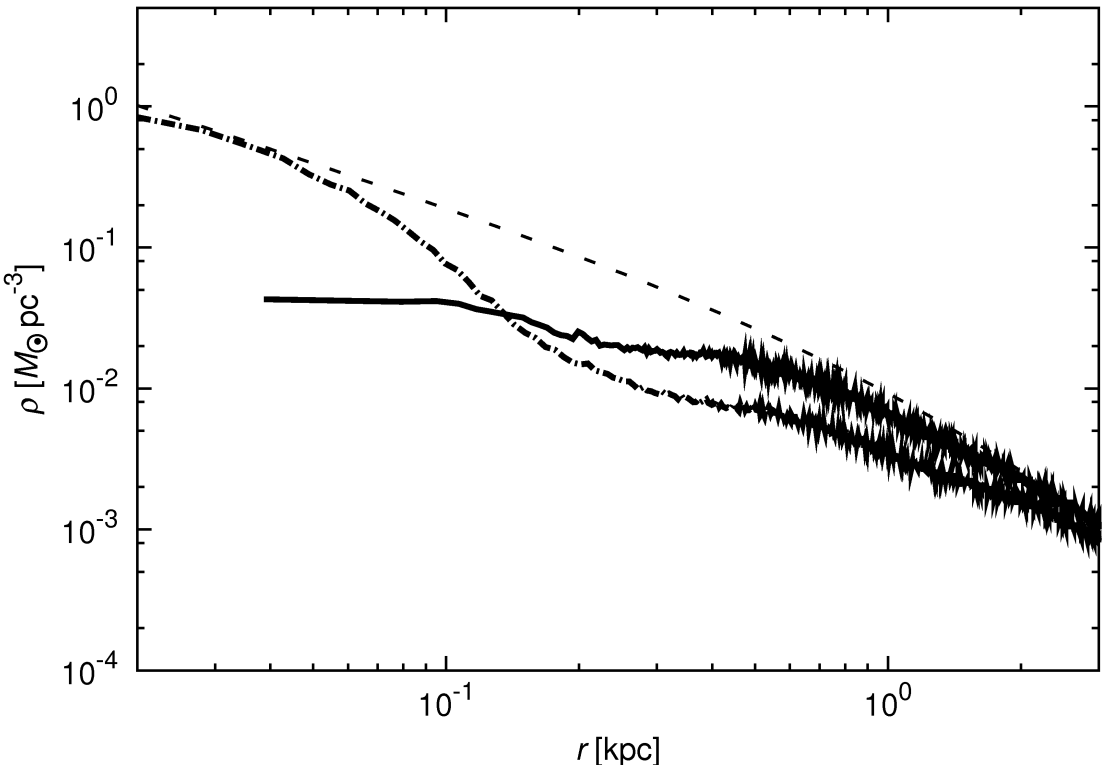

Fig. 5.6: Density profile of the DM halos after exposure to the external potential for 1 Gyr. Solid and dotted–dashed lines represent the results of NFW–4 and NFW–3, respectively. The dashed line represents the NFW profile.

5.4 Discussion

5.4.1 Energy Transfer Rate and Number of Cycles

We have demonstrated that the density profile of DM halos is significantly affected by the resonance between the DM particles and the density waves of the interstellar gas. Although only the oscillation period is the focus of the previous section, the mass of gas component ($M_{\rm b}$) and width of gas oscillation ($R_{\rm b,min}, R_{\rm b,max}$) are also important factors in the real galaxies because they determine the amplitude of potential change and the number of oscillation cycles required to flatten the cusp. Here, we discuss such dependence by using the argument of energy transfer rate from the oscillatory change in galactic potential to DM halos.

We modify the energy transfer rate given by Equation (5.13) as

$$\frac{dK(r)}{dt} = -2\pi^2 \sum_{n=1}^{\infty} \frac{A_n(r)^2 \bar{\rho}(r)}{k(r)} v_0^3(r) \frac{df(v_0)}{dv_0}(r)\Big|_{v_0(r)=n\Omega/k(r)}, \tag{5.37}$$

where $v_0(r) = n\Omega/k(r)$ is the velocity of particles resonating with the n–th overtone mode. The DF of the particle velocity $f(v)$ is adopted by the fitting function proposed by Widrow (2000), and $dK(r)/dt$ is the kinetic energy density injected from the external force to the system per unit time. We compare these values with the binding energy density of the equilibrium NFW halo, $W(r)$, to estimate the number of oscillation cycles required for excess injected kinetic energy over the binding energy, $N_{\rm osc}$.

Figure 5.7 shows the core scale predicted by this model. In these runs, we set the number of oscillation cycles at 10. According to this estimation, the input kinetic energy will be exceeded in the region of curves below the horizontal solid line, and the core structure will be created there. The results of the simulation runs for $T = \tau$ and 3τ (NFW–1,2) accommodate the prediction (upper–left panel in Figure 5.3). The estimation for the core scale determined using the energy transfer rate is consistent with the prediction based on the resonant condition derived in §5.2. However, our model tends to predict a slightly larger core scale than that shown in the simulation results, which may have been caused by the overestimation of the rate of kinetic energy transfer from the baryon potential to the DM halo because of the approximation from Equation (5.12). Nonlinear or multidimensional effects not considered in the model may also have led to the overestimation. Our model fails the prediction for the run of $T = 10\tau$, which is unfortunate because the interactions among different Fourier modes that we neglect are essential in this case. Particles moving faster than density waves push them and lose kinetic energy. Evaluation of such power to accurately estimate the net energy transfer rate requires a significantly more complex analysis.

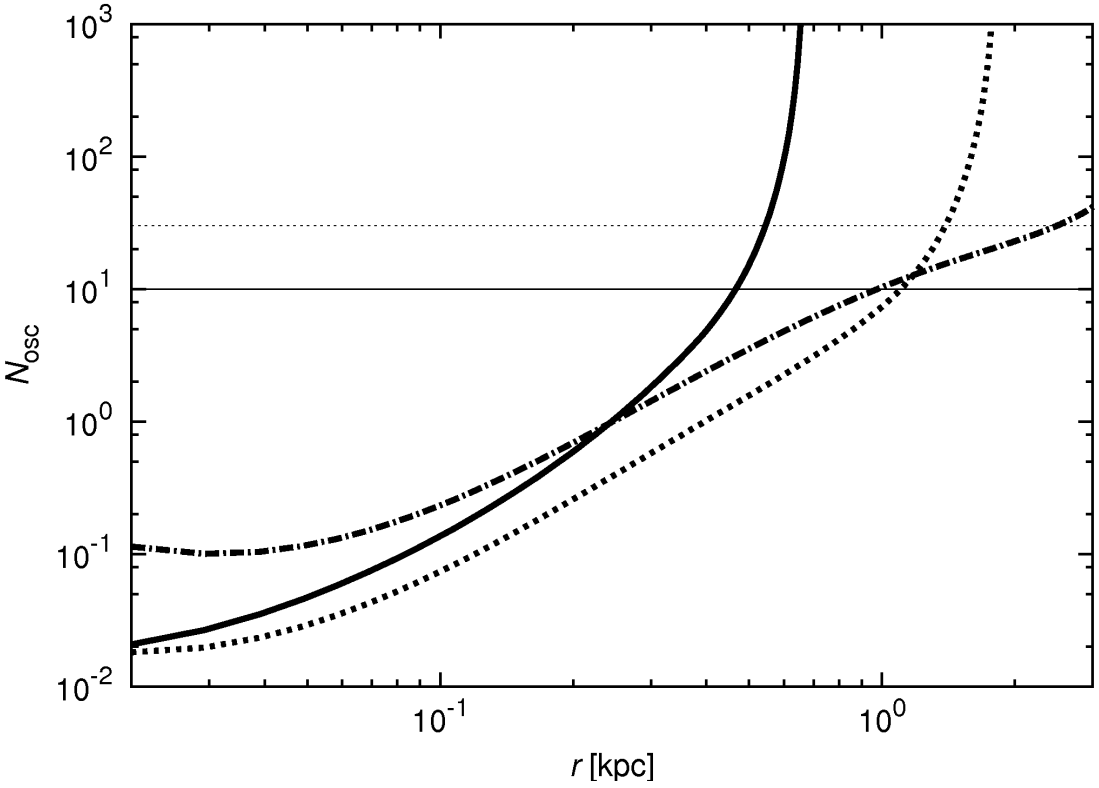

Fig. 5.7: Number of oscillation cycles for the excess of injected kinetic energy over the binding energy, $N_{\rm osc}$ as a function of r. Thick solid, dotted, and dotted–dashed lines represent $T = \tau, 3\tau$, and $10\,\tau$, respectively. Horizontal solid (dotted) lines represent 10 (30) cycles.

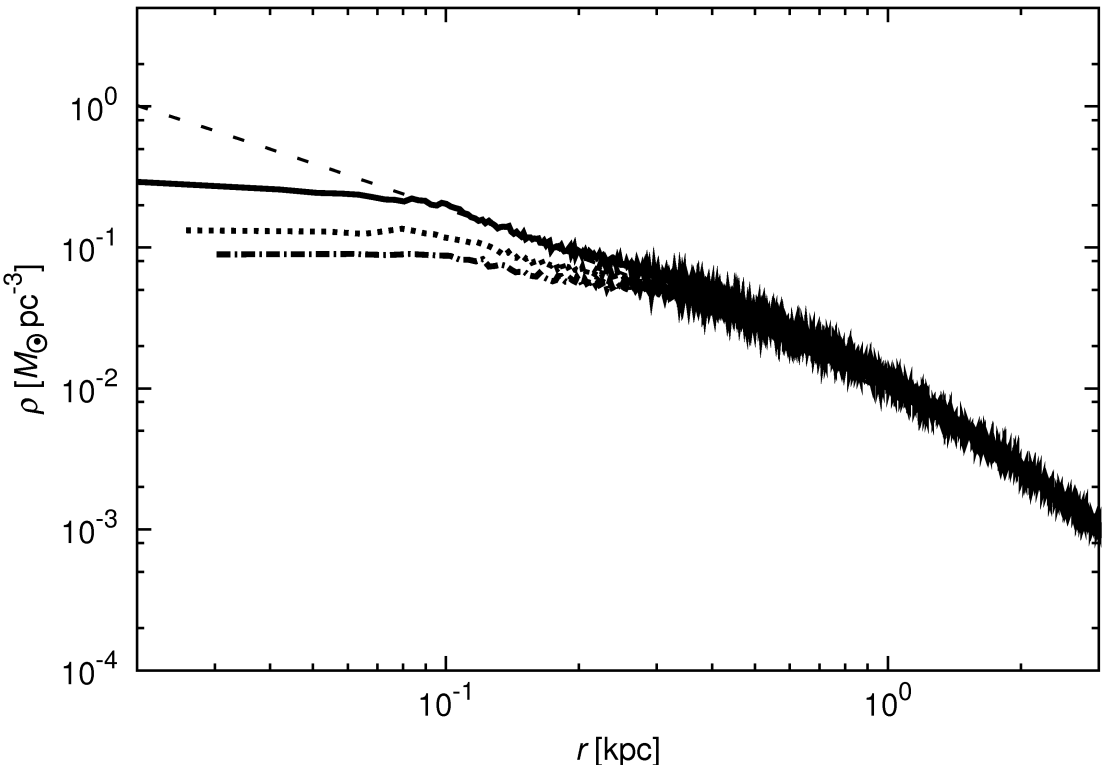

Fig. 5.8: Evolutional process of the density profile of the DM halo (NFW–1) after 10 (solid line), 20 (dotted line), and 30 (dotted–dashed) cycles. The dashed line represents the NFW profile.

This argument also implies that even if we increase the number of cycles, the structure will be scarcely affected because the number of cycles for the excess amount of injected kinetic energy over binding energy, $N_{\rm osc}$, diverges; that is, the energy transfer rate, dK/dt, approaches 0. We then examine the factor determining such a divergent point of $N_{\rm osc}$, or the terminatory core scale. In the initial equilibrium state, particles have velocities less than those escaping from the halo. Particles with high velocities decrease with radius and disappear eventually, which indicates that the term in Equation (5.37), $\frac{df(v_0)}{dv_0}(r) \to 0$. The slowest velocity for the resonance (i.e., the fundamental tone) is given by $v_0(r) = \Omega/k(r)$. Therefore, the divergent point is determined by the period of the fundamental tone and the potential profile of the DM halo. The evolutional processes of NFW–1 are shown in Figure 5.8, which shows that the growth of the core scale saturates, as expected.

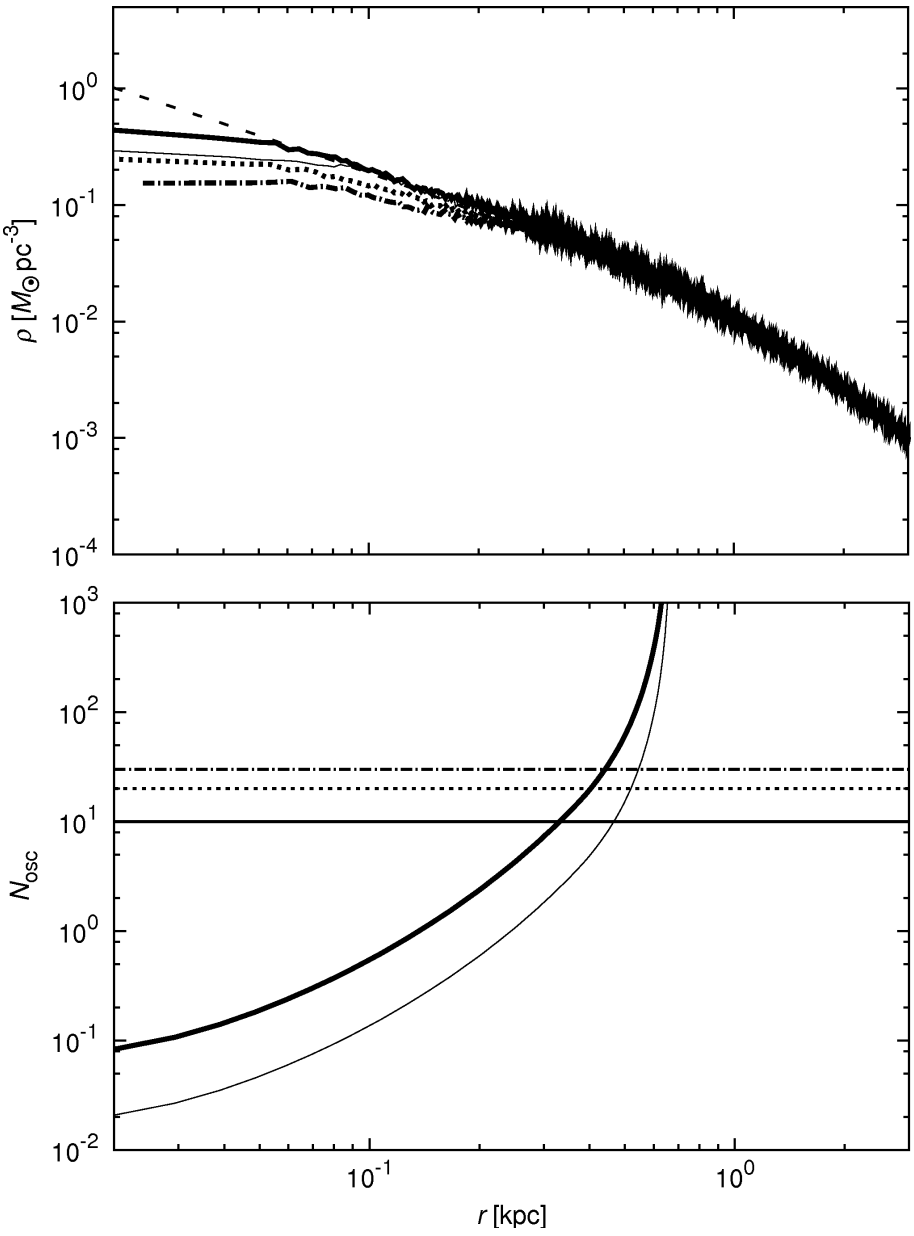

Fig. 5.9: Upper panel shows the evolutional process of the density profile of the DM halo (NFW–5) after 10 (solid line), 20 (dotted line), and 30 (dotted–dashed line) cycles. The thin solid and dashed lines express the results of NFW–1 after 10 cycles and the NFW profile, respectively. The lower panel shows $N_{\mathrm{osc}}(r)$ as a function of r. Thick and thin curves correspond to NFW–5 and NFW–1, respectively.

By a similar discussion, we argue the dependence on other parameters, $M_{\mathrm{b}}, R_{\mathrm{b,max}}$, and $R_{\mathrm{b,min}}$. In NFW–5, the mass of the external potential is set to half, and $T = \tau$. The amplitude of the potential change becomes smaller than those in the former runs, and a larger number of oscillation cycles is required to flatten the cusp. We compare N_{osc} of NFW–5 with that of NFW–1 in the lower panel of Figure 5.9. As expected, N_{osc} becomes larger than NFW–1; however, the divergent point is similar to that of NFW–1. The upper panel in the figure shows the evolutional processes of the density profile and demonstrates that the number of oscillation cycles required to reach the quasiequilibrium state is greater than that in the large amplitude case (NFW–1). However, the final state perfectly matches that of NFW–1.

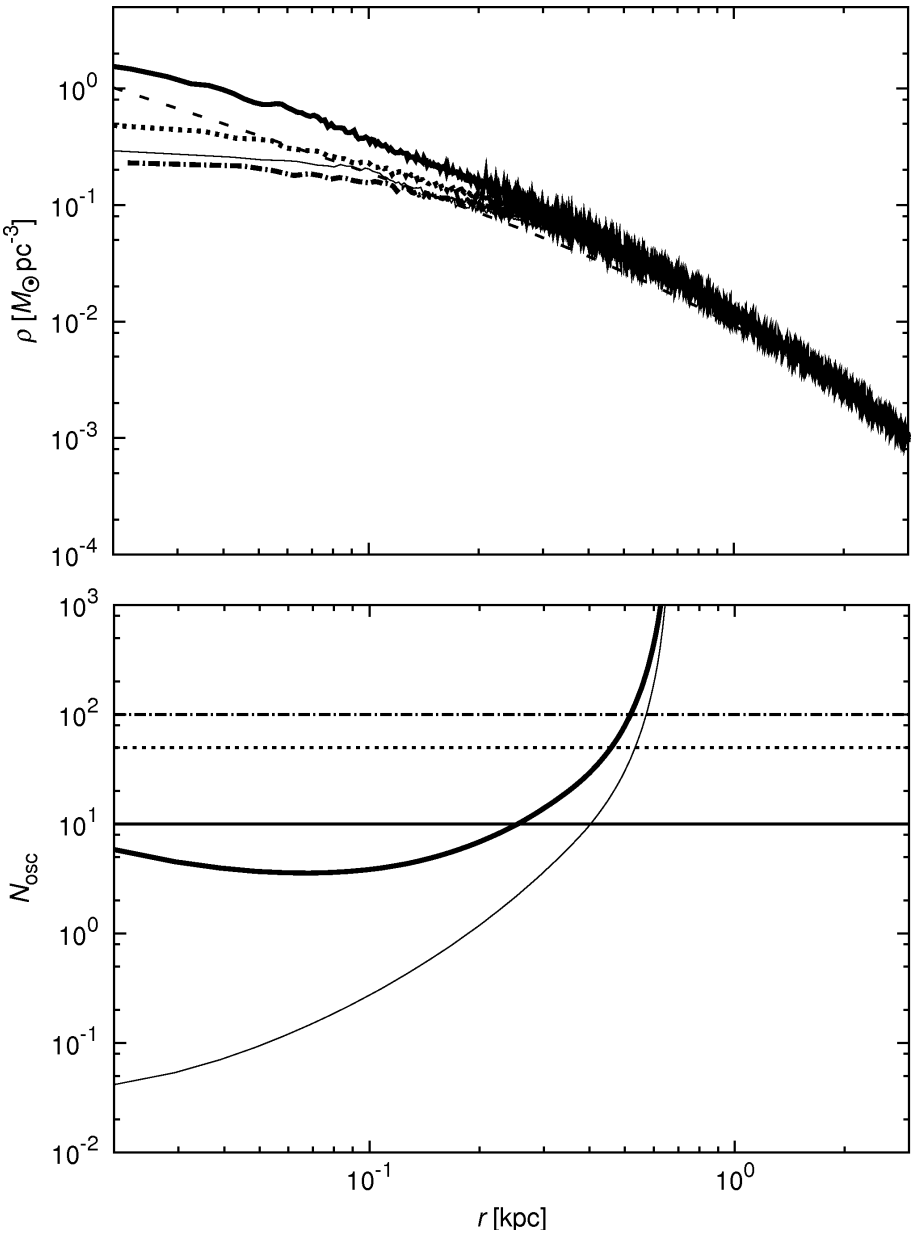

Fig. 5.10: Upper panel shows the evolutional process of the density profile of the DM halo (NFW–6) after 10 (solid line), 50 (dotted line), and 100 (dotted–dashed line) cycles. The thin solid and dashed lines express the results of NFW–1 after 10 cycles and the NFW profile, respectively. The lower panel shows $N_{\rm osc}(r)$ as a function of r. Thick and thin curves correspond to NFW–6 and NFW–1, respectively.

We set the minimum scale length of the external potential at $R_{\rm b,min} = 0.2$ kpc in NFW–6, which is comparable to the expected core scale obtained from the former results. The upper and lower panels in Figure 5.10 show the evolutional processes of the density profile and $N_{\rm osc}$ of the DM halo, respectively. Similar to the observation in NFW–5, $N_{\rm osc}$ becomes larger than NFW–1 because the amplitude of the potential change is smaller, and the divergent point of $N_{\rm osc}$ is similar to those observed in NFW–1 and NFW–5. As predicted by the argument of energy transfer rate, approximately 100 oscillation cycles are required to flatten the central cusp (upper panel). The DM halo then reaches the states of NFW–1 and NFW–5.

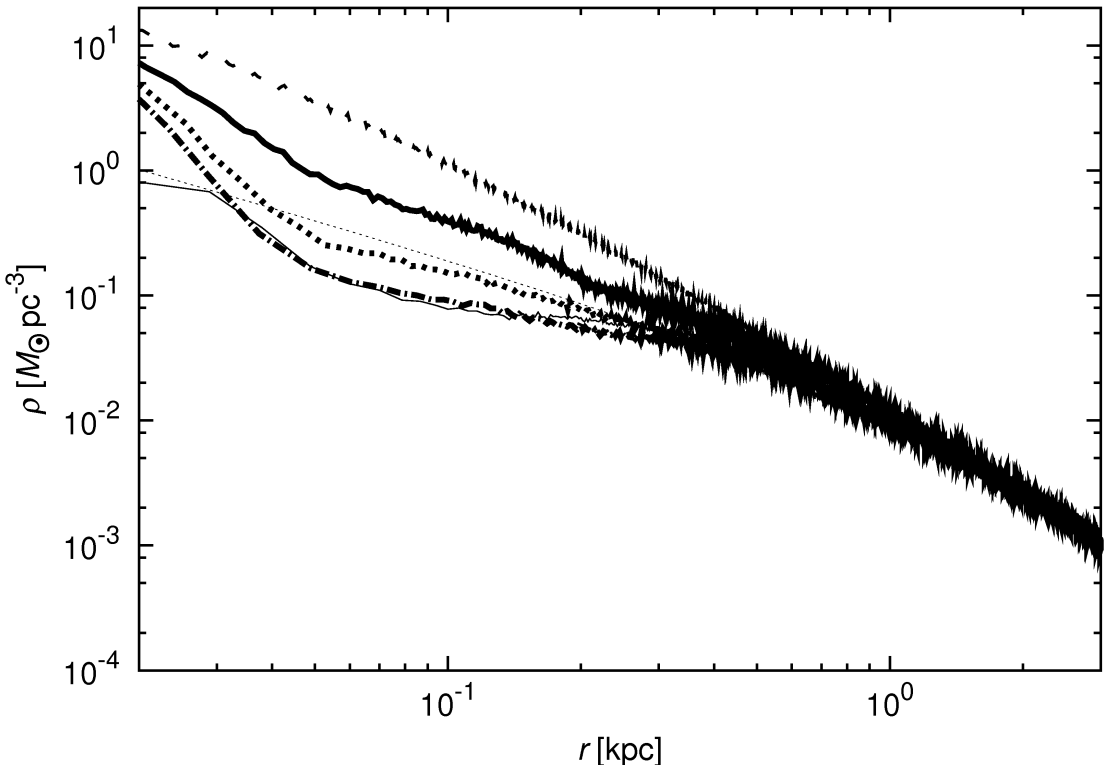

Fig. 5.11: Evolutional process of the density profile of the DM halo (NFW-7) after 10 (solid line), 30 (dotted line), and 50 (dotted-dashed line) cycles. The thin solid and thin dashed lines indicate the conditions after 10 cycles of the NFW–8 and NFW profiles, respectively. The thick dashed line represents the initial condition, which significantly deviates from the NFW profile because the DM halo has relaxed with the static external potential with $R_{\rm b,0} = 0.1$kpc.

In the NFW–7 and NFW–8 runs, because we set $R_{\rm b,0} = 0.1$ kpc, the DM halos contract significantly because of the deep potential depth of the static external potential and deviate from the NFW profile near the innermost region. $R_{\rm b,max} = 0.2$ kpc set in NFW–7 is comparable to the core scale predicted by our analytical model and the resultant core scale created in the runs of $T = \tau$ (NFW–1, NFW–5, and NFW–6). Figure 5.11 demonstrates the bump (NFW–7) and core (NFW–8) structures appearing near $r = 0.2 \sim 0.3$ kpc, around which the resonant condition for $T = \tau$ is satisfied. However, even if the number of cycles exceeds 50, the central cusp remains in NFW–7. Because the amount of change between $R_{\rm b,min}$ and $R_{\rm b,max}$ is quite small, the external potential acts as an almost static potential. In Figure 5.11, the mass density of NFW–7 decreases gradually in this region, which implies that the cusp–to–core transformation may occur if the number of oscillation cycles is increased further. Because the system deviates from the equilibrium NFW model during the relaxation process with the static potential, Widrow's DF is not appropriate for these runs, and thus we cannot evaluate dK/dt.

Meanwhile, we demonstrate that even if the amplitude of the potential change is small, the resultant density profile is quite similar when the oscillation period, T, is same. From these results, we conclude that the period of the oscillation process is an important factor in determining the resultant dynamical state governed by the resonance mechanism.

5.4.2 Implications

Gas oscillation is directly correlated with the stellar activity of galaxies. In recent years, highly accurate measurements of the SFH and the density profile of nearby dwarf galaxies have been reported. For example, research includes NGC 2366, NGC 6822, and Holmberg II (Table 5.3), which have core structures at their centers (Weldrake et al. 2003; Oh et al. 2008, 2011) and episodic SFHs (McQuinn et al. 2010a,b). Their dynamical time at the core scale corresponds approximately to the intervals of their episodic star formation activities. These galaxies conceivably justify the resonance condition predicted by Equation (5.21) at the core scale. Yoshii & Arimoto (1991) studied the color changes in galaxies by using the oscillating star formation history. They revealed that oscillatory star formation activity changes the color of galaxies with time and imprints its record in the two–color diagram. The oscillation period will be measured more precisely in future observations.

Table. 5.3: Comparison with observational results

Galaxy	$r_{\rm core}$ [kpc]	$\rho(r_{\rm core})$ [$M_\odot {\rm pc}^{-3}$]	$t_{\rm d}(r_{\rm core})$ [Myr]	$\tau_{\rm SF}$ [Myr]
NGC 2366	0.6	0.05	40	~ 100
NGC 6822	1	0.03	50	~ 100
Holmberg Ⅱ	0.5	0.03	50	~ 100

Note: Approximated values of NGC 2366, NGC 6822, and Holmberg II. $r_{\rm core}$ is the observed core radius, and $\rho(r_{\rm core})$ is the mass–density at $r_{\rm core}$. We obtain these values from Weldrake et al. (2003; NGC 6822) and Oh et al. (2008, 2011; NGC 2366, Holmberg II). We estimate the dynamical time at $r_{\rm core}$, $t_{\rm d}(r_{\rm core})$ using Equation (5.18). $\tau_{\rm SF}$ is the interval of star formation in these galaxies, which was obtained from McQuinn et al. (2010a, 2010b).

So far, we have assumed that the baryon potential oscillates with the constant period and that the baryon potential is always active. However, in the real less–massive galaxies, the period changes with time, and the potential well is shallower because their gas components are gradually ejected by stellar feedback. At the same time, the degree of potential change weakens. After ejection of gas components from the galaxies, the central cusp does not recover because this process decreases the densities of DM halos (e.g., Navarro et al. 1996a; Gnedin & Zhao 2002; Read & Gilmore 2005; Ogiya & Mori 2011; Ragone-Figueroa et al. 2012). To understand the fundamental physical mechanism of the cusp–to–core transformation of DM halos, we have employed an ideal model.

5.5 N–body + SPH Simulations

As mentioned above, the period of change in the gravitational potential will vary with time. In order to examine our analytical model in more realistic situations, we carry out N–body + Smoothed Particle Hydrodynamics (SPH) simulations. The period and amplitude of the potential change will be determined self–consistently.

5.5.1 Radiative Cooling

Radiative cooling is one of the important physical processes in galaxy formation and evolution (e.g., Rees & Ostriker 1977). The amount of energy radiates away from the i–particle per unit time is given by

$$\left(\frac{dU_{\rm i}}{dt}\right)_{\rm cool} = -\Lambda(T_{\rm i}) n_{\rm i}^2 \frac{m_{\rm i}}{\rho_{\rm i}}, \tag{5.38}$$

where $U_{\rm i}$, $T_{\rm i}$, $m_{\rm i}$ and $n_{\rm i}$ are the internal energy, temperature, mass and number–density of the i–particle, respectively. Λ is the cooling function. We adopt that calculated by Sutherland & Dopita (1993) for primordial gas. The cooling function is derived under the condition of the collisional ionization equiliblium, over a range of $T = 10^4 - 10^{8.5}$K. We assume that the radiative cooling terminates below $T = 10^4$K. This assumption corresponds to neglecting the molecular cooling. For $T > 10^{8.5}$K, we consider the bremsstrahlung process.

The net change ratio of the internal energy of the i–particle is represented by

$$\left(\frac{dU_{\rm i}}{dt}\right)_{\rm net} = \left(\frac{dU_{\rm i}}{dt}\right)_{\rm ad} + \left(\frac{dU_{\rm i}}{dt}\right)_{\rm cool}, \tag{5.39}$$

where $(dU_{\rm i}/dt)_{\rm ad}$ is the change ratio of the internal energy due to the ordinary adiabatic gas physics evaluated by Equation (3.14). In order to determine the amount of energy radiated away at a given time, we solve Equation (5.39) implicitly. Here, the calculation of $(dU_{\rm i}/dt)_{\rm ad}$ is completed before we solve Equation (5.39).

5.5.2 Star Formation and Supernova Feedback

A lot of effort has been made to accelerate computing and the resolution of numerical simulations has been advanced dramatically. However, it is still insufficient to resolve individual stars, supernova (SN) explosions or the fine structure of star–forming gas clouds in the simulations for galaxy formation and evolution. Hence, we have to use the physical recipes which are heuristic to model star formation and effects of SN explosions. We adopt the recipe proposed by Stinson et al. (2006).

Star Formation

The criteria which have to be satisfied by gas particles to form stars are as follows.

(1) The gas particle must be colder than $T_{\rm max} = 15000$K.

(2) The gas particle must be denser than $n_{\rm min} = 10{\rm cm}^{-3}$.

(3) The particle must be part of a converging flow, i.e. $\nabla \cdot \mathbf{v} < 0$.

Then, we determine whether the gas particles which satisfy the criteria form stars by a probabilistic method based on the Kennicutt–Schmidt law of star formation rate (SFR; Schmidt 1959; Kennicutt 1998). The Kennicutt–Schmidt law implies $d\rho_{\rm SFR}/dt \propto \rho_{\rm gas}^{3/2}$, where $\rho_{\rm gas}$ is the gas density. The volume desnity of SFR is approximated by $d\rho_{\rm SFR}/dt \propto \rho_{\rm gas}/t_{\rm form}$, where $t_{\rm form}$ is the time–scale of star formation. Here, we

choose $t_{\rm form} = t_{\rm d,gas} \propto \rho_{\rm gas}^{-1/2}$ where $t_{\rm d,gas}$ is the dynamical time of the star–forming gas cloud. Thus one can express the law of SFR by

$$\frac{d\rho_{\rm SFR}}{dt} = c^* \frac{\rho_{\rm gas}}{t_{\rm d,gas}}, \tag{5.40}$$

where c^* is a parameter to control the efficiency of star formation.

Stinson et al. (2006) proposed a stochastic recipe for when and where stars should form. One can take the probability that a star will form as

$$p = \frac{m_{\rm gas}}{m_*}[1 - \exp\left(-c^* \Delta t_{\rm sf}/t_{\rm d,gas}\right)], \tag{5.41}$$

where $m_{\rm gas}$ and m_* mean the mass of the gas particle and stellar mass formed in the time interval, $\Delta t_{\rm sf}$. We determine the gas particles form stars at intervals of $\Delta t_{\rm sf} = 1$Myr, and estimete the stellar mass formed in the time interval by $m_* = c^* m_{\rm gas}(\Delta t_{\rm sf}/t_{\rm d,gas})$. We assume the lifetime of massive stars which explode as type II supernovae (SNe II), $t_{\rm life} = 10$Myr. Assuming Salpeter's IMF (Salpeter 1955), we can evaluate the number of supernovae, $N_{\rm SN}$, from m_* for each gas particle. We do not create collisionless particles which express stars, and regard stars as just heating sources.

Supernova Feedback

After spending $t_{\rm life}$, massive stars explode and give thermal energy to nearby gas particles. The energy of $E_{\rm SN} = 10^{51}$erg is released from a SN. We evaluate the total released energy from the i–particle by multiplying $E_{\rm SN}$ by $N_{\rm SN,i}$. Here, $N_{\rm SN,i}$ is the number of SNe II explode in the i–particle. The gas particles which release thermal energy are determined at intervals of $\Delta t_{\rm sf}$. The amount of received energy by the j–particle which is one of the neighbors of the i–particle is determined by

$$\Delta E_{\rm SN,j} = E_{\rm SN} N_{\rm SN,i} \frac{m_{\rm j} W(r_{\rm ij}, h_{\rm j})}{\rho_{\rm j}}, \tag{5.42}$$

where W means the kernel function defined by Equation (3.10), and $m_{\rm j}$, $h_{\rm j}$, and $r_{\rm ij}$ are the mass and smoothing length of the j–particle, and the distance between the i– and j–particles, respectively.

Stars are formed in dense gas clouds and SNe explode in such regions. Bacause of the finite resolution and inability to resolve the complex multiphases of the interstellar medium properly, the heated gas particle will cool by radiative cooling before they impact their envelopes strongly. However, SNe should lead to blastwaves around them, and the gas will be kept hot during the blastwave phase (e.g., Sedov 1959; McKee & Ostriker 1977). In order to model the effects of the supernova feedback more realistically, Stinson et al. (2006) proposed a method in which we make radiative cooling disabled for a certain time. Mori et al. (1999) have proposed a similar method earlier. Stinson et al. (2006) determined the time to disable radiative cooling, $t_{\rm blast}$, as a function of the density and pressure of the envelope of the SN (McKee & Ostriker 1977). We set $t_{\rm blast} = 10$Myr for simplicity.

5.5.3 Set Up

We set up a spherical DM halo and embed a gaseous component in the DM halo. They follow an NFW profile (Navarro et al. 1997) with the concentration parameter, $c = 5$. The virial mass, virial radius and scale length of the DM halo are $M_{\rm vir} = 10^9 M_\odot$, $R_{\rm vir} = 10$, and $R_{\rm DM} = 2$ kpc, respectively. The gaseous component has the same virial radius and scale length with the DM halo, and the total gas mass is $M_{\rm b} = 2 \times 10^8 M_\odot$. The mass ratio between DM and baryon, $M_{\rm vir}/M_{\rm b} = 5$, is consistent with the cosmic baryon fraction obtained from Wilkinson Microwave Anisotropy Probe (*WMAP*) observations (Spergel et al. 2007; Komatsu et al. 2009, 2011). The N–body systems which express the DM halos are generated in the

equilibrium state by using the fitting formulation of the distribution function proposed by Widrow (2000). Here, we also take into account the mass of the baryonic component. Initially, the velocity of gas articles is $\mathbf{v} = 0$, and their internal energy is determined to be in the equilibrium with the gravitational potential of DM and baryon (Kaufmann et al. 2006, 2007).

We use 1 048 576 collisionless particles for DM and 131 072 gas particles. The softening length is $\epsilon = 20$pc and the number of neighbor particles is $N_{\rm ngb} = 32 \pm 3$. In order to test the stability of the system, we perform a run without radiative cooling, star formation and supernova feedback. As shown in Figure 5.12, the system keeps the initial configuration at least for 1 Gyr.

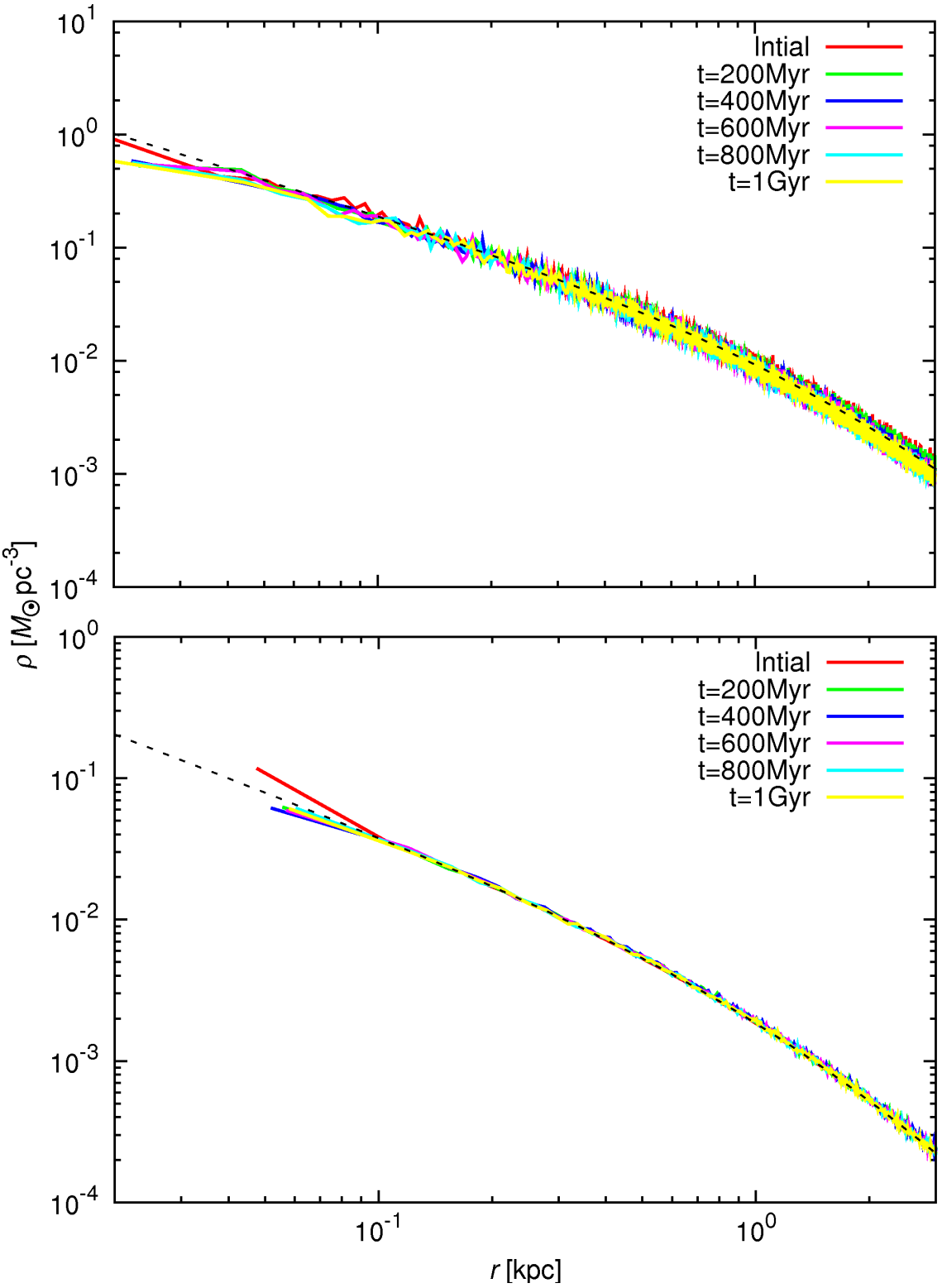

Fig. 5.12: Colored lines show the evolution of the density profiles of the nonperturbed (equilibrium) DM halo (top) and gas component (bottom). Black dashed lines represent the analytical formulation given by Equation (5.23).

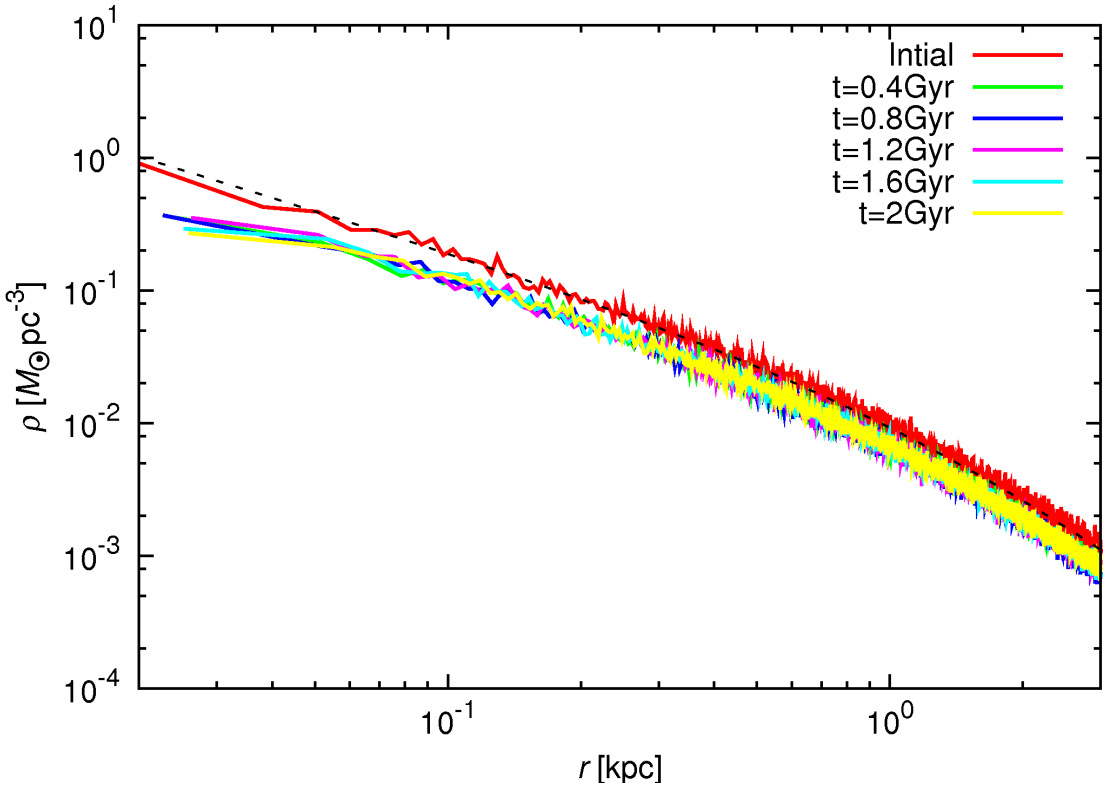

Fig. 5.13: Colored lines show the evolution of the density profile of the DM halo after the gas mass–loss. Black dashed line is the same as that in the top panel of Figure 5.12.

According to Ogiya & Mori (2011), the change in the galactic potential due to the gas mass–loss does not impact the central cusps of DM halos strongly. They found the central cusp is flatter when the mass–loss occurs over a short time than when it occurs over a long time (see also Hills 1980). In order to test that result, we also carry out an additional N–body simulation which corresponds to the instantaneous mass–loss case. In this simulation, the initial condition of the N–body system is the same as that of the equilibrium test performed above, i.e., the potential depth of baryon is taken into account. We remove the all mass of gas particles instantaneously. Figure 5.13 shows that it is tough to flatten the cusp by the mass–loss, as expected.

5.5.4 Results

Here, the efficiency of star formation, c^*, is parameterized. We carry out N–body + SPH simulations for $c^* = 0.01$ and 0.05.

Figure 5.14 demonstrates the sequence of events that produces episodic star formation. First, the gas lose its internal energy by radiative cooling, and infalls towards to the center. It triggers a starburst. The subsequent supernova feedback expells the gas from the galactic center. After the adiabatical expansion of the gas, the star formation is terminated since the gas becomes less dense. This cessation of star formation allows the gas to cool, contract, and become dense enough to form stars again. Then, the process repeats in another cycle of star formation, gas expansion and cooling. As described above, an episodic star formation history naturally arises in an isolated galaxy (e.g., Stinson et al. 2007).

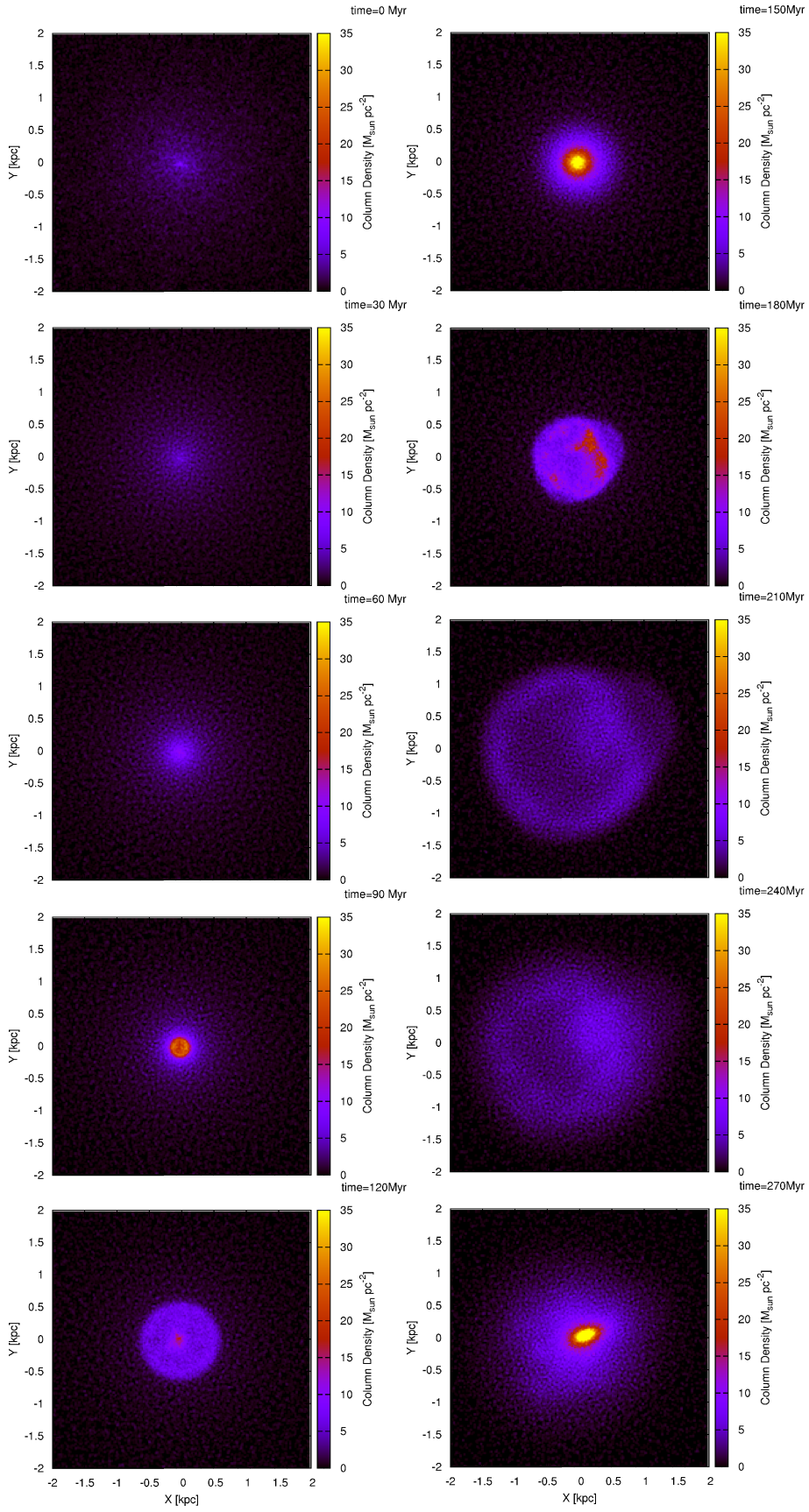

Fig. 5.14: Sequence of events that produces an episodic star formation history in the $c^* = 0.01$ run. Color coordination means the projected gas density in the X–Y plane. The corresponding time is denoted at the upper right corner of each panel.

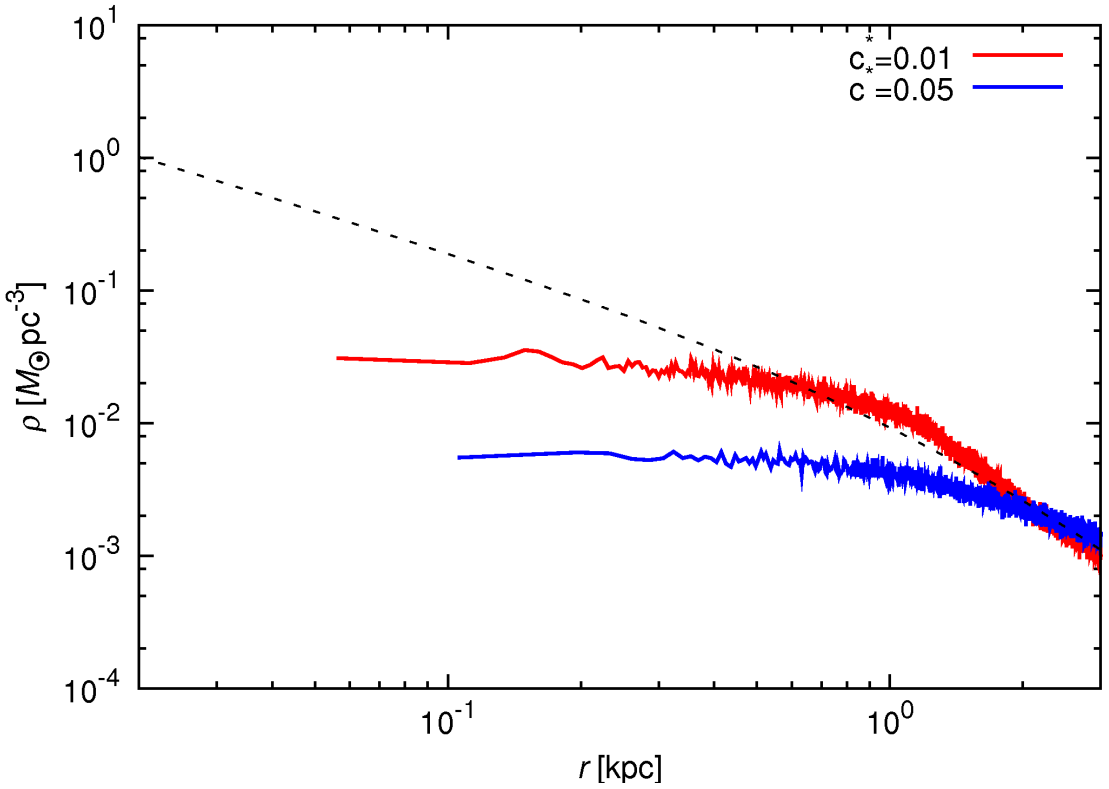

Fig. 5.15: Density profile of DM halos measured at $t = 1$ Gyr. Red and blue lines represent $c^* = 0.01$ and 0.05, respectively. Black dashed one is the initial condition.

The repeating gas inflow and outflow lead a recurring change in the galactic potential. It is possible that such oscillations in the gravitational potential modify the central cusp into a flat core (e.g., Mashchenko et al. 2008; Pontzen & Governato 2012; Ogiya & Mori 2012). Figure 5.15 shows that the central cusps are flattened out into cores within 1 Gyr. The core size created in the run of $c^* = 0.05$ (blue) is larger than that in $c^* = 0.01$ (red).

The upper panel in Figure 5.16 represents the SFHs observed in simulations. It clearly shows the repetitive process of the starburst and cessation of star formation activity. The interval between two cycles which corresponds to the period of gas oscillation in the run of $c^* = 0.05$ is longer than that of the $c^* = 0.01$ run, because a larger amount of energy is released in a starburst. The upper panel of Figure 5.16 clearly demonstrates that. Interestingly, in the $c^* = 0.05$ run, a larger core is created, in spite of the smaller number of SNe II (total amount of input energy) at $t = 1$ Gyr (see the lower panel of Figure 5.16).

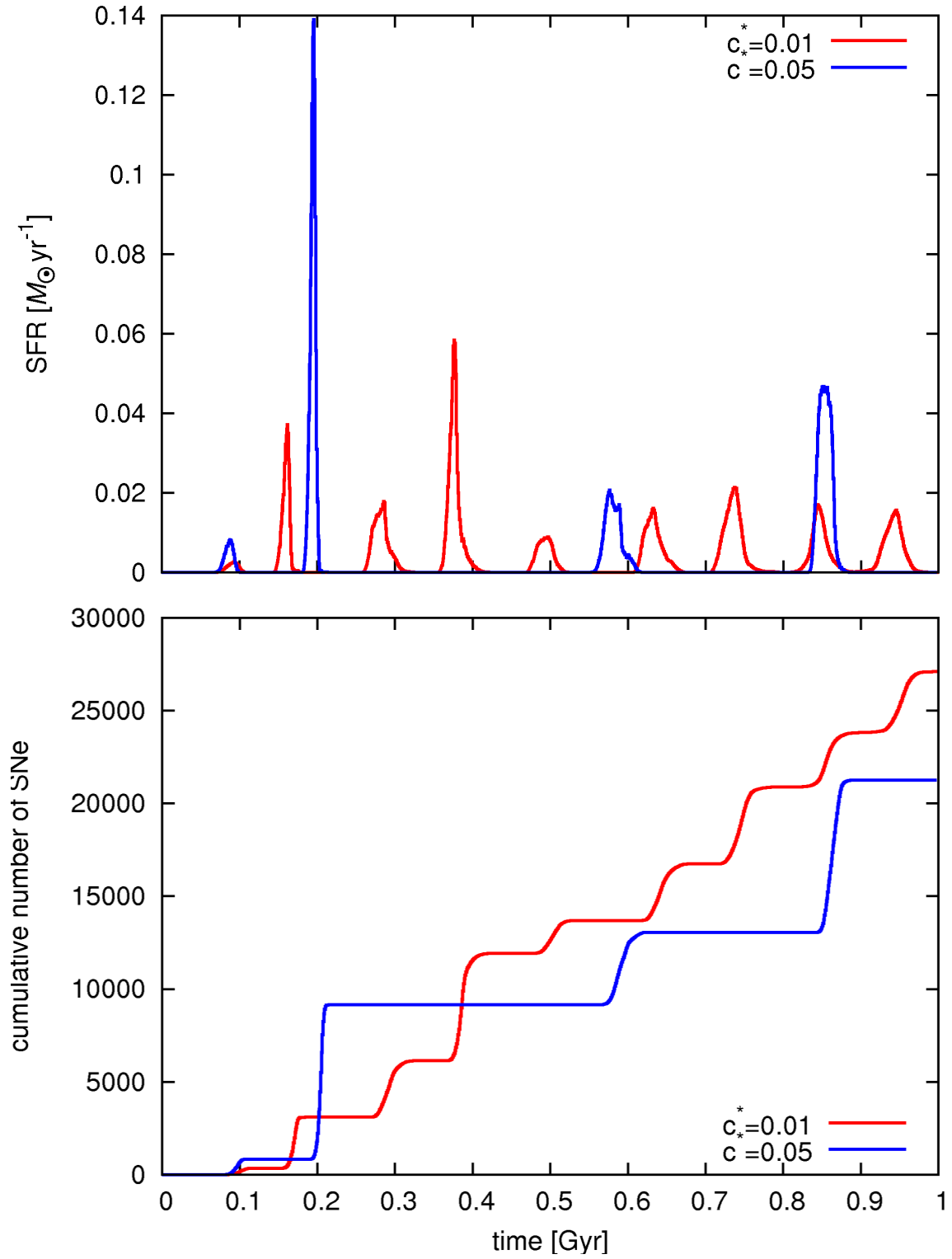

Fig. 5.16: (*Upper*) Star formation histories of simulated galaxies. (*Lower*) Cumulative number of SNe II which corresponds to the input energy as a function of time. Each line represents the same run within Figure 5.15.

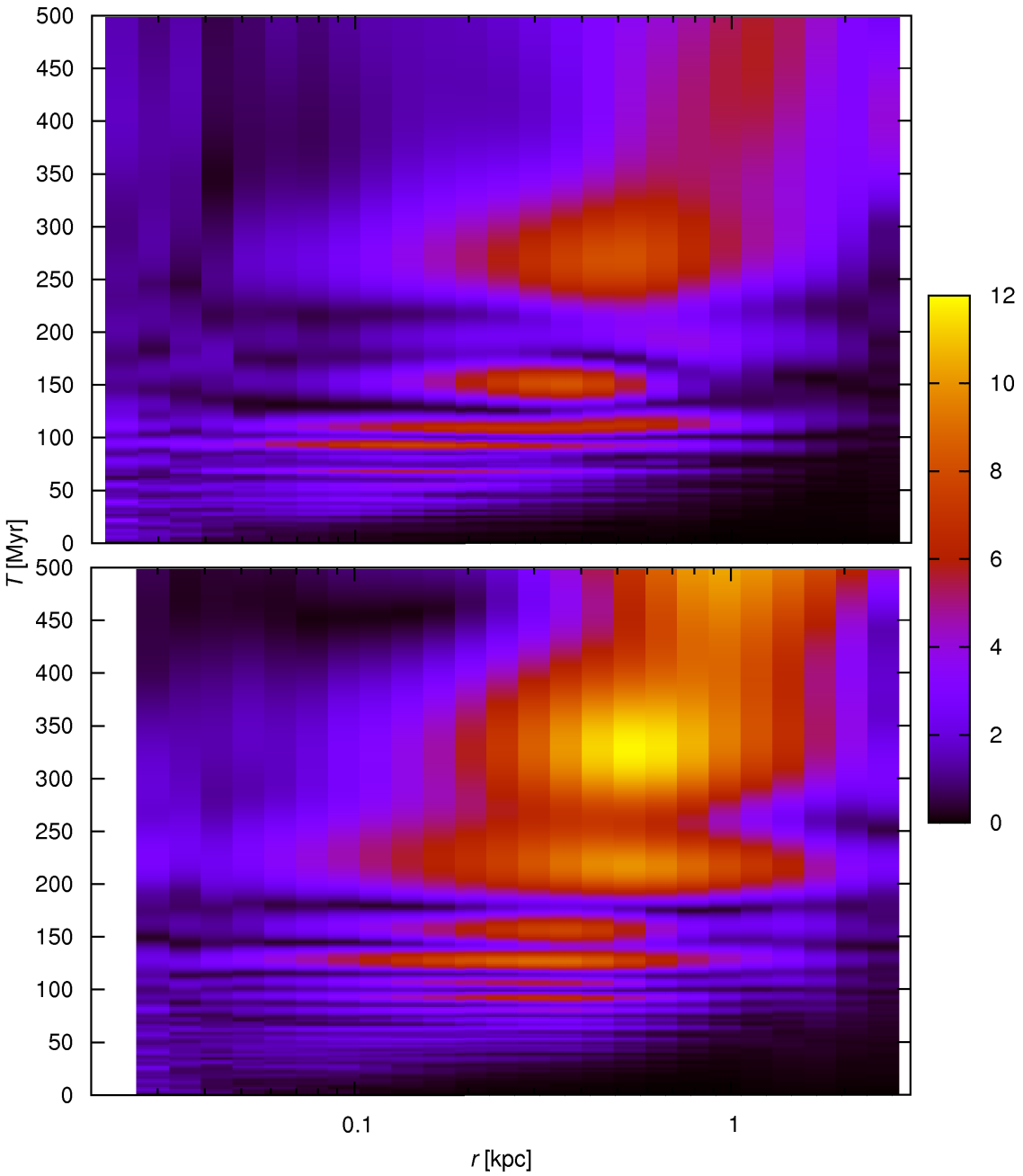

Fig. 5.17: Fourier spectrum of radial velocity as a function of radius, r, and corresponding period, T. Upper and lower panels show the results of $c^* = 0.01$ and 0.05, respectively.

According to the analytical model of the resonance between DM particles and density waves of the interstellar gas proposed in §5.2, the recurring potential change due to the gas oscillation with a longer period affects dynamically over a wider region, because oscillation with a long period contains a variety of modes.

We verify that by the Fourier spectrum of radial velocity in Figure 5.17. On can see that the DM halo in the $c^* = 0.05$ run is impacted more strongly and over a wider range than that in the $c^* = 0.01$ run. The DM halo simulated in the $c^* = 0.05$ run gains kinetic energy efficiently from the recurring change in the gravitational potential through the resonance between DM particles and density waves of the galactic gas. As a consequence of the efficient energy tranfter, the central cusp is flattened out and a large core is created in the run of $c^* = 0.05$.

The SFH of galaxies and density profile of DM halos obtained in the N–body + SPH simulations are similar to observational results (e.g., interval between starbursts, SFR and core size of DM halos). We will enforce additional studies to verify the resonance mechanism by comparing simulation data with observations.

5.6 Conclusion

We have studied the dynamical response of DM halos to recurring changes in the gravitational potential of the interstellar gas near the centers of the DM halos. A resonance model between the DM particles and the oscillating external potential is proposed to understand the physical mechanism of the cusp–to–core transformation of DM halos. We determine that the collisionless system effectively gains kinetic energy from the energy transfer driven by the resonance between the DM particles and the density waves induced by the oscillation of the gravitational potential of the interstellar gas. The condition for the cusp–to–core transformation is such that the oscillation period of the baryon potential is the same as the local dynamical time of the DM halo. That is, the resonance condition at a given radius, r, is represented by $t_{\rm d}(r_{\rm core}) = T$, and the overtone modes are in the resonant states. In addition, the core radius of the DM halo after the cusp–to–core transformation driven by the resonance is shown using the conventional mass–density profile of DM halos, which is predicted by the cosmological structure formation models. Moreover, we verify our analytical model using N–body simulations, whose results validate our resonance model. Therefore, we conclude that the resonance between the DM particles and the oscillation of the baryon potential plays a key role in solving the core–cusp problem of CDM halos. We also perform N–body + SPH simulations to test the perceptions obtained from the analytical model. The results clearly show that the energy transfer through the resonance works well in the more realistic simulations.

Part IV

Summary

Chapter 6 Summary

In this thesis, to resolve the core–cusp problem which is well known as an open question on the present standard paradigm, the cold dark matter (CDM) cosmology, I study the dynamical structure of dark matter (DM) halos. Firstly, I investigate the relation between the scenario of the cusp–to–core transformation and the observational universalities of DM halos. Secondly, to perform large–scale simulations, I develop a tree code designed for GPU clusters. I also extend it to the smoothed particle hydrodynamics (SPH). Then, using numerical simulations, mainly collisionless N–body simulations, I study the dynamical response of DM halos to the gas mass–loss and gas oscillation. The results obtained in each part are summarized below.

The Connection between the Cusp–to–Core Transformation and Observational Universalities of Dark Matter Halos

I examine the $c(M_{200}, z)$, dependence of the concentration parameter of NFW profiles, c, on virial mass of halo, M_{200}, and redshift, z, proposed by Prada et al. (2012) using the data of the cosmological N–body simulation carried out by Ishiyama et al. (2013). The analysis shows the $c(M_{200}, z)$ proposed by Prada et al. (2012) is appropriate down to the mass scale of dwarf galaxies.

The scenario of the cusp–to–core transformation naturally reproduces the $\mu_{0\mathrm{D}}$ relation which is one of the observational universalities of DM halos recently found. The central density of the Burkert profile, ρ_0, is almost independent of M_{200}. This means ρ_0 only depends on z. Thus, considering ρ_0 enable us to estimate the formation redshifts of DM halos. This result implies that the cores of DM halos retain a memory of their formation redshift.

I find that the $\mu_{0\mathrm{D}}$ and Strigari relations are consistent with each other among DM halos surround dSphs orbiting around the Milky Way. However, this consistency breaks down for halos which have larger core structures. The $\mu_{0\mathrm{D}}$ relation holds good in a broader range of halo mass than Strigari relation. Therefore, Strigari relation is an indirect evidence of the $\mu_{0\mathrm{D}}$ relation.

A Tree–SPH Code Developed for GPU Clusters

I propose a method to accelerate the tree–traversal part whose computatinal cost is dominant in the tree algorithm by GPUs. It is an improvement of the method proposed by Nakasato (2012): To achieve a high cache hit rate and to decrease the frequency of warp branches, I bundle the route of particles computed gravitational force while they traverse the tree–structure. This method also suppress the accesses to the slow memory. The method accelerate the tree–traversal part by 3.6 times. I apply Peano–Hilbert curve in substitution for Morton curve which adopted in Nakasato (2012), and the GPU function becomes 10 % faster. Combining them, the GPU function of the tree–traversal is accelerated by 4 times.

I parallelize the code with MPI. The adopted policy is similar to that of parallel CPU codes generally used. The code achieves a performance to compute the gravity among a billion particles within about 18 seconds per time. It enables us to perform collisionless N–body simulations with such a number of particles within a reasonable computation time.

I also extend the code to SPH. The method of the route bundling of particles accelerates some of GPU functions implemented for SPH.

Dynamical Effects of Gas Mass–Loss on Dark Matter Halos

I study the dynamical response of DM halos to the gas mass–loss using collisionless N–body simulations. Some previous studies have been limited by the effects of artificial two–body relaxation. I remove such effects by employing a sufficient number of particles in simulations. I focus on the timescale of the mass–loss. The results of simulations show that the central cusp of the DM halo becomes flatter when mass–loss occurs over a short time than when it occurs over a long time. Hence, the timescale of mass–loss is an important factor to determine the dynamical state of DM halos. Although the central density of DM halos decreases in some degree, the central cusp is still remained even though the mass–loss occurs instantaneously. Therefore, the mass–loss model is ineffective to flatten the central cusp at least in spherical systems.

Dynamical Effects of Gas Oscillation on Dark Matter Halos

I investigate the dynamical response of DM halos to recurring changes in the gravitational potential. To understand the fundamental physical mechanism of the cusp–to–core transformation of DM halos, I construct an analytical model of the resonance between DM particles and the oscillating external potential. This model shows that the systems effectively gain kinetic energy from the external potential through the resonances. I find the resonance condition is that the oscillation period of the baryon potential is the same as the local dynamical time of DM halos. Since the local dynamical time is defined as a function of the distance from the center, r, the resonance condition is represented by $t_{\rm d}(r_{\rm core}) = T$, where $r_{\rm core}$ and T are the core size and the period of the potential change, respectively. Solving this equation by using the inversion procedure, the analytical model allows us to estimate the resultant core size created through the resonance. I estimate the core size for the conventional mass–density profile of CDM halos. The energy transfer rate from the oscillatory change in the galactic potential to DM halos is duscussed and such argument predicts the number of oscillation cycles required to flatten the cusp and core size. These predictions are verified using collisionless N–body simulations. N–body + SPH simulations reveal that the resonance mechanism works well in the more realistic situations. Hence, I conclude that the resonance between DM particles and the density waves of the interstellar gas plays a key role in solving the core–cusp problem of CDM halos.

Acknowledgement

A number of people have helped and encouraged me during my Ph.D days. Thanks to them, I finally finished up my Ph.D thesis. I thank all of them. The following is my acknowledgment to those who gave me a lot of help.

I am really grateful to my supervisor, Prof. Mori at University of Tsukuba, for giving me a lot of helpful advices and useful discussions. His comments contain fruitful implications and always encourage me. He also provided many chances to me. They helped me to discover new horizons, to look abroad and to get necessary experiences to survive difficult situations. I enjoyed working with him very much. I thank him again for his kind assistance.

I greatly thank Prof. Umemura at University of Tsukuba, Dr. Yoshikawa, Dr. Okamoto, and Dr. Kawakatsu for giving me meaningful comments and questions. They brushed up my study significantly. Prof. Umemura gave me opportunities to use FIRST simulator. That was my first time to use supercomputer. Gained experiences have supported me. Comments from Dr. Yoshikawa, Dr. Okamoto and Dr. Kawakatsu were sometimes strict but much helpful. Dr. Okamoto also made a key suggestion to construct the numerical models.

I wish to acknowledge numerous encouragements and advices from Dr. Tanikawa, Dr. Hasegawa, Dr. Kawaguchi, Dr. Wagner and Dr. Namekata. They are very good examples for me to follow. Dr. Tanikawa told me basic skills of numerical simulations and discussed GPGPU with me. Dr. Hasegawa always cared about me and gave a fruitful chance to have a seminar at Paris Observatory. Dr. Kawaguchi advised me on a good way to make documents and presentation files. Dr. Wagner helped me to emend an English manuscript. Dr. Namekata discussed SPH with me and gave me some important advices.

I express my sincere thanks to Prof. Boku, Prof. Kodama, and Prof. Takahashi at University of Tsukuba, Prof. Hanawa at University of Tokyo and Prof. Nakasato at University of Aizu for providing useful comments to develop GPU codes and to measure their performance. Prof. Boku was my supervisor in the computer science division. He let me join the world of high performance computing. Its culture and common sense were much different from those of astrophysics. Such experiences broadened my perception. Prof. Nakasato gave me some critical ideas and hints to much accelerate the GPU code.

Prof. Burkert at Ludwig–Maximilians–Universität München and Dr. Ishiyama helped and encouraged me as my collaborators. Our collaboration has started from Prof. Burkert's suggestion. He also gave me a critical comment to improve the numerical model. Dr. Ishiyama provided the data of his simulations to me. I greatly appreciate them.

I thank Prof. Semelin at Paris Observatory, Prof. Nakai at University of Tsukuba, Prof. Susa and Prof. Tominaga at Konan University, and Prof. Nitta at National University Corporation Tsukuba University of Technology for giving me fruitful opportunities to discuss my study with them. Thanks to Prof. Semelin's comment, I was able to improve the analytical model much.

I would like to acknowledge all of my classmates, seniors, and juniors in the theoretical astrophysics group and HPCS laboratory of University of Tsukuba for discussions and supports. Especially, my classmate, Yohei Miki helped me in various occasions. Discussions with him were very fruitful time for me. He was my best friend as well as my best rival. I also thank him for providing me his index–generation code of Peano–Hilbert curve.

I express thanks to secretaries and engineers at University of Tsukuba. Thanks to their work, I always felt comfortable in our laboratory and on my trips. Numerical simulations were performed on the supercomputers at the Center of Comupational Sciences of University of Tsukuba, FIRST simulator, T2K–Tsukuba and HA–PACS.

I would like to express my best thanks to my father, Tomonari, mother, Masako, brother, Shunji, and sister, Chisato. They always accept me for what I am and encourage me greatly. Finally, I wish to send my sincere thanks to my wife, Nana. Being with her gives me a lot of energy. I was not able to finish up my Ph.D thesis without her support. Nana–san, thank you so much for all your help.

This work was supported by Research Fellowship of the Japan Society for the Promotion of Science (JSPS) for Young Scientists.

References

[1] Agertz, O., Moore, B., Stadel, J., et al. 2007, MNRAS, 380, 963

[2] Balsara, D. S. 1995, Journal of Computational Physics, 121, 357

[3] Barnes, J., & Hut, P. 1986, Nature, 324, 446

[4] Barnes, J. E. 1990, Journal of Computational Physics, 87, 161

[5] Bédorf, J., Gaburov, E., & Portegies Zwart, S. 2012, Journal of Computational Physics, 231, 2825

[6] Belleman, R. G., Bédorf, J., & Portegies Zwart, S. F. 2008, New A, 13, 103

[7] Binney, J., & Tremaine, S. 2008, Galactic Dynamics: Second Edition (Princeton University Press)

[8] Bland-Hawthorn, J., Sutherland, R., & Karlsson, T. 2011, in EAS Publications Series, Vol. 48, EAS Publications Series, ed. M. Koleva, P. Prugniel, & I. Vauglin, 397–404

[9] Boyarsky, A., Neronov, A., Ruchayskiy, O., & Tkachev, I. 2010, Physical Review Letters, 104, 191301

[10] Boylan-Kolchin, M., Springel, V., White, S. D. M., Jenkins, A., & Lemson, G. 2009, MNRAS, 398, 1150

[11] Bromm, V., & Yoshida, N. 2011, ARA&A, 49, 373

[12] Bullock, J. S., Kolatt, T. S., Sigad, Y., et al. 2001, MNRAS, 321, 559

[13] Burkert, A. 1995, ApJ, 447, L25

[14] Cardone, V. F., & Del Popolo, A. 2012, MNRAS, 427, 3176

[15] Cardone, V. F., & Tortora, C. 2010, MNRAS, 409, 1570

[16] Cole, D. R., Dehnen, W., & Wilkinson, M. I. 2011, MNRAS, 416, 1118

[17] de Blok, W. J. G., McGaugh, S. S., Bosma, A., & Rubin, V. C. 2001a, ApJ, 552, L23

[18] de Blok, W. J. G., McGaugh, S. S., & Rubin, V. C. 2001b, AJ, 122, 2396

[19] de Souza, R. S., Rodrigues, L. F. S., Ishida, E. E. O., & Opher, R. 2011, MNRAS, 415, 2969

[20] de Vaucouleurs, G. 1948, Annales d'Astrophysique, 11, 247

[21] Dekel, A., & Silk, J. 1986, ApJ, 303, 39

[22] Del Popolo, A. 2009, ApJ, 698, 2093

[23] Diemand, J., Moore, B., & Stadel, J. 2004, MNRAS, 353, 624

[24] Donato, F., Gentile, G., Salucci, P., et al. 2009, MNRAS, 397, 1169

[25] Doremus, J.-P., Feix, M. R., & Baumann, G. 1971, Physical Review Letters, 26, 725

[26] Eisenstein, D. J., Zehavi, I., Hogg, D. W., et al. 2005, ApJ, 633, 560

[27] El-Zant, A., Shlosman, I., & Hoffman, Y. 2001, ApJ, 560, 636

[28] Elsen, E., Vishal, V., Houston, M., et al. 2007, ArXiv e-prints, arXiv:0706.3060

[29] Faber, S. M., & Jackson, R. E. 1976, ApJ, 204, 668

[30] Faerman, Y., Sternberg, A., & McKee, C. F. 2013, ApJ, 777, 119

[31] Fukushige, T., Kawai, A., & Makino, J. 2004, ApJ, 606, 625

[32] Fukushige, T., & Makino, J. 1997, ApJ, 477, L9

[33] Galli, D., & Palla, F. 1998, A&A, 335, 403

[34] Gentile, G., Salucci, P., Klein, U., Vergani, D., & Kalberla, P. 2004, MNRAS, 351, 903

[35] Gingold, R. A., & Monaghan, J. J. 1977, MNRAS, 181, 375

[36] Gnedin, O. Y., & Zhao, H. 2002, MNRAS, 333, 299

[37] Goerdt, T., Moore, B., Read, J. I., & Stadel, J. 2010, ApJ, 725, 1707

[38] Governato, F., Brook, C., Mayer, L., et al. 2010, Nature, 463, 203

[39] Governato, F., Zolotov, A., Pontzen, A., et al. 2012, MNRAS, 422, 1231

[40] HA-PACS. 2012, HA–PACS, `http://www.ccs.tsukuba.ac.jp/CCS/research/project/ha-pacs`

[41] Hamada, T., Narumi, T., Yokota, R., et al. 2009, in Proceedings of the Conference on High Performance Computing Networking, Storage and Analysis, ACM, 62

[42] Hayashi, K., & Chiba, M. 2012, ApJ, 755, 145

[43] Hernquist, L. 1990, ApJ, 356, 359

[44] Hernquist, L., & Katz, N. 1989, ApJS, 70, 419

[45] Hills, J. G. 1980, ApJ, 235, 986

[46] Hinshaw, G., Nolta, M. R., Bennett, C. L., et al. 2007, ApJS, 170, 288

[47] Ikuta, C., & Arimoto, N. 2002, A&A, 391, 55

[48] Inoue, S., & Saitoh, T. R. 2011, MNRAS, 418, 2527

[49] Ishiyama, T., Fukushige, T., & Makino, J. 2008, PASJ, 60, L13

[50] —. 2009, ApJ, 696, 2115

[51] Ishiyama, T., Rieder, S., Makino, J., et al. 2013, ApJ, 767, 146

[52] Jing, Y. P., & Suto, Y. 2000, ApJ, 529, L69

[53] Kaufmann, T., Mayer, L., Wadsley, J., Stadel, J., & Moore, B. 2006, MNRAS, 370, 1612

[54] —. 2007, MNRAS, 375, 53

[55] Kazantzidis, S., Zentner, A. R., & Kravtsov, A. V. 2006, ApJ, 641, 647

[56] Kennicutt, Jr., R. C. 1998, ApJ, 498, 541

[57] Khronos. 2011, The OpenCL specification, version 1.2, revision 16

[58] Klypin, A., Kravtsov, A. V., Bullock, J. S., & Primack, J. R. 2001, ApJ, 554, 903

[59] Klypin, A. A., Trujillo-Gomez, S., & Primack, J. 2011, ApJ, 740, 102

[60] Komatsu, E., Dunkley, J., Nolta, M. R., et al. 2009, ApJS, 180, 330

[61] Komatsu, E., Smith, K. M., Dunkley, J., et al. 2011, ApJS, 192, 18

[62] Kormendy, J., & Freeman, K. C. 2004, in IAU Symposium, Vol. 220, Dark Matter in Galaxies, ed. S. Ryder, D. Pisano, M. Walker, & K. Freeman, 377

[63] Kuzio de Naray, R., McGaugh, S. S., & de Blok, W. J. G. 2008, ApJ, 676, 920

[64] Kuzio de Naray, R., McGaugh, S. S., de Blok, W. J. G., & Bosma, A. 2006, ApJS, 165, 461

[65] Lam, W. M., & Shapiro, J. 1994, in Image Processing, 1994. Proceedings. ICIP-94., IEEE International Conference, Vol. 1, IEEE, 638–641

[66] Łokas, E. L., Kazantzidis, S., & Mayer, L. 2012, ApJ, 751, L15

[67] Lucy, L. B. 1977, AJ, 82, 1013

[68] Ludlow, A. D., Navarro, J. F., Li, M., et al. 2012, MNRAS, 427, 1322

[69] Mac Low, M.-M., & Ferrara, A. 1999, ApJ, 513, 142

[70] Macciò, A. V., Dutton, A. A., & van den Bosch, F. C. 2008, MNRAS, 391, 1940

[71] Macciò, A. V., Stinson, G., Brook, C. B., et al. 2012, ApJ, 744, L9

[72] Marcolini, A., D'Ercole, A., Battaglia, G., & Gibson, B. K. 2008, MNRAS, 386, 2173

[73] Marcolini, A., D'Ercole, A., Brighenti, F., & Recchi, S. 2006, MNRAS, 371, 643

[74] Mashchenko, S., Couchman, H. M. P., & Wadsley, J. 2006, Nature, 442, 539

[75] Mashchenko, S., Wadsley, J., & Couchman, H. M. P. 2008, Science, 319, 174

[76] Mateo, M. L. 1998, ARA&A, 36, 435

[77] McKee, C. F., & Ostriker, J. P. 1977, ApJ, 218, 148

[78] McQuinn, K. B. W., Skillman, E. D., Cannon, J. M., et al. 2010a, ApJ, 721, 297

[79] —. 2010b, ApJ, 724, 49

[80] Miki, Y., Takahashi, D., & Mori, M. 2012, Procedia Computer Science, 9, 96

[81] —. 2013, Computer Physics Communications

[82] Monaghan, J. 1997, Journal of Computational Physics, 136, 298

[83] Monaghan, J. J. 1992, ARA&A, 30, 543

[84] —. 2005, Reports on Progress in Physics, 68, 1703

[85] Moore, B. 1994, Nature, 370, 629

[86] Moore, B., Ghigna, S., Governato, F., et al. 1999a, ApJ, 524, L19

[87] Moore, B., Governato, F., Quinn, T., Stadel, J., & Lake, G. 1998, ApJ, 499, L5

[88] Moore, B., Quinn, T., Governato, F., Stadel, J., & Lake, G. 1999b, MNRAS, 310, 1147

[89] Mori, M., & Burkert, A. 2000, ApJ, 538, 559

[90] Mori, M., Ferrara, A., & Madau, P. 2002, ApJ, 571, 40

[91] Mori, M., & Rich, R. M. 2008, ApJ, 674, L77

[92] Mori, M., Yoshii, Y., & Nomoto, K. 1999, ApJ, 511, 585

[93] Mori, M., Yoshii, Y., Tsujimoto, T., & Nomoto, K. 1997, ApJ, 478, L21

[94] MPI. 2013, The Message Passing Interface (MPI) standard, `http://www.mcs.anl.gov/research/projects/mpi/`

[95] Nakasato, N. 2012, Journal of Computational Science, 3, 132

[96] Navarro, J. F., Eke, V. R., & Frenk, C. S. 1996a, MNRAS, 283, L72

[97] Navarro, J. F., Frenk, C. S., & White, S. D. M. 1995, MNRAS, 275, 720

[98] —. 1996b, ApJ, 462, 563

[99] —. 1997, ApJ, 490, 493

[100] Navarro, J. F., Hayashi, E., Power, C., et al. 2004, MNRAS, 349, 1039

[101] Navarro, J. F., Ludlow, A., Springel, V., et al. 2010, MNRAS, 402, 21

[102] NVIDIA, C. 2011, programming guide 4.0 (2012)

[103] Nyland, L., Harris, M., & Prins, J. 2007, GPU gems, 3, 677

[104] Ogiya, G., & Mori, M. 2011, ApJ, 736, L2

[105] —. 2012, ArXiv e-prints, arXiv:1206.5412

[106] Ogiya, G., Mori, M., Miki, Y., Boku, T., & Nakasato, N. 2013, Journal of Physics Conference Series, 454, 012014

[107] Oh, S.-H., de Blok, W. J. G., Brinks, E., Walter, F., & Kennicutt, Jr., R. C. 2011, AJ, 141, 193

[108] Oh, S.-H., de Blok, W. J. G., Walter, F., Brinks, E., & Kennicutt, Jr., R. C. 2008, AJ, 136, 2761

[109] Okamoto, T., Jenkins, A., Eke, V. R., Quilis, V., & Frenk, C. S. 2003, MNRAS, 345, 429

[110] Omukai, K., & Nishi, R. 1998, ApJ, 508, 141

[111] Peñarrubia, J., Pontzen, A., Walker, M. G., & Koposov, S. E. 2012, ApJ, 759, L42

[112] Pontzen, A., & Governato, F. 2012, MNRAS, 421, 3464

[113] Prada, F., Klypin, A. A., Cuesta, A. J., Betancort-Rijo, J. E., & Primack, J. 2012, MNRAS, 423, 3018

[114] Press, W. H., & Schechter, P. 1974, ApJ, 187, 425

[115] Price, D. J. 2012, Journal of Computational Physics, 231, 759

[116] Ragone-Figueroa, C., Granato, G. L., & Abadi, M. G. 2012, MNRAS, 423, 3243

[117] Read, J. I., & Gilmore, G. 2005, MNRAS, 356, 107

[118] Reed, D., Governato, F., Verde, L., et al. 2005, MNRAS, 357, 82

[119] Rees, M. J., & Ostriker, J. P. 1977, MNRAS, 179, 541

[120] Rosswog, S. 2009, New A Rev., 53, 78

[121] Rubin, V. C., & Ford, Jr., W. K. 1970, ApJ, 159, 379

[122] Rubin, V. C., Ford, W. K. J., & . Thonnard, N. 1980, ApJ, 238, 471

[123] Saitoh, T. R., & Makino, J. 2013, ApJ, 768, 44

[124] Salpeter, E. E. 1955, ApJ, 121, 161

[125] Salucci, P., & Burkert, A. 2000, ApJ, 537, L9

[126] Salucci, P., Wilkinson, M. I., Walker, M. G., et al. 2012, MNRAS, 420, 2034

[127] Salvadori, S., Ferrara, A., & Schneider, R. 2008, MNRAS, 386, 348

[128] Schmidt, M. 1959, ApJ, 129, 243

[129] Sedov, L. I. 1959, Similarity and Dimensional Methods in Mechanics

[130] Silich, S., & Tenorio-Tagle, G. 2001, ApJ, 552, 91

[131] Silk, J. 1968, ApJ, 151, 459

[132] Spano, M., Marcelin, M., Amram, P., et al. 2008, MNRAS, 383, 297

[133] Spekkens, K., Giovanelli, R., & Haynes, M. P. 2005, AJ, 129, 2119

[134] Spergel, D. N., Bean, R., Doré, O., et al. 2007, ApJS, 170, 377

[135] Springel, V. 2005, MNRAS, 364, 1105

[136] —. 2010, ARA&A, 48, 391

[137] Springel, V., & Hernquist, L. 2002, MNRAS, 333, 649

[138] Springel, V., White, S. D. M., Jenkins, A., et al. 2005, Nature, 435, 629

[139] Stadel, J., Potter, D., Moore, B., et al. 2009, MNRAS, 398, L21

[140] Stinson, G., Seth, A., Katz, N., et al. 2006, MNRAS, 373, 1074

[141] Stinson, G. S., Dalcanton, J. J., Quinn, T., Kaufmann, T., & Wadsley, J. 2007, ApJ, 667, 170

[142] Strigari, L. E., Bullock, J. S., Kaplinghat, M., et al. 2008, Nature, 454, 1096

[143] Sutherland, R. S., & Dopita, M. A. 1993, ApJS, 88, 253

[144] Swaters, R. A., Madore, B. F., van den Bosch, F. C., & Balcells, M. 2003, ApJ, 583, 732

[145] Tegmark, M., Blanton, M. R., Strauss, M. A., et al. 2004, ApJ, 606, 702

[146] Teyssier, R., Pontzen, A., Dubois, Y., & Read, J. I. 2013, MNRAS, 429, 3068

[147] Tolstoy, E., Hill, V., & Tosi, M. 2009, ARA&A, 47, 371

[148] Tonini, C., Lapi, A., & Salucci, P. 2006, ApJ, 649, 591

[149] van Eymeren, J., Trachternach, C., Koribalski, B. S., & Dettmar, R.-J. 2009, A&A, 505, 1

[150] Walker, M. G., Mateo, M., Olszewski, E. W., et al. 2009, ApJ, 704, 1274

[151] Warren, M. S., & Salmon, J. K. 1993, in Proceedings of the 1993 ACM/IEEE conference on Supercomputing, ACM, 12–21

[152] Weinberg, M. D., & Katz, N. 2002, ApJ, 580, 627

[153] Weisz, D. R., Dalcanton, J. J., Williams, B. F., et al. 2011, ApJ, 739, 5

[154] Weldrake, D. T. F., de Blok, W. J. G., & Walter, F. 2003, MNRAS, 340, 12

[155] White, S. D. M., & Rees, M. J. 1978, MNRAS, 183, 341

[156] Widrow, L. M. 2000, ApJS, 131, 39

[157] Yokota, R., Barba, L. A., Narumi, T., & Yasuoka, K. 2011, ArXiv e-prints, arXiv:1106.5273

[158] Yoshii, Y., & Arimoto, N. 1987, A&A, 188, 13

[159] —. 1991, A&A, 248, 30

[160] Zwicky, F. 1933, Helvetica Physica Acta, 6, 110